

# Helium $2^3P$ Fine Structure Measurement in a Discharge Cell

A thesis presented

by

Tanya Zelevinsky

to

The Department of Physics

in partial fulfillment of the requirements

for the degree of

Doctor of Philosophy

in the subject of

Physics

Harvard University

Cambridge, Massachusetts

October 2004

©2004 - Tanya Zelevinsky

All rights reserved.

Thesis advisor

Author

Gerald Gabrielse

Tanya Zelevinsky

## Helium $2^3\text{P}$ Fine Structure Measurement in a Discharge Cell

### Abstract

A measurement of helium  $2^3\text{P}$  fine structure was carried out in a discharge cell using saturation spectroscopy. It is the only experiment to directly measure all three fine structure intervals at a 1 kHz level of accuracy. The measured values are 2 291 175.4(6) kHz for the  $2^3\text{P}_1 - 2^3\text{P}_2$  interval, 29 616 951.5(8) kHz for the  $2^3\text{P}_0 - 2^3\text{P}_1$  interval, and 31 908 126.6(1.0) kHz for the  $2^3\text{P}_0 - 2^3\text{P}_2$  interval. All three intervals are the most precise helium fine structure measurements to date. The  $2^3\text{P}_0 - 2^3\text{P}_2$  interval exceeds the precision of its best prior measurement by a factor of 3. The  $2^3\text{P}_0 - 2^3\text{P}_1$  measurement helps resolve an existing disagreement between other experiments. The  $2^3\text{P}_1 - 2^3\text{P}_2$  interval value agrees with other experiments and disagrees with theoretical predictions of two-electron QED. When the disagreement is resolved, the measurements reported here will allow a determination of the fine structure constant to 14 parts in  $10^9$ , surpassing the precision of the well known quantum Hall effect and Josephson effect determinations. One of the leading systematic effects in this experiment is light-pressure-induced frequency shifts. A discharge cell is advantageous in the study and correction of these shifts. Other important systematic effects include pressure shifts, velocity cross-relaxation collisions, and magnetic shifts.

# Contents

Title Page . . . . .	i
Abstract . . . . .	iii
Table of Contents . . . . .	iv
List of Figures . . . . .	vii
Acknowledgments . . . . .	x
<b>1 Introduction</b>	<b>1</b>
<b>2 Background</b>	<b>4</b>
2.1 Various Approaches to Measuring $\alpha$ . . . . .	5
2.1.1 Quantum Hall Effect . . . . .	5
2.1.2 Ac Josephson Effect . . . . .	7
2.1.3 Magnetic Moment of the Electron . . . . .	8
2.1.4 Neutron $h/m_n$ . . . . .	8
2.1.5 Atom $h/m_A$ and Mass Ratios . . . . .	9
2.1.6 Muonium Hyperfine Structure . . . . .	10
2.1.7 Helium Fine Structure . . . . .	10
2.2 Helium Fine Structure: Status of Experiments and QED Calculations	11
2.2.1 Helium Energy Levels and $2^3\text{P}$ Fine Structure . . . . .	11
2.2.2 Theoretical Progress . . . . .	13
2.2.3 Experimental Developments . . . . .	17
<b>3 Experimental Setup</b>	<b>25</b>
3.1 Lasers for Helium Spectroscopy . . . . .	28
3.1.1 Laser Line Width . . . . .	35
3.2 Optical Components . . . . .	40
3.2.1 Optical Isolation . . . . .	40
3.2.2 Optical Spectrum Analyzers . . . . .	41
3.2.3 Fiber Amplifiers . . . . .	43
3.2.4 Modulation and Frequency Shifting of Light . . . . .	45
3.2.5 Spatial Filtering of Light . . . . .	48

3.2.6	Light Intensity Stabilization . . . . .	49
3.2.7	Polarization Control . . . . .	50
3.2.8	Beam Expansion . . . . .	50
3.2.9	Optical Detection . . . . .	51
3.3	Microwave System for Laser Frequency Control . . . . .	51
3.4	Production of $2^3\text{S}$ Metastable Helium . . . . .	57
3.5	Pressure Regulation . . . . .	62
3.6	$^3\text{He}$ Frequency Reference . . . . .	63
3.7	Saturation Spectroscopy of $^4\text{He}$ . . . . .	67
3.7.1	Saturation Spectroscopy Technique . . . . .	67
3.7.2	Implementation and Data Collection . . . . .	71
<b>4</b>	<b>Light-Pressure-Induced Frequency Shifts</b>	<b>73</b>
4.1	Theory of the Light-Pressure Effect for a Two-Level Atom . . . . .	76
4.2	Light-Pressure Effect for Helium Atoms with Degenerate Magnetic Sublevels . . . . .	83
4.2.1	Significance of the Optical and Collisional Time Constants . . . . .	83
4.2.2	The Multilevel Picture of Helium . . . . .	85
4.2.3	Measurement of the Collisional Time Constant . . . . .	87
4.2.4	Line Shape Calculation for a Multilevel Atom . . . . .	87
4.2.5	The Two-Level Atom . . . . .	91
4.2.6	The $2^3\text{S}_1 - 2^3\text{P}_0$ Transition . . . . .	94
4.2.7	The $2^3\text{S}_1 - 2^3\text{P}_1$ Transition . . . . .	94
4.2.8	The $2^3\text{S}_1 - 2^3\text{P}_2$ Transition . . . . .	95
4.3	Results and Comparison with Experiment . . . . .	96
4.3.1	Discontinuous Frequency Shifts Obtained with Orthogonal Pump and Probe Polarizations . . . . .	96
4.3.2	Collisional Parameters Obtained from Discontinuous Frequency Shifts . . . . .	103
4.3.3	Direct Observation of Light Pressure Near Discontinuity Points . . . . .	105
4.4	Light-Pressure Effect at Magnetic Resonance . . . . .	105
4.5	Controlling Light-Pressure-Induced Line Shifts . . . . .	107
<b>5</b>	<b>Zeeman Effect in Helium</b>	<b>110</b>
5.1	Theoretical Description of the Zeeman Effect . . . . .	111
5.1.1	Frequency Shifts . . . . .	111
5.1.2	Line Shapes in a Magnetic Field . . . . .	114
5.1.3	Calculation of the Magnetic Field from Line Splitting . . . . .	118
5.2	Magnetic Field Coils . . . . .	118

---

<b>6</b>	<b>Systematic Study of the Fine Structure Intervals</b>	<b>124</b>
6.1	Measured Line Shapes . . . . .	124
6.2	Velocity Changing Collisions . . . . .	126
6.2.1	Line Shape Including Velocity Changing Collisions . . . . .	127
6.2.2	Limiting Velocity Changing Collisions with Magnetic Resonance	135
6.2.3	Systematic Errors Due to Velocity Changing Collisions . . . . .	137
6.3	Linear Pressure Shifts . . . . .	138
6.3.1	Linear Pressure Shift and Broadening Model . . . . .	139
6.3.2	Pressure Shifts and Broadening in Helium . . . . .	141
6.3.3	Systematic Pressure Shift Corrections . . . . .	142
6.4	Light-Pressure-Induced Shifts . . . . .	143
6.5	Optical Power Shifts . . . . .	148
6.6	Discharge Power Shifts . . . . .	149
6.7	Magnetic Field Corrections . . . . .	152
6.8	Consideration of Other Systematic Effects . . . . .	152
6.8.1	Wavefront Curvature of Optical Beams . . . . .	152
6.8.2	Frequency Offset between Pump and Probe Beams . . . . .	153
6.8.3	Coupling of Systematic Effects . . . . .	154
6.9	Experimental Statistics . . . . .	156
6.10	Results . . . . .	158
<b>7</b>	<b>Conclusion</b>	<b>163</b>
7.1	Significance of the Results . . . . .	163
7.2	Future Improvements . . . . .	164
7.3	Summary . . . . .	166
	<b>Bibliography</b>	<b>167</b>

# List of Figures

2.1	Comparison of various fine structure constant measurements. . . . .	6
2.2	$^4\text{He}$ energy levels. . . . .	12
2.3	Progress of helium $2^3\text{P}$ fine structure calculations. . . . .	18
2.4	History of helium $2^3\text{P}$ fine structure interval measurements. . . . .	19
3.1	Saturation spectroscopy setup. . . . .	26
3.2	Diode laser cavity. . . . .	28
3.3	Variation of optical power with laser diode current. . . . .	29
3.4	Variation of optical power with laser diode temperature. . . . .	30
3.5	Using an anamorphic prism pair to correct the diode laser beam ellipticity. . . . .	32
3.6	Setup for measuring the diode laser line width. . . . .	34
3.7	Laser line width at several output coupler reflectivities. . . . .	37
3.8	Dependence of the laser line width on the extended cavity length. . .	38
3.9	Diode laser line width measurement with a fiber delay interferometer.	39
3.10	Principle of optical isolation. . . . .	40
3.11	Absorption and emission peak wavelengths of Yb-doped fiber amplifiers.	44
3.12	Fiber amplifier schematic diagram. . . . .	45
3.13	Acousto-optic effect. . . . .	46
3.14	Spatial filtering of optical beams. . . . .	48
3.15	Optical power regulation. . . . .	49
3.16	Microwave and rf components for the diode laser offset lock. . . . .	52
3.17	Phase frequency detector and compensation circuit for the diode laser offset lock. . . . .	54
3.18	Locked beatnote between the scan and clock lasers. . . . .	56
3.19	Rf discharge setup for metastable helium production. . . . .	57
3.20	Doppler-broadened profile of the $2^3\text{S}_1 - 2^3\text{P}_1$ and $2^3\text{S}_1 - 2^3\text{P}_2$ transitions.	58
3.21	Density of metastable $2^3\text{S}$ helium atoms in the discharge cell as a function of pressure. . . . .	60
3.22	Pressure regulation system. . . . .	62

3.23	Comparison of $^3\text{He}$ and $^4\text{He}$ energy levels. . . . .	64
3.24	Clock laser locking setup. . . . .	65
3.25	$^3\text{He}$ derivative signal for locking the clock laser. . . . .	66
3.26	Helium clock stability measurement. . . . .	67
3.27	Principle of saturation spectroscopy. . . . .	68
3.28	Saturation spectroscopy scan of the $^4\text{He}$ $2^3\text{S}_1 - 2^3\text{P}_2$ transition. . . . .	69
3.29	Optical pumping for $2^3\text{S}_1 - 2^3\text{P}_{0,1,2}$ transitions. . . . .	71
4.1	Doppler profile with a dispersive modification resulting from momentum transfer by the pump beam. . . . .	77
4.2	Optical pressure effectively superimposes a dispersive component onto the symmetric saturation line shape. . . . .	82
4.3	Explanation of the blue shift of the saturation peak. . . . .	84
4.4	Level structures and coupling coefficients for the $2^3\text{S}_1 - 2^3\text{P}_{0,1,2}$ transitions. . . . .	85
4.5	Half width of the $2^3\text{S}_1 - 2^3\text{P}_1$ line as a function of helium pressure. . . . .	88
4.6	Computed light-pressure-induced frequency shifts of a two-level atom. . . . .	93
4.7	Helium light-pressure-induced frequency shifts with a lin $\perp$ lin polarization configuration. . . . .	97
4.8	The $f_{12}$ fine structure interval measured with the lin $\perp$ lin polarization configuration. . . . .	98
4.9	Calculated ratios of the $2^3\text{S}_1 - 2^3\text{P}_0$ signal amplitudes in the lin $\perp$ lin configuration to the signal amplitudes of a two-level atom. . . . .	100
4.10	Helium light-pressure-induced frequency shifts with a lin $\parallel$ lin polarization configuration. . . . .	102
4.11	Direct manifestation of optical pressure creating a dispersive kink in the helium velocity distribution. . . . .	104
4.12	Light-pressure-induced shifts at magnetic resonance. . . . .	106
4.13	Reducing the light-pressure-induced shifts of the fine structure intervals by adjusting the pump and probe polarizations. . . . .	108
4.14	Reducing the light-pressure-induced shifts of the fine structure intervals by resolving the magnetic sublevels. . . . .	108
5.1	Saturation spectroscopy peak locations for $2^3\text{S} - 2^3\text{P}$ helium transitions with resolved magnetic sublevels. . . . .	115
5.2	Coils used to create a magnetic field in the helium cell. . . . .	119
5.3	Calculated distribution of vertical magnetic field strengths about the measured average field in the illuminated region of the helium cell. . . . .	120
5.4	Magnetic field measurement histogram. . . . .	122
6.1	Line shapes of magnetically resolved $2^3\text{S} - 2^3\text{P}$ helium transitions. . . . .	125
6.2	A $2^3\text{S}_1 - 2^3\text{P}_0$ line scan showing a large portion of the broad background arising from velocity changing collisions. . . . .	130

---

6.3	A $2^3S_1 - 2^3P_1$ line scan showing a large portion of the broad background arising from velocity changing collisions. . . . .	131
6.4	Heights and widths of the broad signal backgrounds arising from velocity changing collisions. . . . .	133
6.5	Effect of magnetic resonance of the rf discharge with the $2^3S$ Zeeman splitting on the broad backgrounds arising from velocity changing collisions. . . . .	135
6.6	The $2^3P_0 - 2^3P_1$ interval error that arises if vcc pedestals are not accounted for in the line fits. . . . .	136
6.7	Linear extrapolation of the fine structure interval values to zero pressure, including corrections of the light-pressure-induced frequency shifts. . . . .	142
6.8	Schematic showing how the interval frequencies $f_{12}$ , $f_{01}$ , and $f_{02}$ , and the frequency $d_0$ used for light-pressure correction, are measured from the three $2^3S_1 - 2^3P_J$ transitions. . . . .	144
6.9	Linear dependence of $d_0$ , the measure of the light-pressure-induced shifts, on optical power. . . . .	146
6.10	The histogram of $d_0$ measurements at 18 mTorr. . . . .	147
6.11	Light shifts of the fine structure intervals. . . . .	150
6.12	Dependences of the fine structure intervals on rf discharge power. . . . .	151
6.13	Variation of optical power transmitted through the cell with helium pressure. . . . .	155
6.14	Fine structure interval measurement histograms. . . . .	157
6.15	Comparison of the most recent helium fine structure interval measurements. . . . .	160
6.16	Comparison of the $2^3P$ helium fine structure theoretical values and Harvard measurements. . . . .	161

# Acknowledgments

I am grateful to Professor Gerald Gabrielse for giving me a chance to work on this experiment. While offering his students a lot of freedom in research, he provides us with enough guidance to keep us on the right track and to instill the sense of confidence. Many thanks also to Dr. Ron Walsworth and Professors Shaoul Ezekiel and John Doyle for help and advice along the way, to Dan Farkas for valuable help with projects and unending enthusiasm, to Klaus Hermanspahn for introducing me to the lab, and to Jan Ragusa for handling the administrative tasks and giving us more time to spend on research.

Of course, I greatly appreciate the support of my parents and family, who have encouraged my interest in science since an early age, and have shared in happy as well as difficult times. Special thanks to my husband Niell Elvin for providing the inspiration without always knowing.

This work and the first three years of my graduate studies were supported by the National Science Foundation.

# Chapter 1

## Introduction

This thesis describes a new precision measurement of helium fine structure. The first goal of the measurement is to test the theoretical techniques of two-electron quantum electrodynamics (QED) used to calculate helium energy levels. The second goal is to combine theoretical calculations and experimental results to obtain a new value of the fine structure constant,  $\alpha$ , one of the most fundamental quantities in physics.

The best determination of the fine structure constant to date comes from measurements of the electron magnetic moment. However, it is vital to measure  $\alpha$  using a variety of approaches, such as single particle physics, atomic physics, and solid state physics. One reason is that these approaches have different degrees of reliance on QED expansions of the measured quantities, and therefore different aspects of QED are experimentally tested. The second reason is that experiments performed using dissimilar techniques are not affected by the same systematic errors. By comparing these experiments, problems with specific experimental techniques can be discov-

ered. Finally, unresolved disagreements between  $\alpha$  measurements based on different approaches can point to new physics outside the framework of QED.

While several other helium fine structure experiments have recently been carried out, as discussed in Chapter 2, the measurement described in this work plays an important role. First, it is the only self-consistent measurement of all three (interdependent)  $2^3\text{P}$  helium fine structure intervals at a 1 kHz level of precision. Second, it helps resolve a disagreement between the  $2^3\text{P}_0 - 2^3\text{P}_1$  interval measurements, while improving on the precision of all three intervals. In addition, it confirms the disagreement between helium experiments and theory, which needs to be understood before a value of  $\alpha$  can be determined from helium fine structure. Finally, the measurement techniques differ substantially from those used in the other experiments, ensuring that the possible systematic errors are quite different.

This work is based on optical spectroscopy of helium in a discharge cell. All other helium fine structure precision experiments rely on metastable helium beams. The high accuracy of the results reported here attests to the possibility of using gas cells in precision measurements. The shifts due to the discharge and interatomic collisions are shown to be small and readily measured. Moreover, the use of a discharge cell has two advantages. The first advantage is a high signal to noise ratio, leading to relatively short averaging times. The second advantage is the simplicity of optical pressure studies, and was discovered in the course of this experiment. Since helium is a light atom, it is highly susceptible to pressure exerted by laser photons. Systematic shifts associated with this pressure have a characteristic dependence on the density of helium in the cell, which makes them significantly easier to measure and correct in

---

a cell than in a beam. The study of optical pressure on helium in the discharge cell described in this thesis is also of independent interest.

Chapter 2 summarizes past and present experimental and theoretical work on helium fine structure. Chapter 3 describes the details of the experimental setup used to carry out the measurement reported here. Chapter 4 provides details on the investigation of light-pressure effects in a helium discharge cell, which is the first known study of optical pressure on multilevel atoms. Chapter 5 presents the properties of helium energy levels in magnetic fields that are relevant to the experiment. Chapter 6 discusses all systematic shifts that affect the fine structure measurements, as well as the final results. Finally, Chapter 7 concludes the discussion of the measurement and suggests future improvements to the experiment.

# Chapter 2

## Background

The fine structure constant  $\alpha$  was introduced by Sommerfeld to describe relativistic energy level splitting of the Bohr atom [1]. It is defined as

$$\alpha = \frac{1}{4\pi\epsilon_0} \frac{e^2}{\hbar c} \tag{2.1}$$

in SI units, and has a magnitude of approximately 1/137. Since the fine structure constant is proportional to the squared electronic charge  $e$ , it is a measure of the strength of electromagnetic interactions. As such,  $\alpha$  is one of the most fundamental constants of nature, dominating the behavior of physical, chemical, and biological systems. Although its historical name is still used, the significance of  $\alpha$  extends far beyond quantifying spin-orbit interactions.

The fundamental origin of the fine structure constant implies that it can be measured in a variety of physical systems, from particle to macroscopic [2]. Comparisons between those measurements serve as consistency checks and as tests of the renormalizable theory of QED. Some measurements are non-QED in a sense that they yield  $\alpha$  directly, such as measurements of the quantum Hall effect, while others rely

on higher-order QED calculations of physical quantities, such as measurements of helium fine structure splitting. Ultimately, all experimental determinations of  $\alpha$  are tests of QED.

The 1998 Committee on Data for Science and Technology (CODATA) [5] value of the fine structure constant derived from the measurements described below is

$$\alpha^{-1} = 137.035\,999\,76(50) \quad (3.6 \text{ ppb}), \quad (2.2)$$

where ppb refers to parts per billion. This value is based mostly on the original electron magnetic moment measurement [6], before a mistake in the QED theory was fixed [7], and its fractional precision is 3.7 ppb. A graphic comparison of the various  $\alpha$  measurements along with their absolute and fractional uncertainties is shown in Fig. 2.1.

## 2.1 Various Approaches to Measuring $\alpha$

### 2.1.1 Quantum Hall Effect

When a strong perpendicular magnetic field is applied to a two-dimensional electron gas at a low temperature, the resistance of the gas is quantized as [8]

$$R_n = \frac{h}{e^2 n} \quad (2.3)$$

for  $n = 1, 2, \dots$ . Measuring the Hall resistance in SI units is a direct measure of  $\alpha$ , since

$$\alpha = \frac{c\mu_0}{2nR_n}. \quad (2.4)$$

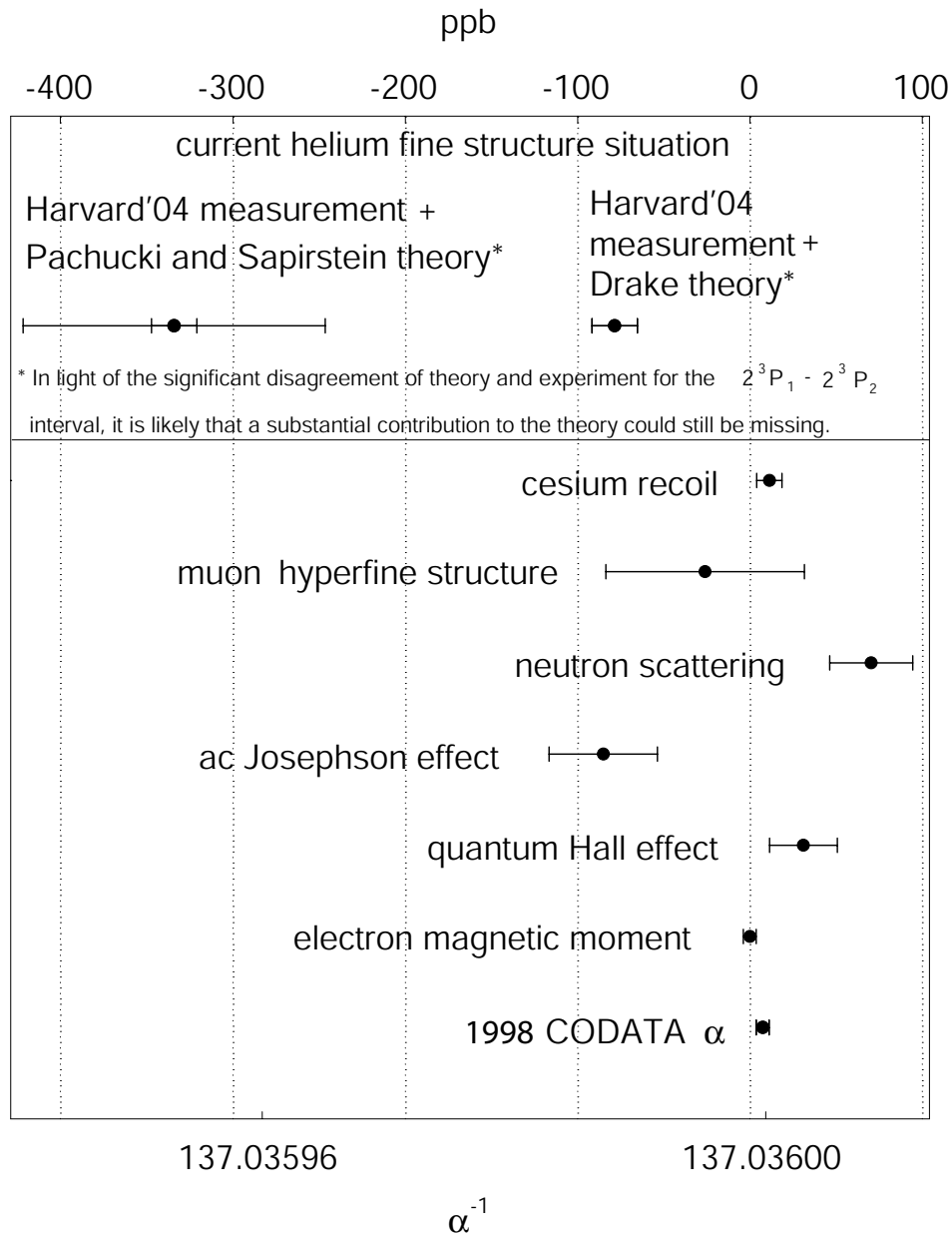


Figure 2.1: Comparison of various inverse fine structure constant measurements. The values obtained from the helium fine structure measurements reported here are based on two theoretical works [3, 4]. Drake estimates the theory error to be much smaller than the experimental error. The larger error on the result that relies on the Pachucki and Sapirstein theory is their estimation of the uncalculated higher-order terms already included by Drake, and the smaller error is experimental. The small experimental errors make the helium measurement one of the most precise ways to measure  $\alpha$ , once the theoretical calculations are refined to the needed accuracy.

The 1998 CODATA gives a value of the inverse fine structure constant based on the Quantum Hall effect [8] as

$$\alpha_{qH}^{-1} = 137.036\,003\,0(27) \quad (20 \text{ ppb}). \quad (2.5)$$

The measurement error arises mainly from the calibration of the Ohm.

### 2.1.2 Ac Josephson Effect

A dc voltage  $V$  applied across a superconducting junction leads to an alternating current of frequency [9]

$$f = \frac{2eV}{h}. \quad (2.6)$$

Numerous studies reveal no dependence of  $f$  on the specific materials used in the junction [10]. This implies that knowledge of  $V$  and  $f$  determines  $\alpha$  if combined with an independent knowledge of  $e$  or  $\hbar$ , since the speed of light  $c$  is a defined constant. The additional measurements required to deduce  $\alpha$  are summarized in the relation

$$\alpha^{-2} = \frac{c}{4R_\infty \gamma'_p} \frac{\mu'_p}{\mu_B} \frac{2e}{h}, \quad (2.7)$$

where  $\mu_B$  is the Bohr magneton,  $\mu'_p$  [11] and  $\gamma'_p$  are the magnetic moment and gyromagnetic ratio of the proton in water, and the Rydberg constant

$$R_\infty \equiv \frac{m_e c}{2h} \alpha^2 \quad (2.8)$$

is known very precisely from 1S – 2S hydrogen spectroscopy and QED calculations [2]. In 1998, CODATA reported a value of  $\alpha$  based on the ac Josephson effect as

$$\alpha_{acJ}^{-1} = 137.035\,987\,1(43) \quad (31 \text{ ppb}). \quad (2.9)$$

The precision is limited by the error in the gyromagnetic ratio of the proton in water,  $\gamma'_p$  [12].

### 2.1.3 Magnetic Moment of the Electron

The most precise  $\alpha$  measurement to date stems from an experimental determination of the anomalous magnetic moment of the electron or positron,  $a_e$ . Its theoretical value is the best-known quantity in QED,

$$a_e^{\text{theory}} = 0.5 \left(\frac{\alpha}{\pi}\right) - 0.328 \dots \left(\frac{\alpha}{\pi}\right)^2 + 1.181 \dots \left(\frac{\alpha}{\pi}\right)^3 - \dots \quad (2.10)$$

A comparison of the theoretical and experimental [6, 7] values of  $a_e$  yields the inverse fine structure constant

$$\alpha_{a_e}^{-1} = 137.035\,999\,58(52) \quad (3.8 \text{ ppb}). \quad (2.11)$$

By virtue of its precision, this measurement is the largest contributor to the 1998 CODATA value of  $\alpha$ . The leading cause of uncertainty is the shift of the electron or positron axial frequency in the Penning trap that arises from interaction of the particle with cavity modes.

An experiment in the Gabrielse group is currently completing the first fully quantum measurement of the electron magnetic moment in a cylindrical Penning trap with a well-known mode structure. This measurement is likely to improve the precision of  $\alpha$  by a factor of 5 or more, with further improvements expected in the future.

### 2.1.4 Neutron $h/m_n$

The fine structure constant can be expressed as

$$\alpha^2 = \frac{2R_\infty m_n}{c} \frac{h}{m_e m_n}, \quad (2.12)$$

where only the ratio of the Planck constant to the neutron mass,  $h/m_n$ , is not yet known to an extremely high precision [2]. It is determined [13] by measuring two quantities, the velocity  $v$  and de Broglie wavelength  $\lambda$  of a neutron beam, since

$$\lambda = \frac{h}{m_n v}. \quad (2.13)$$

The wavelength is found from a Bragg reflection of the neutrons off a silicon crystal, and the velocity is found from back-reflecting and detecting a modulated neutron beam. The 1998 value of  $\alpha$  obtained by this method as quoted by CODATA is

$$\alpha_{h/m_n}^{-1} = 137.036\,008\,4(3\,3) \quad (24 \text{ ppb}). \quad (2.14)$$

This measurement is limited by the purity of the silicon crystal.

### 2.1.5 Atom $h/m_A$ and Mass Ratios

Analogously to eq. (2.12),  $\alpha$  can be expressed through the mass of an atom  $m_A$ ,

$$\alpha^2 = \frac{2R_\infty m_p m_A}{c m_e m_p} \frac{h}{m_A}. \quad (2.15)$$

This very promising approach to measuring  $\alpha$  [14] is made possible by recent developments in laser cooling [15], atom interferometry [16], and mass ratio precision measurements [17]. The latest measurement of  $h/m_{\text{Cs}}$  from cesium atom recoil upon absorption of a  $D1$  photon yields a preliminary value of  $\alpha$  with a precision of 7.4 ppb [18, 19], second only to the 3.8 ppb precision of  $\alpha_{a_e}$ ,

$$\alpha_{h/m_{\text{Cs}}}^{-1} = 137.036\,000\,3(1\,0) \quad (7 \text{ ppb}). \quad (2.16)$$

This experiment may yield higher precision in the future, since it has few fundamental limitations, and error can be minimized by reducing the vibrational noise and increasing the interrogation time of the atom interferometer.

### 2.1.6 Muonium Hyperfine Structure

Ground state hyperfine structure of a single-electron atom is a very suitable system for measuring  $\alpha$ . For example, the 1420 MHz hyperfine splitting of the hydrogen ground state is experimentally known to better than  $10^{-12}$ . The QED theory of the interval is also very well understood. The lack of sufficient knowledge of the proton form factors arising from strong interactions, however, prevents the possibility of obtaining a good theoretical value of the splitting.

In contrast to hydrogen, muonium has a leptonic nucleus, unaffected by strong interactions. Ground state muonium hyperfine structure has been measured [20] and compared with theory. The 1998 CODATA value of  $\alpha$  extracted from muonium hyperfine structure experiments is

$$\alpha_{\mu\text{hfs}}^{-1} = 137.035\,995\,2(79) \quad (58 \text{ ppb}). \quad (2.17)$$

The leading source of error is the uncertainty in the muon mass.

### 2.1.7 Helium Fine Structure

Helium  $2^3\text{P}$  fine structure is an alternative atomic system for  $\alpha$  measurements. The advantages over the  $2\text{P}$  hydrogen fine structure are the 100 ns lifetime and 40 GHz splitting, as compared to 1.6 ns and 10 GHz for hydrogen, both resulting in higher precision. Helium fine structure is measured using microwave or laser spectroscopy, and compared with its theoretical expansion in powers of  $\alpha$ . The fine structure constant values obtained from the helium experiment described in this work and

from theoretical calculations by Pachucki and Sapirstein [3] and by Drake [4] are

$$\alpha_{\text{Harvard, PS}}^{-1} = 137.035\,952\,9(18)(11\,6) \quad (14 \text{ ppb})(88 \text{ ppb}), \quad (2.18)$$

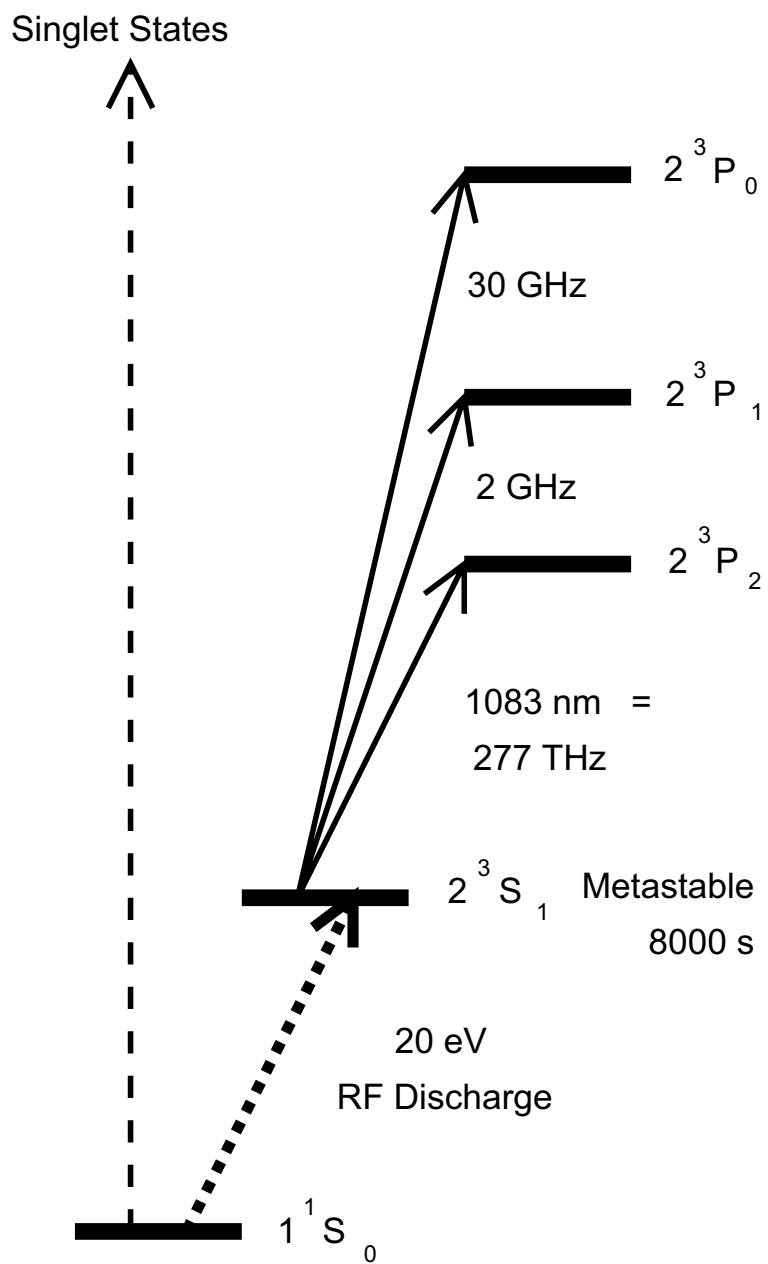
$$\alpha_{\text{Harvard, D}}^{-1} = 137.035\,988\,0(1\,8)(6) \quad (14 \text{ ppb})(5 \text{ ppb}), \quad (2.19)$$

where the first quoted error is experimental, and the second error is the estimation of the uncalculated higher-order terms, some of which have already been explicitly included by Drake. Both theory groups agree that some important terms may have been omitted from the calculations [21], and the complexity of the calculation currently dominates the uncertainty in the final result. However, advances are continuously made on both the theoretical and experimental fronts. A precision helium spectroscopy experiment, carried out to obtain a new value of  $\alpha$  and to check the QED theory for two-electron atoms, is the subject of this thesis.

## 2.2 Helium Fine Structure: Status of Experiments and QED Calculations

### 2.2.1 Helium Energy Levels and $2^3\text{P}$ Fine Structure

This thesis reports a new measurement of the  $2^3\text{P}$  fine structure of helium.  $^4\text{He}$  energy levels (not to scale) are shown in Fig. 2.2. The ground state  $1^1\text{S}_0$  is a spin singlet. Excited states are either spin singlets or triplets, and the two sets are not connected by dipole transitions. Triplet states lie lower in energy than their singlet counterparts because their electronic wave functions are antisymmetric as required by the Pauli exclusion principle, and the two repelling electrons are further apart in

Figure 2.2:  $^4\text{He}$  energy levels.

position space. In all stable excited configurations of helium, one electron remains in the ground state, while the second electron occupies a higher energy level.

The first excited state is  $2^3S_1$ . It is a metastable state with a lifetime of approximately 8000 s, and it lies about 20 eV above the ground state. The gap between  $2^3S_1$  and the second excited state  $2^3P$  is 277 THz, or 1083 nm.  $2^3P$  is split into three fine structure levels with  $J = 0, 1, \text{ and } 2$ . The two independent fine structure intervals  $f_{JJ'}$  are  $f_{12} \simeq 2.291$  GHz and  $f_{01} \simeq 29.617$  GHz. The third interval,  $f_{02} \simeq 31.908$  GHz, is the sum of the first two.

A comparison of the experimental value of  $f_{01}$  and its theoretical expansion in powers of  $\alpha$  can be used to derive a value of the fine structure constant. The  $f_{12}$  interval is less sensitive to  $\alpha$  due to its small size. Therefore, any reasonably precise value of  $\alpha$  (most commonly,  $\alpha_{a_e}$ ) can be substituted into the expansion of  $f_{12}$  to obtain its theoretical value. For this reason,  $f_{12}$  is usually used to test the accuracy of two-electron QED predictions.

## 2.2.2 Theoretical Progress

Wave functions of two-electron quantum mechanical systems obey the Schrödinger equation

$$-\frac{\hbar^2 \nabla_1^2}{2m_e} \Psi - \frac{\hbar^2 \nabla_2^2}{2m_e} \Psi - \frac{2e^2}{r_1} \Psi - \frac{2e^2}{r_2} \Psi + \frac{e^2}{r_{12}} \Psi = E\Psi. \quad (2.20)$$

The calculation of the wave functions and energy levels is difficult because of the  $1/r_{12}$  term. Fine structure corrections to the energy levels arise from spin-orbit interactions of each of the two electrons, as well as from a spin-spin interaction between the electrons. In order to find the energy levels modified by fine structure, relativistic

effects must be taken into account. The Breit equation [22] gives fine structure intervals to first order. The Breit equation is

$$\left(E - H_1 - H_2 - \frac{e^2}{r_{12}}\right) \Psi = -\frac{e^2}{2r_{12}} \left[ \vec{\alpha}_1 \cdot \vec{\alpha}_2 + \frac{(\vec{\alpha}_1 \cdot \vec{r}_{12})(\vec{\alpha}_2 \cdot \vec{r}_{12})}{r_{12}^2} \right] \Psi, \quad (2.21)$$

where the Dirac Hamiltonian is

$$H_i = -e\varphi(\vec{r}_i) + \beta_i mc^2 + \vec{\alpha}_i \cdot (c\vec{p}_i + e\vec{A}(\vec{r}_i)), \quad (i = 1, 2) \quad (2.22)$$

$\vec{\alpha}$  and  $\beta$  are the Dirac matrices that operate on the spinor components of  $\Psi$ , and  $\varphi$  and  $\vec{A}$  are the scalar and vector electromagnetic potentials that include the nuclear Coulomb potential. This equation is a generalization of the Dirac equation for a two-electron system. The Breit equation is not fully Lorentz-invariant, and the higher-order corrections of the fine structure intervals are obtained from the extensive set of equations derived by Bethe and Salpeter [23].

The fine structure intervals  $f_{JJ'}$  can be written as expansions in powers of  $\alpha$  as [4]

$$f_{JJ'} = C_2\alpha^2 + C_3\alpha^3 + C_4\alpha^4 + C'_5\alpha^5 \ln \alpha + C_5\alpha^5 + \mathcal{O}(\alpha^6). \quad (2.23)$$

Each coefficient  $C$  in eq. (2.23) is itself an expansion of the form

$$C = C^{(0)} + \left(\frac{\mu}{M}\right) C^{(1)} + \left(\frac{\mu}{M}\right)^2 C^{(2)} + \mathcal{O}\left(\left(\frac{\mu}{M}\right)^3\right), \quad (2.24)$$

where  $M$  is the nuclear mass of helium and  $\mu$  is the reduced electron mass. The expansion coefficients present a great calculational challenge, since each contains contributions from many different processes, such as spin-orbit, spin-spin, and spin-other-orbit interactions. Theoretical error estimation is also difficult, since the error arises from the contributions of an infinite number of higher-order terms, and its size cannot be precisely known.

Two recent theoretical works calculate helium fine structure intervals up to order  $\alpha^5$ , and derive the fine structure constant in terms of the measured interval values.

Pachucki and Sapirstein quote [3]

$$f_{01} = \alpha^2 \times 556\,200\,289.5(1) \text{ MHz} - 1.487\,1(5\,0) \text{ MHz}. \quad (2.25)$$

Eq. (2.25) predicts the inverse fine structure constant based on the  $f_{01}$  measurement reported in this thesis as

$$\alpha_{\text{Harvard, PS}}^{-1} = 137.035\,952\,9(1\,8)(11\,6) \quad (14 \text{ ppb})(88 \text{ ppb}), \quad (2.26)$$

where the first error is experimental and the second error is an estimation of the uncalculated higher-order terms. It corresponds to a 5 kHz uncertainty in the fine structure interval.

Drake's expression relating  $\alpha$  and the  $f_{01}$  measurement is [4]

$$f_{01} = \alpha^2 \times 556\,200\,289.4(1) \text{ MHz} - 1.472\,1(3) \text{ MHz}. \quad (2.27)$$

Eq. (2.27) predicts the inverse fine structure constant based on the Harvard University  $f_{01}$  measurement as

$$\alpha_{\text{Harvard, D}}^{-1} = 137.035\,988\,0(1\,8)(6) \quad (14 \text{ ppb})(5 \text{ ppb}), \quad (2.28)$$

where the first uncertainty is experimental and the second uncertainty is an estimation of the uncalculated terms.

The two values of  $\alpha$  in eqs. (2.26, 2.28) disagree. One reason for the disagreement is that Pachucki and Sapirstein have not verified or included the remaining known QED corrections to the electron-electron interaction in their final results, and hence

assigned larger errors. Drake computes the total contribution of these terms to be 15 kHz and 7 kHz on the  $f_{01}$  and  $f_{12}$  interval values [21]. Most of the other corrections have been checked, and those included by both theory groups are in agreement. An exception is the inclusion by Drake of the Bethe logarithmic contribution to the electron-nuclear interaction that was only calculated by Pachucki and Sapirstein [24]. The difference between the two  $\alpha$  results is indicative of the size of the  $\mathcal{O}(\alpha^5 \ln \alpha)$  and  $\mathcal{O}(\alpha^5)$  terms presently being calculated.

The values of  $\alpha$  in eqs. (2.26, 2.28) disagree with  $\alpha_{ae}$  by nearly 4 times the estimated theoretical error for both theory values. Another indication of unresolved problems with the helium theory is that the theoretical and experimental values for the  $f_{12}$  interval disagree. The theoretical predictions of the  $f_{12}$  fine structure interval by Drake and by Pachucki and Sapirstein disagree with experiment by approximately 20 and 3 times the combined experimental and theoretical uncertainty, respectively. Pachucki and Sapirstein's theoretical expression for the  $f_{12}$  interval is [25]

$$f_{12} = \alpha^2 \times 43\,148\,533.2(1) \text{ MHz} - 6.555\,9(50) \text{ MHz}, \quad (2.29)$$

and the value of  $\alpha$  obtained using this expression and the Harvard measurements, equivalent to eqs. (2.25 - 2.28) for the  $f_{01}$  interval, is [21]

$$\alpha^{-1} = 137.035\,597(18)(150) \quad (130 \text{ ppb})(1100 \text{ ppb}), \quad (2.30)$$

with the experimental error shown first and the theoretical error shown last. Drake's expression is [21]

$$f_{12} = \alpha^2 \times 43\,148\,532.9(1) \text{ MHz} - 6.563\,2(3) \text{ MHz}, \quad (2.31)$$

which leads to

$$\alpha^{-1} = 137.035\,380(18)(9) \quad (130 \text{ ppb})(66 \text{ ppb}). \quad (2.32)$$

These  $\alpha$  values disagree with  $\alpha_{a_e}$ , by factors of 3 and 30 times the combined uncertainties, respectively. This disagreement indicates that more theoretical efforts are required before experimental values of helium fine structure intervals can be used for a competitive determination of the fine structure constant.

The progress of helium  $2^3\text{P}$  fine structure calculations is shown in Fig. 2.3. The values measured in the experiment described here are also shown for comparison. In addition, earlier calculations by Lewis and Serafino [26], Drake *et al.* [27, 28], and Pachucki and Sapirstein [29], are presented. The earliest calculations by Schwartz [30] and Douglas, Hambro, and Kroll [31] are not shown, since they differ from the later values by several megahertz and about 200 kHz, respectively, and thus do not fit on the graphs in Fig. 2.3.

### 2.2.3 Experimental Developments

The history of  $2^3\text{P}$  helium fine structure measurements is summarized below. Published values from four research groups, as well as the new values obtained in this work, are presented in Fig. 2.4. An expanded plot comparing the most recent measurements is near the end of this work, in Fig. 6.15.

#### **Yale University Experiments by Hughes *et al.***

The earliest measurements of helium  $2^3\text{P}$  fine structure were made at Yale University by Hughes *et al.* starting in the late 1960's [32, 33, 34]. They employed a

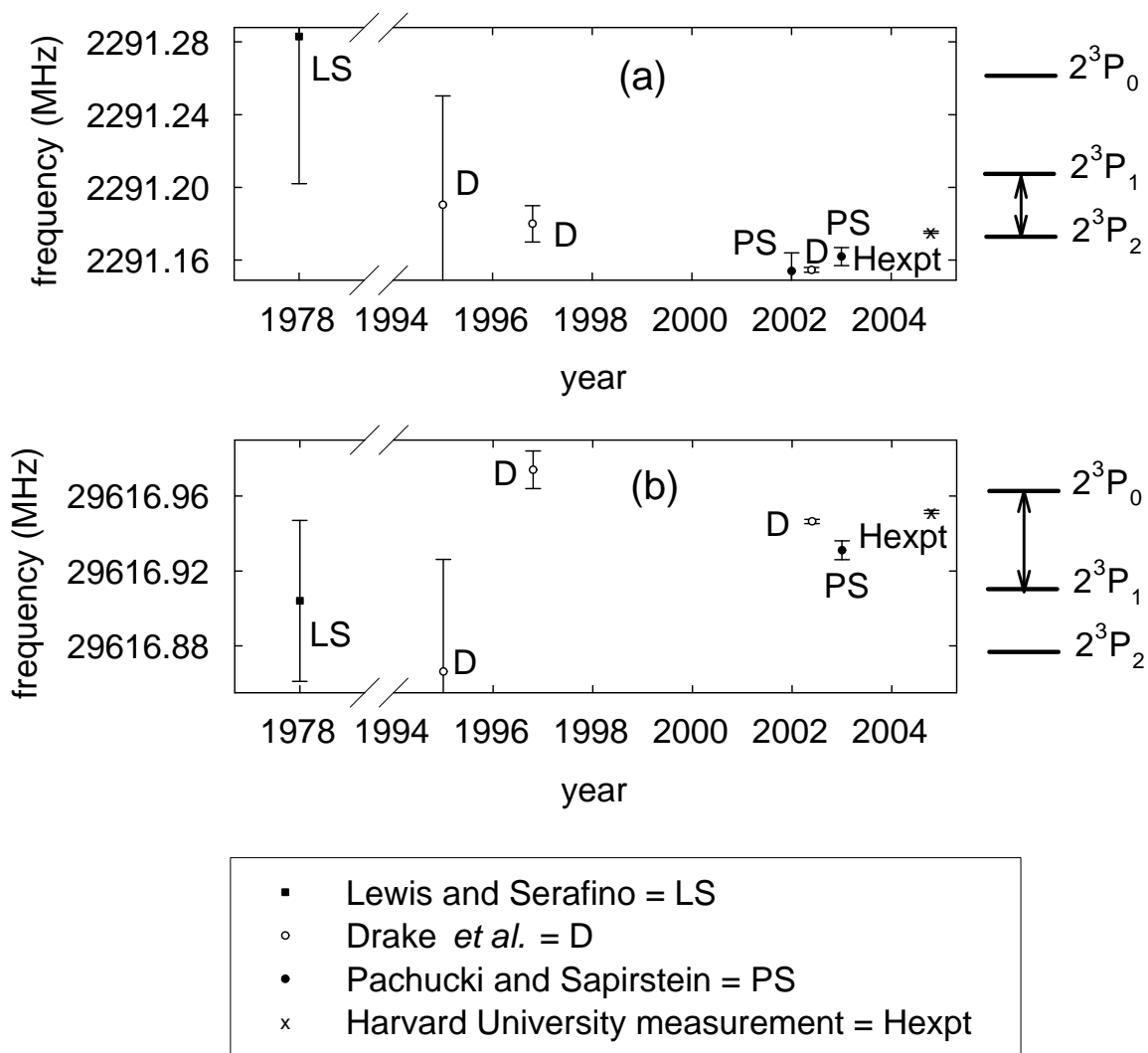


Figure 2.3: Progress of helium  $2^3P$  fine structure calculations. (a) The  $2^3P_1 - 2^3P_2$  interval. (b) The  $2^3P_0 - 2^3P_1$  interval.

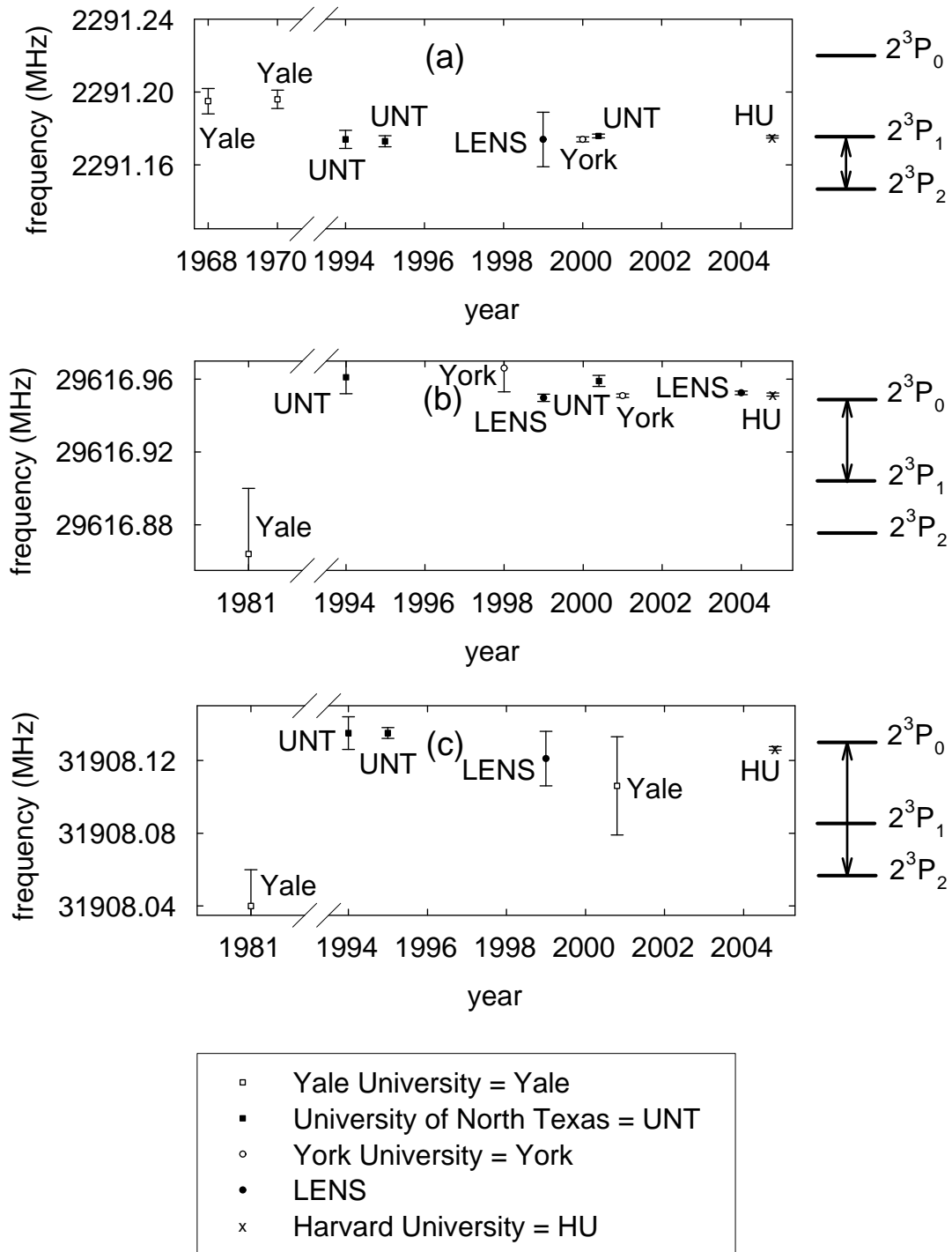


Figure 2.4: History of helium  $2^3P$  fine structure interval measurements. (a) The  $2^3P_1 - 2^3P_2$  interval. (b) The  $2^3P_0 - 2^3P_1$  interval. (c) The  $2^3P_0 - 2^3P_2$  interval.

technique that combined optical and microwave spectroscopy of a helium beam in a magnetic field. The atoms in the  $2^3S_1(m_J)$  metastable sublevels were spatially separated and then recombined at a detector. In the middle part of the trajectory, the atoms encountered a region of uniform magnetic field. In this region, a helium discharge lamp induced 1083 nm transitions between the  $2^3S$  and the  $2^3P$  states, causing a fraction of atoms in the  $2^3S(m_J = 0)$  sublevel to be optically pumped into the  $2^3S(m_J = 1)$  sublevel. In addition to the optical fields, a resonant microwave drive was applied to couple the  $2^3P$  fine structure levels. The resulting mixing of the magnetic sublevel populations led to a change in the fraction of  $2^3S_1(m_J = 0)$  atoms at the detector. This change was measured using phase-sensitive detection.

These were pioneering experiments, carried out in the days when laser sources at 1083 nm were not yet available. The development of such lasers made it possible to make more accurate measurements in the 1990's.

### **University of North Texas Experiments by Shiner *et al.***

The modern era of helium fine structure began in measurements by another group at Yale University [35], which then moved to the University of North Texas. Great excitement was generated when new laser measurements disagreed with earlier work by more than twice the combined experimental error. A subsequent reanalysis of the old measurements in 2000 revealed an error in the magnetic field measurement, and brought the  $f_{02}$  interval value into agreement with the new results, as shown in Fig. 2.4 (c).

The Texas fine structure measurement relies on laser excitation of helium to the

$2^3\text{P}$  states. In the latest experimental determination of  $f_{12}$ , an electro-optic modulator puts sidebands on light from a 1083 nm diode laser that makes the light resonant with both  $2^3\text{S}_1 - 2^3\text{P}_1$  and  $2^3\text{S}_1 - 2^3\text{P}_2$ . A metastable helium beam passes through an inhomogeneous magnetic field that deflects the atoms with  $m_J = \pm 1$ . Then, in a uniform magnetic field region, both levels  $2^3\text{P}_1$  and  $2^3\text{P}_2$  are simultaneously excited by sidebands to  $m_J = \pm 1$  and subsequently decay to  $2^3\text{S}_1 (m_J = 0, \pm 1)$ . The  $2^3\text{S}_1 (m_J = \pm 1)$  population is detected.

The advantage of using modulated light is fast switching between optical transitions and cancellation of laser frequency drifts that occur on longer time scales. The main limitations of the experiment are related to line center determination using pairs of points on opposite sides of the line shapes, and to imperfect cancellation of the first-order Doppler shifts.

The results from this group are [36]

$$f_{12}^{\text{Texas}'00} = 2291.175\,9(1\,0)\text{MHz} \quad (440 \text{ ppb}) \quad (2.33)$$

and

$$f_{01}^{\text{Texas}'00} = 29616.959(3)\text{MHz} \quad (100 \text{ ppb}). \quad (2.34)$$

### **European Laboratory for Nonlinear Spectroscopy (LENS) Experiments by Inguscio *et al.***

The helium spectroscopy facility at LENS uses techniques that are closest to those described here since they rely on  $2^3\text{S} - 2^3\text{P}$  spectroscopy without spatial separation of atoms in different magnetic sublevels. The setup consists of a metastable beam apparatus, and optical spectroscopy is performed with a retroreflected 1083 nm diode

laser that acts as a pump and probe. The interaction and detection region is free of magnetic fields, and the detected quantity is saturated fluorescence.

The advantages of this experiment are relative simplicity and lack of magnetic fields, which limits the potential sources of systematic errors. The leading systematic error is due to optical pressure exerted by laser photons on helium atoms. It is probed experimentally by varying how much of the helium beam is illuminated by the laser. Ultimately, the contribution of this effect to the error budget has to be theoretically estimated.

The fine structure intervals measured by this group are [37]

$$f_{12}^{\text{LENS}'99} = 2291.174(15)\text{MHz} \quad (6500 \text{ ppb}) \quad (2.35)$$

and [38]

$$f_{01}^{\text{LENS}'04} = 29616.952\,5(10)\text{MHz} \quad (34 \text{ ppb}). \quad (2.36)$$

### York University Experiments by Hessels *et al.*

Helium fine structure measurements at York University are based entirely on microwave spectroscopy of the  $2^3P_J$  levels. A metastable helium beam is subjected to a magnetic field that resolves Zeeman sublevels. A 1083 nm diode laser induces optical pumping into the  $2^3S_1$  ( $m_J = 1$ ) sublevel, and the atoms subsequently interact with circularly polarized light to populate  $2^3P_1$  ( $m_J = 0$ ). The atoms then enter a microwave excitation cavity where they undergo a transition to  $2^3P_2$  ( $m_J = 0$ ) or to  $2^3P_0$  ( $m_J = 0$ ), depending on whether the  $f_{12}$  or  $f_{01}$  fine structure interval is being measured. The atoms that finally decay to  $2^3S_1$  ( $m_J = 0$ ) are detected by observing the  $2^3S_1$  ( $m_J = 0$ ) –  $2^3P_0$  fluorescence.

An important advantage of this work is reliance on microwave spectroscopy only, and an absence of optical frequency fields in the excitation region. This ensures that most systematic effects are different from those of the other fine structure measurements. The main systematic effect arises from leakage of microwave power through the grid of the excitation cavity, which slightly distorts the line shape. A general disadvantage of this method is the necessity to construct a new microwave cavity for the measurement of each fine structure interval.

The latest results reported by this group are [39]

$$f_{12}^{\text{York}'00} = 2291.1740(14)\text{MHz} \quad (610 \text{ ppb}) \quad (2.37)$$

and [40]

$$f_{01}^{\text{York}'01} = 29616.9509(9)\text{MHz} \quad (30 \text{ ppb}). \quad (2.38)$$

## Harvard University Experiment

The fine structure measurement carried out at Harvard University and described in this thesis is based on  $2^3\text{S}_1 - 2^3\text{P}_J$  1083 nm Doppler-free laser spectroscopy. The atoms in a pressure-variable discharge cell are subject to a constant magnetic field that resolves spectral lines and allows a reduction of light-pressure effects.

Optical pressure is still the leading systematic effect, along with velocity cross-relaxation collisions that distort spectral line shapes. The advantages of using the discharge cell are large signals and the possibility of a clean light pressure study. The disadvantages are the presence of interatomic collisions, and the application of rf discharge to the measurement region.

This experiment allows easy switching between measurements of the three fine

structure intervals. All three intervals were studied, thus establishing internal consistency of the experiment. The results are

$$f_{12}^{\text{Harvard}'04} = 2291.175\,4(6)\text{MHz} \quad (260 \text{ ppb}), \quad (2.39)$$

$$f_{01}^{\text{Harvard}'04} = 29616.951\,5(8)\text{MHz} \quad (27 \text{ ppb}), \quad (2.40)$$

and

$$f_{02}^{\text{Harvard}'04} = 31908.126\,6(10)\text{MHz} \quad (31 \text{ ppb}). \quad (2.41)$$

# Chapter 3

## Experimental Setup

The helium fine structure experiment is based on Doppler-free saturation spectroscopy in a discharge cell. The basic principle of this well-known technique [41] is to expose atoms to two oppositely directed photons from the same laser and thus eliminate first-order Doppler broadening of the spectral line. A Doppler-free measurement is crucial for precision spectroscopy as it leads to a thousandfold reduction in line width. In practice, it is achieved by splitting the laser beam into two counter-propagating components, pump and probe. The laser frequency is then scanned across the atomic resonance, revealing a spectral line with a width determined mostly by lifetime of the excited state.

Fig. 3.1 shows the schematic outline of the experiment. The laser is stabilized to an atomic clock using frequency modulation spectroscopy [42]. The clock setup is very similar to the  $^4\text{He}$  spectroscopy setup with the exception of sidebands imposed on the laser frequency. The sidebands allow locking to the center point of an atomic transition. A  $^3\text{He}$  transition was chosen as the frequency reference (or the clock tran-

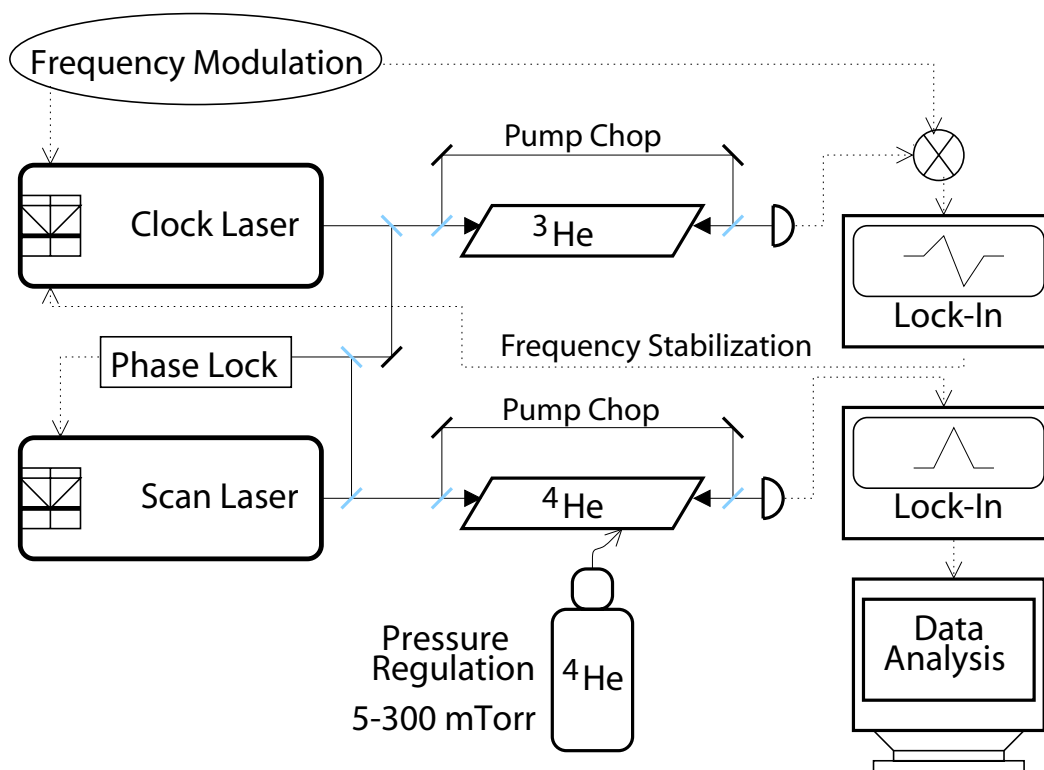


Figure 3.1: Schematic representation of the saturation spectroscopy setup.

sition) because the  $^3\text{He}$  energy levels are close to those of  $^4\text{He}$ , placing the difference frequencies in a convenient microwave regime.

The main distinction between this experiment and other helium fine structure measurements [40, 36, 37] is the use of a discharge helium cell rather than a metastable atomic beam. One advantage of the cell is a high signal to noise ratio due to an increased number of sampled atoms. The second important advantage was discovered in the course of this experiment. Collisions in the cell can be used to interrupt optical pumping and minimize light-pressure-induced frequency shifts. These shifts contribute to the measurement uncertainty, and are discussed in detail in Chapter 4. A disadvantage of the cell is the need to apply a discharge to the region where probing takes place in order to create metastable helium. This introduces a possibility of a systematic effect related to the discharge, which is hard to understand in detail. Systematic shifts also arise from interatomic collisions in the cell. To facilitate investigation of these shifts, a pressure variation system is utilized.

Initially, the experiment was performed in a magnetic field-free region in order to eliminate a source of systematic effects related to dc magnetic fields. However, degenerate Zeeman sublevels led to light-pressure-induced line shifts that dominated the measurement error. Hence the fine structure interval measurements were carried out in a constant magnetic field that split the lines by about 15 line widths. Systematic effects associated with magnetic fields are important to second order of the field, but they are much easier to control than light-pressure shifts.

This experiment utilizes optical laser spectroscopy to couple  $2^3\text{S}$  and  $2^3\text{P}$  states of  $^4\text{He}$ . The  $2^3\text{S}_1 - 2^3\text{P}_J$  and  $2^3\text{S}_1 - 2^3\text{P}_{J'}$  frequencies are measured within about a

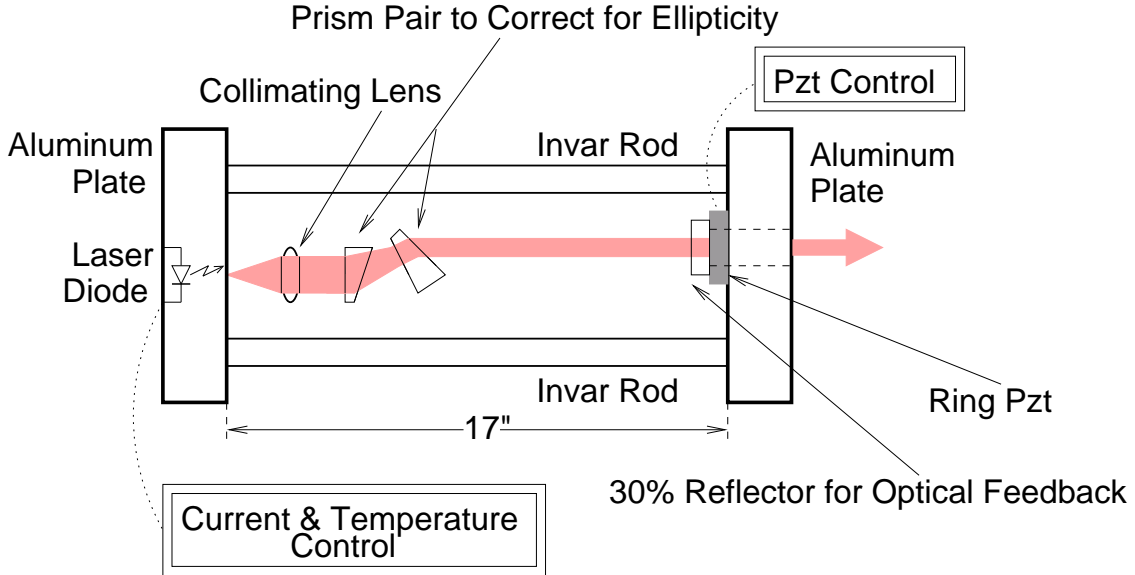


Figure 3.2: Diode laser cavity including optical elements.

minute of each other and subtracted to find the  $f_{JJ'}$  fine structure interval. Although this approach requires measuring two frequencies of  $\sim 10^{14}$  Hz and subtracting them to find a much smaller frequency of  $\sim 10^{10}$  Hz, the degree of laser control that is possible to achieve allows making an improved measurement of the fine structure intervals.

Below, all components of the apparatus in Fig. 3.1 are explained in greater detail, and the physics of saturation spectroscopy is discussed.

### 3.1 Lasers for Helium Spectroscopy

The lasers used in this experiment are SDL-6702 InGaAs diodes manufactured in TO-3 packages and placed in external cavities for tuning and improved spectral purity. The diode spectrum is centered around the 1083 nm wavelength, resonant

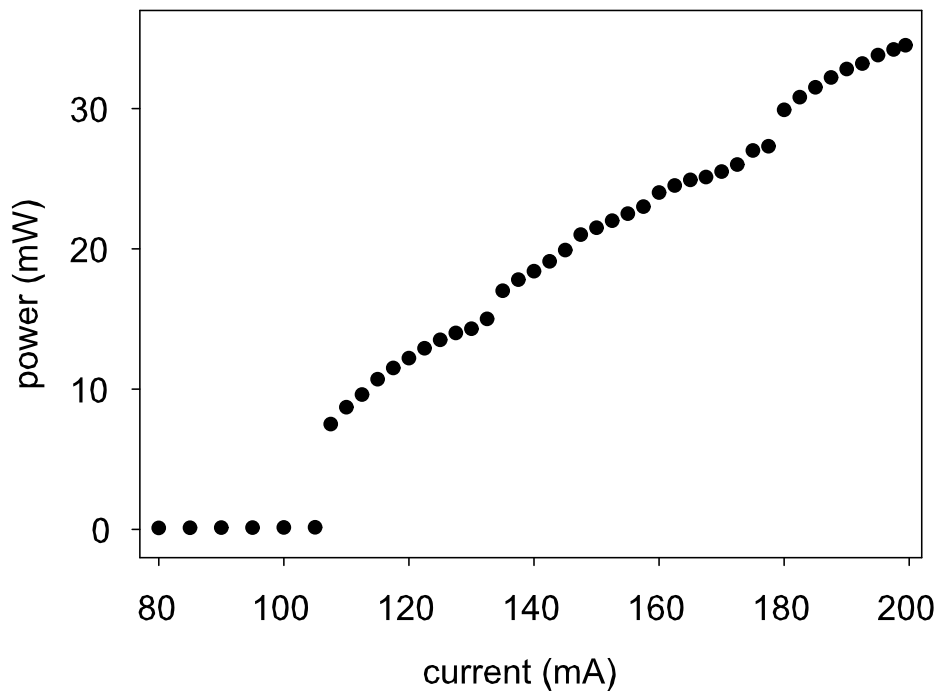


Figure 3.3: The variation of optical power with laser diode current shows a threshold behavior near 110 mA, and discontinuities due to mode hops.

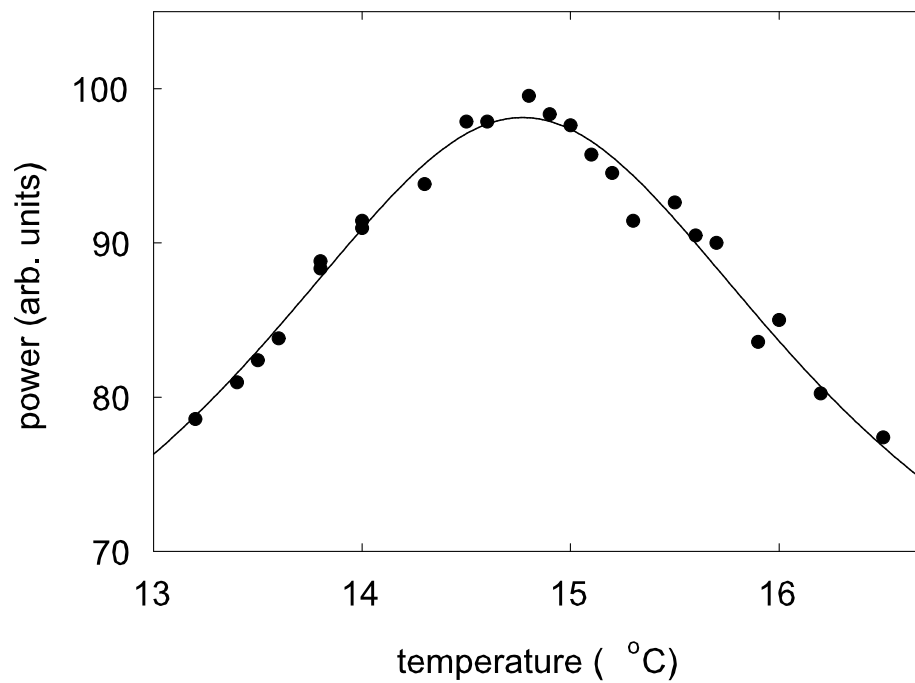


Figure 3.4: The variation of optical power with laser diode temperature. The curve is centered around an optimal operating temperature. A Lorentzian is drawn through the points.

with the helium  $2^3S - 2^3P$  transition. A diagram of the laser cavity is shown in Fig. 3.2. The case of the diode is firmly attached to an aluminum back plate for heat sinking and stability, and a negative current of about 170 mA is sent to the cathode from an ILX Lightwave LDC-3722B laser diode controller. The anode of the laser package is grounded. When new, the diodes can emit up to 50 mW of optical power, but the output power degrades over a course of several years. The diode temperature is regulated with the ILX Lightwave controller at  $0.01^\circ\text{C}$ . Typical measured dependences of the output power on current and temperature are shown in Figs. 3.3 and 3.4. The current dependence shows threshold behavior near 110 mA. Above threshold, there are discontinuities due to mode hops. The most stable laser operation is achieved away from the discontinuities. Each diode contains an internal Bragg grating for single mode operation. As a result, the measured free-running line width is only about 0.5 MHz. In reality, internal mode selection is dominated by the external cavity and optical feedback.

Operating current for the diode lasers is close to 170 mA. Operating temperatures vary between different batches of diodes, and have to be found by either measuring the laser frequency with a wavemeter or by looking at a beatnote of the laser with another laser of a known frequency. Temperature control serves as coarse tuning of the laser with a frequency dependence of about  $-20 \text{ GHz}/^\circ\text{C}$ . The diode used in the fine structure measurements is operated at  $23.4^\circ\text{C}$ ,  $24.8^\circ\text{C}$ , and  $24.9^\circ\text{C}$ , for  $2^3S_1 - 2^3P_0$ ,  $2^3S_1 - 2^3P_1$ , and  $2^3S_1 - 2^3P_2$ , respectively.

The diode output is highly divergent and has a large numerical aperture of close to 0.5. A lens with a short focal length is necessary to collect and collimate the laser

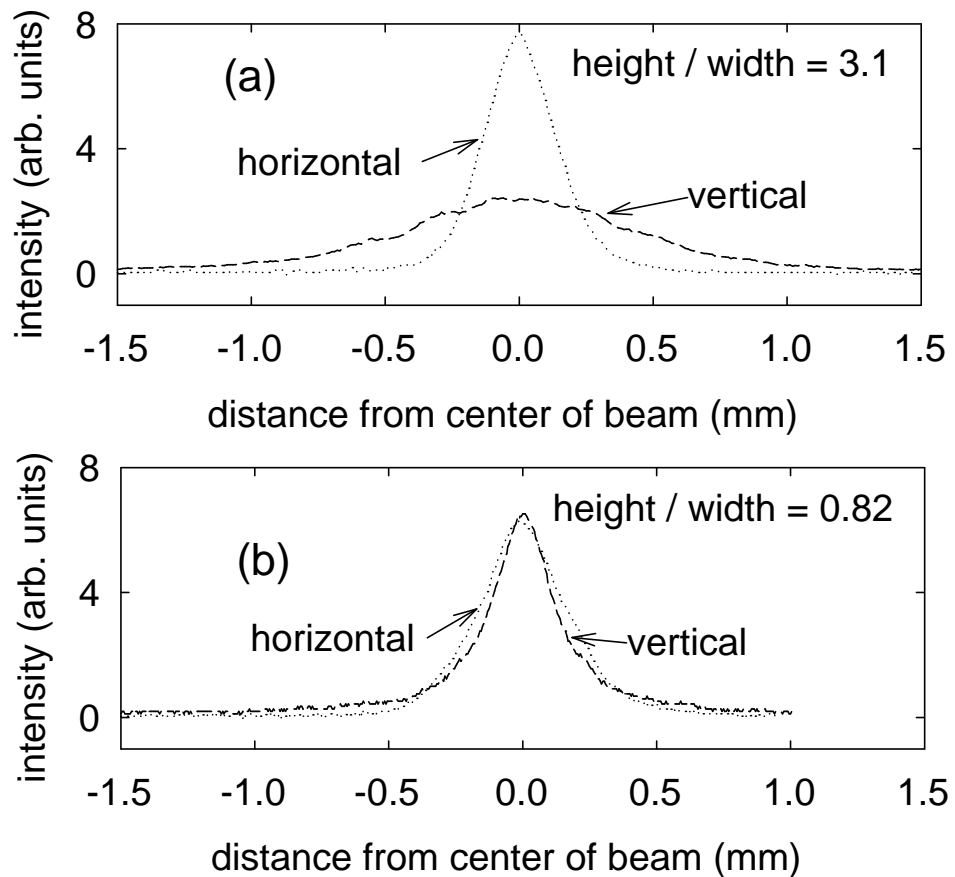


Figure 3.5: Using an anamorphic prism pair to correct the ellipticity of the diode laser beam. (a) Laser beam profile without the prism pair. The ratio of the beam height to its width is 3.1. (a) Laser beam profile with the prism pair. The ratio of the beam height to its width is 0.82.

output without loss of power. In addition, the diode output is strongly elliptical, with a beam height to beam width ratio of about 3. An anamorphic prism pair is inserted into the laser cavity after the collimating lens to correct the ellipticity. The original and improved beam profiles in the horizontal and vertical directions are shown in Figs. 3.5 (a) and (b).

Optical feedback, sometimes called injection locking, is used to narrow the diode laser spectrum by an order of magnitude, to several tens of kilohertz. A partial reflector attached to the front plate of the laser cavity reflects 30% of the light back into the diode. The length of the cavity allows only certain discrete longitudinal modes, and frequency components of the spectrum that are not supported by the cavity are suppressed.

The output coupler is mounted on a ring piezoelectric transducer (pzt). In order to fine-tune the laser frequency, voltage is applied to the pzt, forcing the cavity length to contract or expand. The boundary condition is

$$\frac{n\lambda}{2} = L, \quad (3.1)$$

where  $L$  is the cavity length,  $\lambda$  is the wavelength of the light, and  $n$  is an integer.

Since the light frequency  $\nu = c/\lambda$ , eq. (3.1) implies that

$$\nu = \frac{nc}{2L}, \quad (3.2)$$

and the differential change in frequency is

$$\delta\nu = -\nu \frac{\delta L}{L}. \quad (3.3)$$

For  $\nu \simeq 300$  THz and  $L \simeq 40$  cm,

$$\frac{\delta\nu}{\delta L} \simeq -1 \text{ GHz}/\mu\text{m}. \quad (3.4)$$

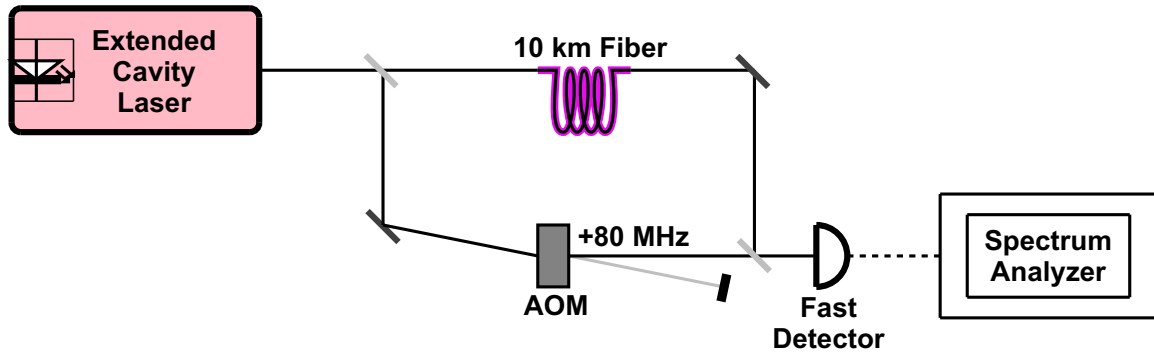


Figure 3.6: Setup for measuring the diode laser line width.

About 1 GHz of fine tuning is required to comfortably scan an atomic transition line, which corresponds to a pzt movement of approximately  $1 \mu\text{m}$ . This is achieved with a 300 V controller driven by a PA85 high-voltage operational amplifier. Since the controller gain is 20, the pzt tuning sensitivity of the laser is 3 MHz/Volt.

The front and back plates of the cavity are held together by 1" thick invar rods. Invar has a nearly zero thermal expansion coefficient at room temperature, and makes the laser frequency more immune to thermal drift.

Alignment of the optics inside the laser cavity is critical for avoiding mode hops and controllable tuning. The light has to closely retrace its path upon reflection from the output coupler. Presence of optical feedback can be determined by turning the diode current down to just below threshold in the absence of feedback. As the coupler position is adjusted with an ultrastable Burleigh micrometer tilt mount, the diode output power suddenly increases once feedback is attained.

### 3.1.1 Laser Line Width

The spectral widths of the diode lasers are narrowed in order to avoid broadening of the helium lines. This is accomplished with extended cavities, as explained above. The clock laser line width can be monitored using a delay fiber interferometer setup shown in Fig. 3.6. The laser beam is split into two paths. One path is delayed with several kilometers of multimode optical fiber, and the other is frequency-offset by 80 MHz with an AOM, in order to reduce noise in the detection bandwidth. The interferometer paths are then recombined on a detector, and the 80 MHz beatnote is viewed on a spectrum analyzer. The optical fiber must be much longer than the laser coherence length in order for the beatnote to truly reflect the laser line width.

The effect of the finite fiber length on the measured laser line width is estimated as follows. Let  $f(t) = f_0 + \delta f(t)$  be the laser frequency,  $\Delta f_L$  the full width of the laser spectrum,  $\Delta f_{\text{beat}}$  the full width of the beatnote measured with the interferometer setup,  $\langle f(t) \rangle$  the time average of  $f(t)$ ,  $\tau_D$  the fiber delay time, and  $\tau_{\text{coh}} \equiv 1/(2\pi\Delta f_L)$  the coherence time of the laser. Then

$$\begin{aligned}\Delta f_{\text{beat}} &= \sqrt{\langle (f(t) - f(t - \tau_D))^2 \rangle} \\ &= \sqrt{\langle \delta f(t)^2 + \delta f(t - \tau_D)^2 - 2\delta f(t)\delta f(t - \tau_D) \rangle},\end{aligned}\tag{3.5}$$

and, using the exponential autocorrelation function for a Lorentzian spectrum,

$$\begin{aligned}\Delta f_{\text{beat}} &= \sqrt{2\langle f(t)^2 \rangle - 2\langle f(t)f(t - \tau_D) \rangle} \\ &= \sqrt{2}\Delta f_L \sqrt{1 - e^{-\tau_D/(2\tau_{\text{coh}})}} = \sqrt{2}\Delta f_L \sqrt{1 - e^{-\pi\tau_D\Delta f_L}}.\end{aligned}\tag{3.6}$$

The factor of  $\sqrt{2}$  arises from the fact that the two interferometer paths represent two independent oscillators in the long delay limit, and the exponential factor is a

correction that appears because the delay time is finite and the oscillators are therefore not completely independent.

The delay time for a fiber of length  $l = 3300$  m is

$$\tau_D = \frac{n_c l}{c} = 16 \mu\text{s} \quad (3.7)$$

where  $n_c = 1.46$  is the index of refraction of the fiber core, and

$$\frac{\tau_D}{2\tau_{\text{coh}}} = \frac{\Delta f_L}{20 \text{ kHz}}. \quad (3.8)$$

Therefore, a 3.3 km fiber provides sufficient delay if the laser line width is significantly larger than 20 kHz. Since typical line widths are only a few times larger than 20 kHz, the exponential correction from eq. (3.6) is applied to the measured beatnote width. In addition, the laser line width was checked with a 10 km fiber [43], yielding the same result as the 3.3 km fiber.

Laser line width measurements were used to optimize the spectrum with respect to the output coupler reflectivity and the extended cavity length. Line width was measured for 10%, 30%, and 50% reflectors, as shown in Fig. 3.7. The 30% and 50% couplers lead to similar line widths that are narrower than the 10% couple line width. The 30% coupler was chosen to allow a higher percentage of the laser power to leave the cavity.

The extended cavity length was varied by using invar rods of different lengths. The spectral width dependence on the cavity length is shown in Fig. 3.8. Narrower widths were observed for longer lengths, and 17" was chosen. Even longer laser cavities are more susceptible to environmental drifts and creep, and place tighter requirements on the tilt resolution of the output coupler.

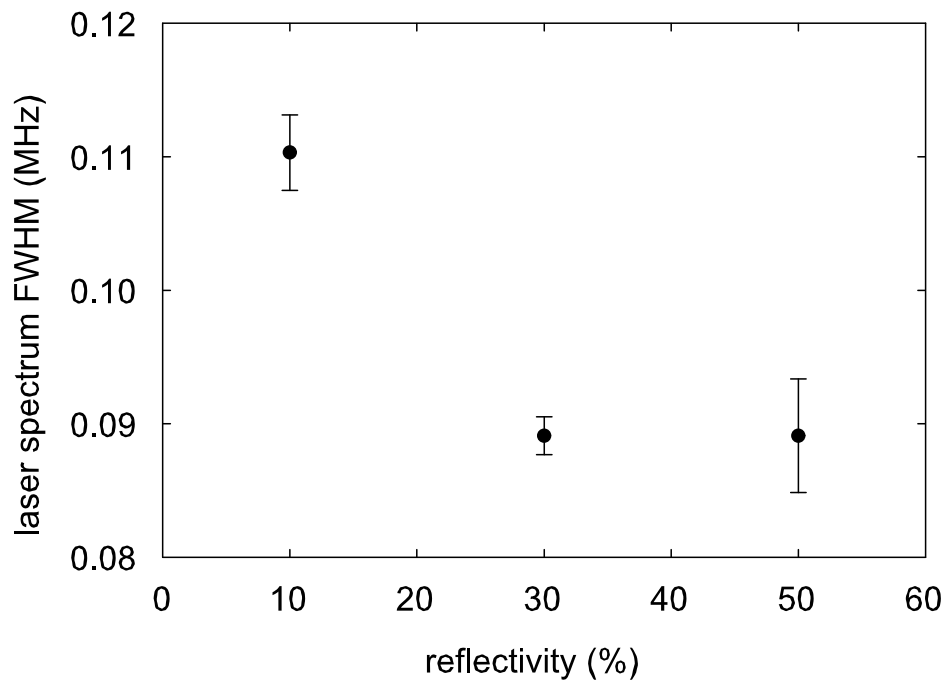


Figure 3.7: Laser line width at several output coupler reflectivities.

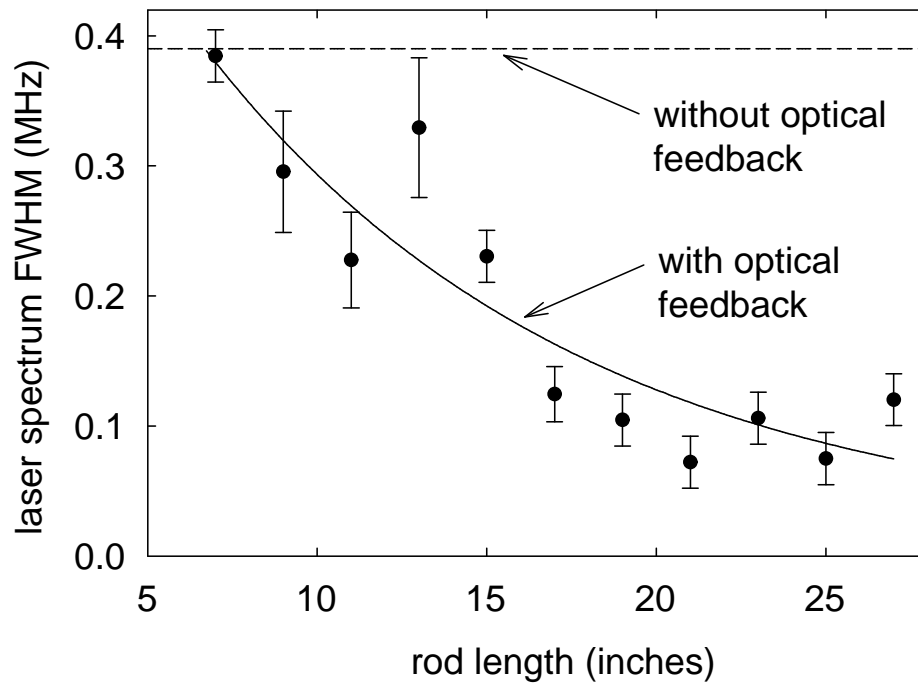


Figure 3.8: The dependence of laser line width on the extended cavity length. The cavity length is about 2" shorter than the indicated rod length.

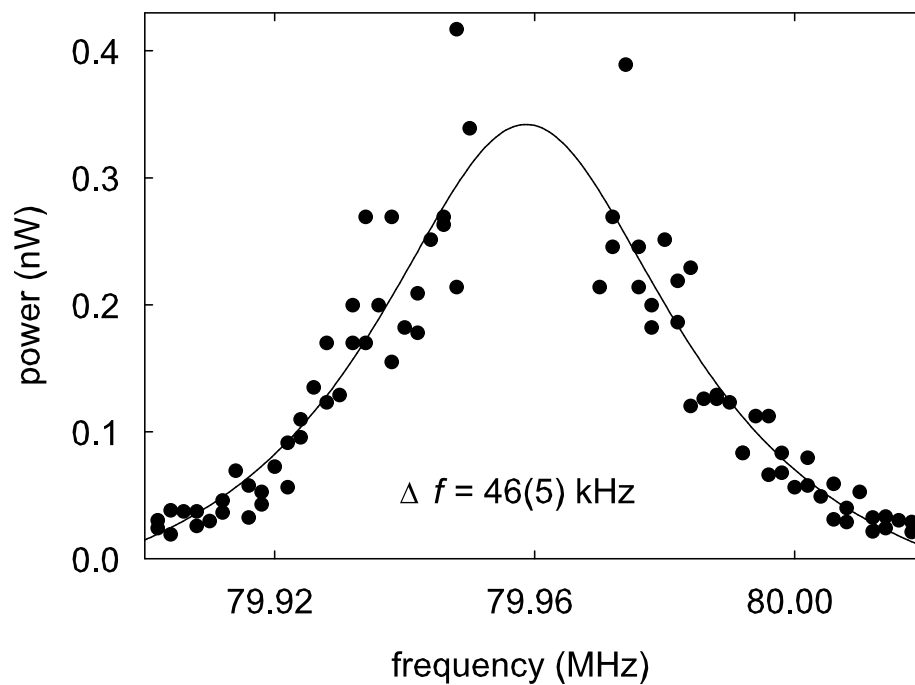


Figure 3.9: Diode laser line width measurement using the delay fiber interferometer with a 3.3 km fiber. A narrow central peak, caused by the spatially overlapping zeroth order AOM output, was removed.

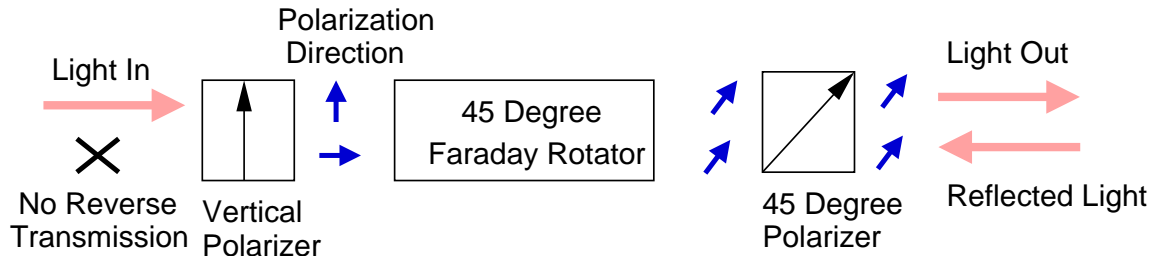


Figure 3.10: The principle of optical isolation.

The cavities constructed with 17" invar rods and 30% output couplers are placed in boxes to minimize effects of air turbulence and sound, and attached to the optical table. Under these conditions, the best measured line width was 46(5) kHz. The interferometer beatnote for this measurement is shown in Fig. 3.9. In order to narrow the spectral width further, active techniques are needed, such as locking the laser to a high finesse cavity or a narrow atomic transition using feedback to the diode current.

## 3.2 Optical Components

Optical components other than the diode lasers and their extended cavities are described in this section.

### 3.2.1 Optical Isolation

Light back-reflected onto the diode laser causes unwanted optical feedback leading to frequency and amplitude instabilities of the lasers and even permanent damage. It is therefore necessary to isolate the lasers from back-reflected light. The IO-YAG

isolators, model IO-5-1083-HP, manufactured by OFR are used for this purpose. The principle behind optical isolation is illustrated in Fig. 3.10. Incoming light is vertically polarized, and subsequently its polarization is rotated by  $45^\circ$  as it propagates through a gyrotropic medium created by applying a magnetic field to a magneto-optic material. A medium is gyrotropic if two orthogonal circular polarizations traverse it at different velocities. Linearly polarized light propagating through this medium rotates polarization in space by an angle given by the length of the medium. This is called Faraday rotation. At the output of the isolator is a  $45^\circ$  polarizer. Any back-reflected light first passes through this polarizer, and its polarization is rotated by an additional  $45^\circ$  angle by the Faraday rotator. The light is then completely rejected by the input vertical polarizer of the isolator.

The isolation of the OFR devices is about 45 dB. After initial alignment of the input and output polarizers in a way that agrees with the laser polarization, the best way to optimize performance is to reverse the isolator in the laser beam and adjust the angle of the output polarizer until transmission reaches minimum.

Identical isolators are also installed after fiber amplifiers (see Sec. 3.2.3) to prevent damaging optical feedback.

### 3.2.2 Optical Spectrum Analyzers

Burleigh SA-200 optical spectrum analyzers are used to verify single mode operation of the diode lasers. These spectrum analyzers are confocal Fabry-Perot interferometers. In a confocal cavity, identical spherical mirrors are separated by a distance equal to their radius of curvature, and light rays cross the cavity four times before

multiple beam interference takes place. Free spectral range of a cavity is the frequency interval by which adjacent frequencies corresponding to maximum cavity transmission are separated. Since the transmitted spectrum is repeated with every  $\lambda/4$  increase in mirror spacing, the free spectral range of confocal cavities is  $\text{FSR} = c/(4nR)$ , where  $R$  is the mirror separation as well as their radius of curvature, and  $n$  is the refractive index. Therefore, in a confocal cavity the free spectral range is set by the properties of the mirrors. Although it is a limitation, the advantage of the confocal over a flat-mirror geometry is that it is relatively insensitive to alignment of the mirrors inside the cavity as long as their separation is properly fixed. The only critical aspect of alignment is that of the optical beam. In fact, if the incoming beam is perfectly aligned with the cavity axis, mode matching is achieved, and the FSR is doubled. Complete mode matching is usually not needed in practice. Each spectrum analyzer features a pzt-mounted mirror to scan the cavity length, and a built-in optical detector. The mirror properties are such that the FSR is about 2 GHz, and the cavity finesse is about 200.

The spectrum analyzer pzt is driven with a Burleigh RC-45 CFT controller capable of putting out high-voltage ramp signals. A cable also connects the spectrum analyzer to a photodetector amplifier inside the controller. The amplified signal is monitored with an oscilloscope. In order for the laser spectrum to be visible on the scope, the laser beam must be incident on the spectrum analyzer window at a right angle. The critical step of alignment is ensuring that the reflection from the spectrum analyzer coincides with the incident beam. If the spectrum looks asymmetric or broader than the 10 MHz frequency resolution typically observed, it is possible that the spacing

between the mirrors needs adjustment. The spacing can be adjusted by loosening the lock on the interferometer and turning the silver ring inside. Optimal adjustment is achieved by tilting the interferometer mount until transmission peaks are maximized. Sometimes, additional transverse modes are visible on the spectrum. It is usually easy to verify that they arise from imperfections in alignment rather than from multimode laser operation. In the former case, if the laser frequency is tuned with the pzt, the size and location of these transverse modes will remain constant relative to the main longitudinal mode.

### 3.2.3 Fiber Amplifiers

Ytterbium-doped fiber amplifiers are used to boost the diode laser light output at 1083 nm in order to facilitate studies of fine structure interval dependences on optical power. The units are YAM-3PM polarization-maintaining amplifiers manufactured by IPG Photonics. They are specified to increase light power output by over 30 dB, but in practice this figure is as low as about 10 dB. The laser spectrum is only about 50 kHz in width, and this narrow spectrum at high output powers could lead to instabilities such as stimulated Brillouin scattering [44] in the doped fiber. The amplifier used with the scan laser had polarization instability problems that were fixed by IPG Photonics, and both amplifiers had pre-amp problems that were fixed by the company. The performance of the units, however, still does not reach the specified level. Despite these problems, the amplifiers are helpful in the studies of systematic power dependences.

The absorption and emission peak wavelengths of the ytterbium-doped fiber [45]

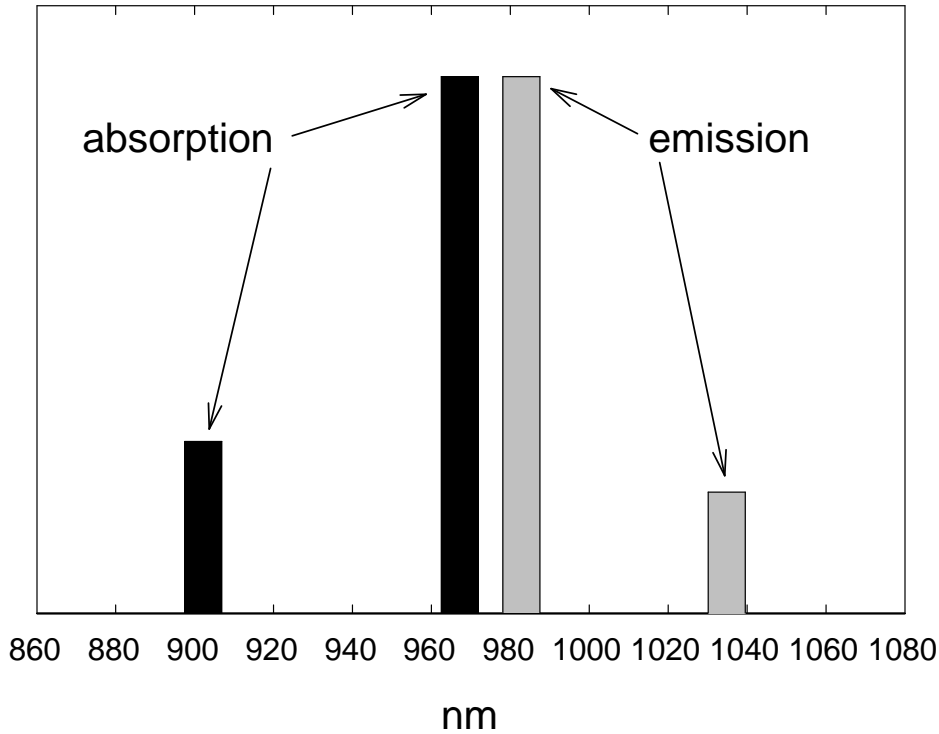


Figure 3.11: Absorption and emission peak wavelengths of Yb-doped fiber amplifiers [45].

are schematically shown in Fig. 3.11. The principle of amplifier operation is illustrated in Fig. 3.12. The active medium is pumped with a 978 nm laser diode, and the amplifier is seeded with 1083 nm light. The gain profile has a peak centered near 1027 nm, with one third of the peak gain at 1083 nm. The light emerging from the doped fiber is passed through a dichroic mirror that splits off any remaining pump light and outputs only the amplified 1083 nm light.

Light is coupled into the amplifiers using OZ Optics HPUC-23AF-1083-P-11AS-11-SP single mode polarization maintaining laser-to-fiber couplers. It is a simplified alternative to coupling light into bare fibers using three-axis translation stages. These devices transfer tilt degrees of freedom into translational degrees of freedom, and

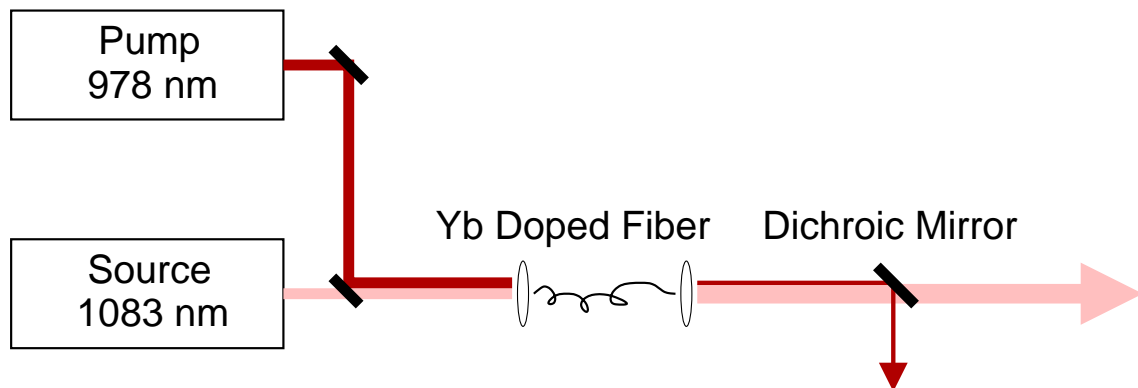


Figure 3.12: Fiber amplifier schematic diagram.

coupling is usually achieved faster than with bare fibers. As a first step, light from the laser has to pass through the coupler with no fiber attached to the coupler head, and the beam must remain straight and parallel to the optical table. Then a multimode fiber patchcord should be used to achieve initial alignment of the coupler. At this point, it is easy to reach high coupling efficiency, but the most important aspect to achieve is good output beam quality rather than high transmitted power. Light exiting the multimode fiber must be as close to single mode as possible, and if the output beam spot is uneven in intensity, alignment must be improved. Only then should a single mode fiber patchcord be used to optimize alignment. Finally, the fiber amplifier input is attached to the coupler, and remaining tilt adjustments are usually small.

### 3.2.4 Modulation and Frequency Shifting of Light

In order to subtract the large Doppler background from the probe transmission signal, the pump beam is modulated, and a lock-in amplifier detects probe transmission

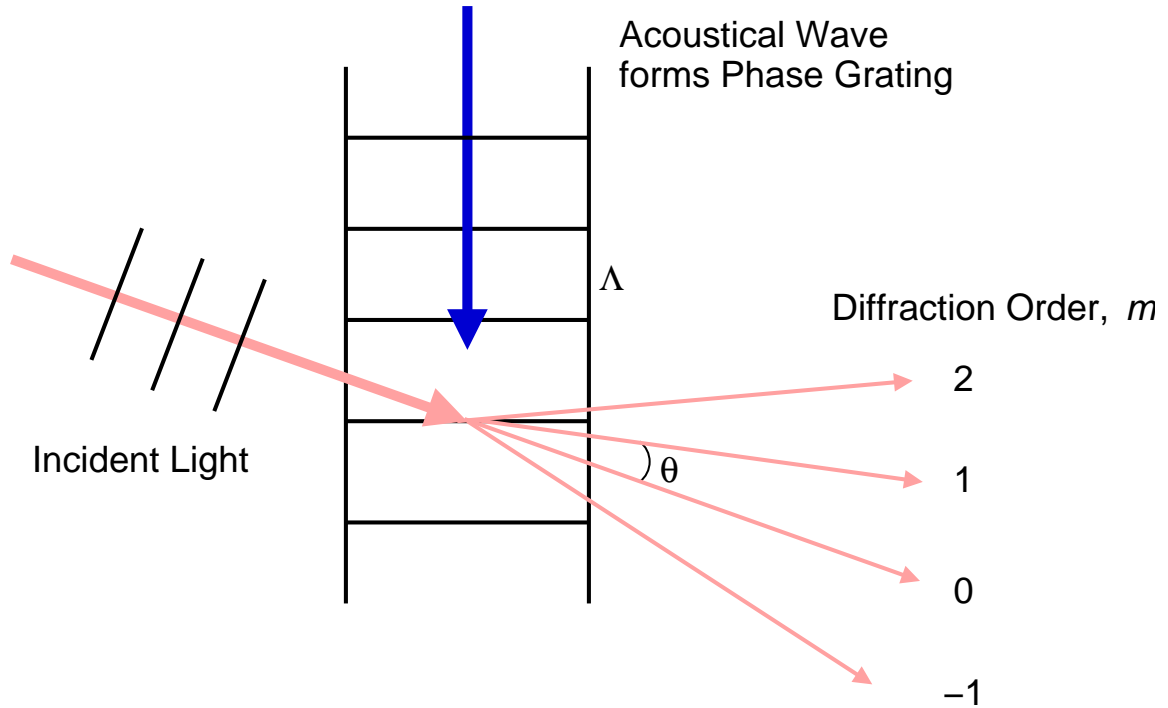


Figure 3.13: Acousto-optic effect.

synchronously with modulation of the pump. An additional benefit of this technique is reduction of the detection bandwidth of the saturation spectroscopy signal.

Acousto-optical modulators (AOMs) are used to frequency shift and modulate the pump beams of both scan and clock lasers. Inside the AOM, light is diffracted by a phase grating formed by an orthogonally directed acoustical wave. The phase grating is caused by change of the refractive index due to the photoelastic effect. Fig. 3.13 shows the principle of frequency shifting with an AOM. The angle  $\theta$  between different diffraction orders,  $1.5^\circ$  in this case, is given by

$$\sin \theta = \frac{m\lambda}{\Lambda}, \quad (3.9)$$

where  $\Lambda$  is the wavelength of the acoustical wave and  $m$  is the diffraction order. Upon

passing through an AOM driven at frequency  $f_0$ , the light is frequency shifted by

$$\Delta\nu = mf_0. \quad (3.10)$$

The AOMs operate at  $f_0 = 80$  MHz, and the superimposed modulation is typically a few tens of kilohertz. The modulation is square wave for the scan laser, and sinusoidal for the clock laser in order to prevent high harmonics of the modulation signal from interfering with efficient locking of the clock.

If the modulated pump beam is frequency offset from the probe beam by 80 MHz, the resulting saturation spectroscopy signal is offset from the center of the Doppler profile by 40 MHz, since pump and probe frequencies are scanned simultaneously. In order to keep the saturation signal closer to the flattest part of the Doppler profile, the probe beam of the scan laser is frequency shifted by 78 MHz using an identical AOM. As a result, the saturation signal is only 1 MHz away from the center of the Doppler profile, and corresponds to the atomic velocity group of about 1 m/s. The probe beam offset is not chosen to be exactly 80 MHz, since interference effects of scattered pump and probe would lie within the detection bandwidth leading to a poor signal to noise ratio.

A mechanical chopper wheel SRS540 has also been used to chop the pump beam of the clock laser at 1.5 kHz. An AOM, however, allows chopping at higher frequencies which reduces noise from laser amplitude fluctuations in the lock-in detection bandwidth.

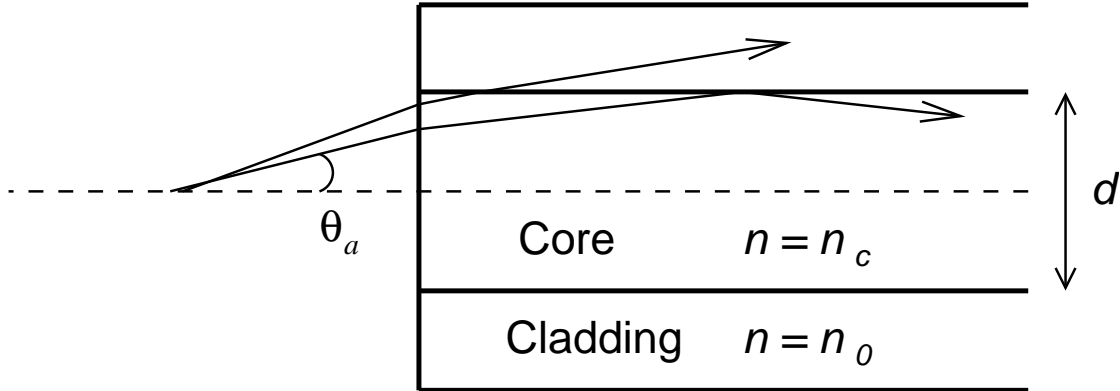


Figure 3.14: Spatial filtering of optical beams with single mode optical fiber.

### 3.2.5 Spatial Filtering of Light

To ensure that optical beams contain a single spatial mode, optical fibers positioned after the AOMs in the scan laser pump and probe paths filter out higher spatial modes. Spatial filtering with single mode optical fibers is illustrated in Fig. 3.14. If the refractive indices of the fiber core and cladding are  $n_c$  and  $n_0$ , respectively, Snell's law gives the critical angle of incidence of light on the fiber face,  $\theta_a$ , also called the acceptance angle,

$$\sin \theta_a = \sqrt{n_0^2 - n_c^2}. \quad (3.11)$$

If the incidence angle exceeds  $\theta_a$ , light does not propagate through the fiber. Numerical aperture (NA) is defined as

$$\text{NA} \equiv \sin \theta_a. \quad (3.12)$$

In order for the fiber to support only the lowest spatial mode of light, the requirement on the core diameter  $d$  is [46]

$$d < 2.4 \frac{\lambda}{2\pi(\text{NA})}, \quad (3.13)$$

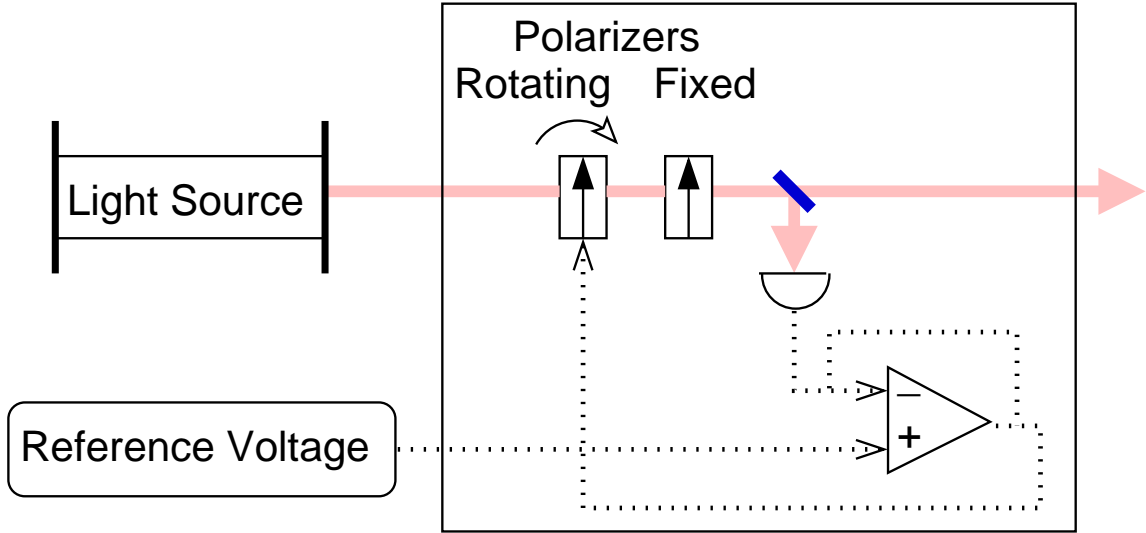


Figure 3.15: Optical power regulation.

and typically  $d$  is only a few optical wavelengths. For 1083 nm light, the single mode fiber diameter is about  $6 \mu\text{m}$ .

### 3.2.6 Light Intensity Stabilization

Thorlabs CR200-B laser intensity stabilizers in the pump and probe paths reduce low-frequency laser amplitude noise. A dc voltage is applied to the units from the computer using the DAC, or manually by turning the potentiometers on the units. The calibration of the input voltage is usually done by measuring optical power just outside the helium cell, as losses along the paths vary depending on the optical elements that are used. The intensity stabilizers were measured to be effective up to about 1 kHz and provide about 15 dB of noise reduction at 60 Hz.

The principle of intensity stabilization is shown in Fig. 3.15. A small portion of incident light is sampled by a photodiode, and the signal is compared to the setpoint.

Electrical feedback is sent to a variable attenuator that consists of a polarizer pair. Outgoing light is vertically polarized, and the incoming light polarization should be as close to vertical as possible for optimal performance. It is important to prevent back-reflected light from entering output ports of the intensity stabilizers, as it leads to poor performance. Optical isolators are used for this purpose.

### 3.2.7 Polarization Control

For studies of optical pressure on helium atoms, it is important to rotate the polarization direction of one of the laser beams entering the cell. For this purpose, a Newport 10RP32-1064 half-wave plate is mounted in a Newport PR50 motorized rotation stage. The stage is computer controlled to  $0.01^\circ$  resolution. For most fine structure interval data collection, the wave plate is positioned to preserve vertical polarization. Thorlabs GTH10 Glan-Thompson polarizers with specified extinction ratios of  $10^5$  are placed in the paths of pump and probe beams, including one just before the rotating wave plate. The polarizers are positioned to transmit vertically polarized light.

### 3.2.8 Beam Expansion

Special Optics 50-51-10X-1083 laser beam expanders increase the pump and probe beam diameters from about 2 mm to 2 cm. This reduces optical intensity while keeping total power unchanged, and leads to better signal to noise ratios while reducing saturation effects. Moreover, large optical beam diameters minimize the effects of transit time broadening and wavefront curvature. The beams are passed through 8

mm diameter apertures in order to confine the saturation signals to central portions of the beam intensity profiles. The pump and probe expanders are equidistant from the helium cell, and the beams are well collimated inside the 2.5 cm diameter cell.

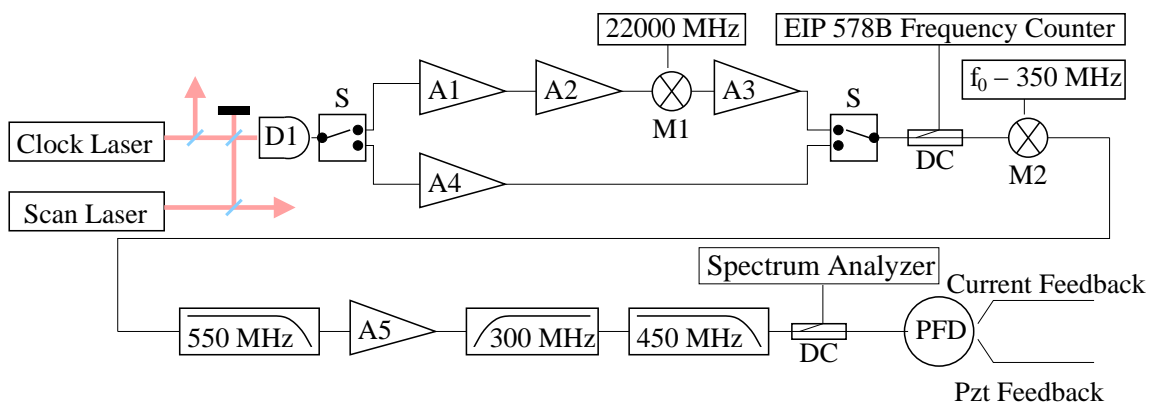
### 3.2.9 Optical Detection

Probe light transmitted through the cell is detected with a Thorlabs PDA400 amplified InGaAs detector. The active face of the detector is about 1 mm<sup>2</sup>. The output of the detector is sent to a SRS830 digital lock-in amplifier typically set to a 1 ms time constant and a roll-off of 24 dB per octave. The amplified internal reference of the lock-in drives the AOM signal for the pump beam amplitude chop.

## 3.3 Microwave System for Laser Frequency Control

The scan laser frequency has to be precisely tuned in order to sample line shapes of the  $2^3\text{S} - 2^3\text{P}$  helium transitions. It is phase-locked to the clock laser frequency reference, and the offset frequencies are about 6, 8, and 38 GHz for the  $2^3\text{S}_1 - 2^3\text{P}_2$ ,  $2^3\text{S}_1 - 2^3\text{P}_1$ , and  $2^3\text{S}_1 - 2^3\text{P}_0$  transitions, respectively.

Due to a large disparity between offset frequencies for the different intervals, two distinct paths have to be used for the microwave beat signal, as shown in Fig. 3.16. The clock and scan lasers beat on a 40 GHz photodetector D1, and a computer-controlled TTL switch S directs the signal along either the lower frequency path for  $2^3\text{S}_1 - 2^3\text{P}_2$  and  $2^3\text{S}_1 - 2^3\text{P}_1$ , or the higher frequency path for  $2^3\text{S}_1 - 2^3\text{P}_0$ . The paths



- D1: New Focus 1011 DC – 40 GHz photodetector  
 S: Dynatech FSCM 50667 DC – 40 GHz switch  
 A1: MITEQ JS4-26004000-40-5A amplifier  
 A2: MITEQ AMF-5F-260400-50-8P amplifier  
 A3: MITEQ AFS4-06001800-40-LN amplifier  
 A4: MITEQ AFS4-05001000-14-10P-4 amplifier  
 A5: MITEQ AM-3A-000115 amplifier  
 M1: MITEQ TB0440LW1 mixer, 4–40 GHz  
 M2: REMEC MM134P-1 mixer, 1.5–26.5 GHz  
 DC: directional coupler  
 PFD: Phase Frequency Detector circuit

Figure 3.16: Microwave and rf components for the diode laser offset lock.

are recombined with an identical switch after amplification, but first the  $2^3S_1 - 2^3P_0$  signal is mixed down to about 16 GHz using a 22 GHz local oscillator. All signals then follow the same path. A directional coupler splits off -13dB of the signal power to the frequency counter that is read by the computer in order to ascertain the proximity of the laser frequency to one of the helium lines. The signal is mixed down to 350 MHz, further amplified, and bandpass-filtered. Another directional coupler sends part of the signal to the spectrum analyzer to monitor the quality of the beatnote, while the main portion of the signal goes to a phase frequency detector and compensation circuit described below that in turn provides two feedback paths to the scan laser. The low-frequency feedback controls the pzt that sets the extended cavity length, and the high-frequency feedback modulates diode current.

The phase-locked loop for offset frequency relies on the ADF4111 chip. The chip contains a low-noise digital phase frequency detector and a precision charge pump, as well as a programmable divide-by-N feature to divide the frequency of  $RF_{IN}$ . The phase detector and compensation circuit is shown in Fig. 3.17.  $RF_{IN}$  is the input for the mixed-down offset frequency, and  $REF_{IN}$  is the input for the local oscillator frequency near 15 MHz. All functions of ADF4111 are computer-controlled through a fiber serial controller board with an optical fiber interface. The multiplexed MUX-OUT output is wired to the Lock Detect feature of the chip that sends a high or low TTL signal to an LED and to the computer, depending on whether or not  $RF_{IN}$  is phase-locked to the local oscillator.

The output of ADF4111 is the charge pump CP. The CP filter has a pole at dc and a zero at about 200 Hz. The low-frequency pzt feedback path consists of a times-two

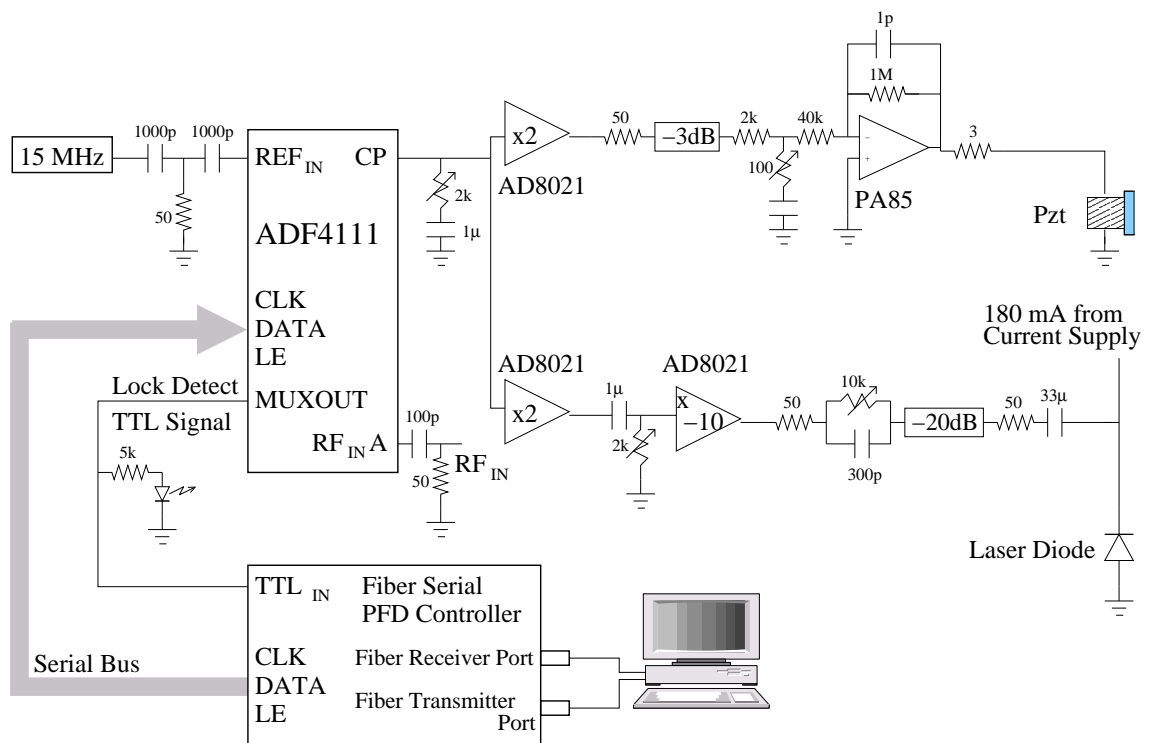


Figure 3.17: Phase frequency detector and compensation circuit for the diode laser offset lock. Resistor values are in ohms, capacitor values are in farads.

buffer, an attenuator, a lag-lead filter with an 80 Hz pole and a 15 kHz zero, and a high voltage pzt driver. The pzt feedback operates stably in the presence or absence of current feedback. The high-frequency current feedback path consists of a times-two buffer, a dc-blocking high-pass filter with a pole at 200 Hz, a times-ten inverting amplifier, a phase-advance circuit with a 0.5 MHz zero and a 10 MHz pole, and a large dc-blocking capacitor on the laser diode. The effect is that the scan laser frequency is locked to that of the clock laser, with feedback to the pzt correcting fluctuations less than 200 Hz, and the current feedback correcting fluctuations between 100 Hz and 1 MHz.

The locked beatnote is shown in Fig. 3.18. Trace (a) is taken with only the pzt feedback. Trace (b) is taken with both the pzt and current feedback. It demonstrates that the lock loop bandwidth is about 0.5 MHz, and prominent noise spikes are visible within the loop bandwidth. These 200 kHz spikes are more clearly visible on trace (c) that is taken with a 1 MHz frequency span. Trace (d) shows the beatnote within 0.1 MHz of the carrier. Its broadening is due to the residual low-frequency noise. The beatnote locked with pzt and current feedback is much narrower than the spectral width of the individual lasers, which is about  $\sqrt{2}$  times less than the width of the slowly locked beatnote on trace (a).

The 200 kHz noise spikes on the locked offset frequency were determined to originate in the commercial current supply used to power the scan laser diode. The same lock loop was tested using a homemade current supply with low high-frequency noise, and the noise spikes disappeared. If the homemade supplies are shown not to broaden the laser line width due to low-frequency noise, and are set up to be computer

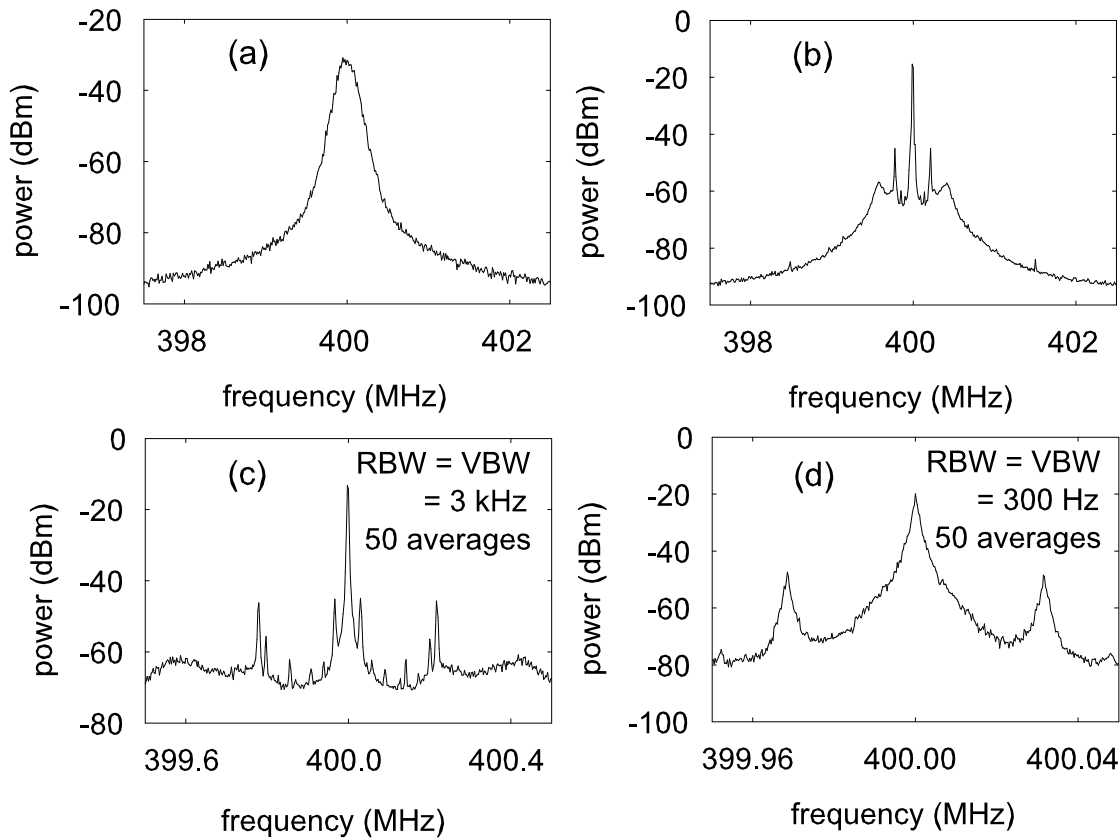


Figure 3.18: Locked beatnote between the scan and clock lasers. (a) Only the pzt feedback path is closed. (b) Both the pzt and current feedback paths are closed. The loop bandwidth of about 0.5 MHz is marked by the shoulders of the beatnote. The narrow spikes near 200 kHz are most likely due to noise from the current supply. (c) Same as (b), with a 1 MHz frequency span. Spikes are clearly visible on this trace. (d) Same as (b) and (c), with a 0.1 MHz frequency span. Besides additional noise spikes near the carrier, this scan shows residual low-frequency noise on the beatnote that prevents it from more closely resembling a delta function. Nevertheless, the 2 kHz beatnote is much narrower than the 50 kHz spectral widths of the individual lasers.

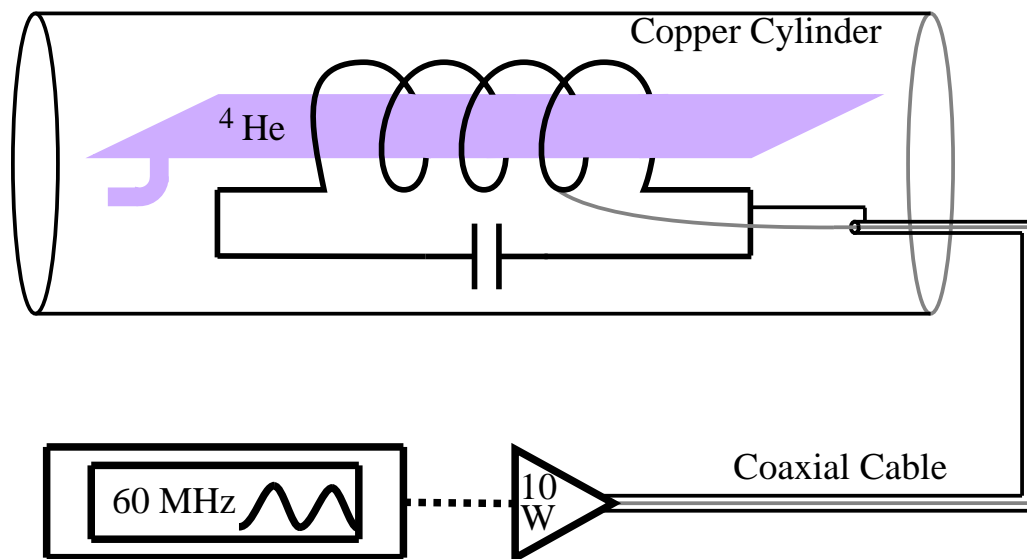


Figure 3.19: Rf discharge setup for metastable helium production in the cell.

controlled, they can be used in the measurements instead of the commercial units.

### 3.4 Production of $2^3\text{S}$ Metastable Helium

Metastable helium atoms are produced with an rf discharge illustrated in Fig. 3.19. The cell is surrounded by eight turns of thick silver-plated wire that forms a tuned circuit with a parallel capacitor. The assembly is enclosed in a cylindrical copper cavity to improve the quality factor of the resonance. The circuit resonates at about 60 MHz. This frequency can be increased by decreasing the value of the capacitor, the number of turns in the coil, as well as by using a copper cylinder with a smaller diameter. Several watts of power are typically delivered to the coil.

The presence of metastable triplet helium in the cell is confirmed by monitoring single-beam transmission of light on resonance with the  $2^3\text{S} - 2^3\text{P}$  transition. The

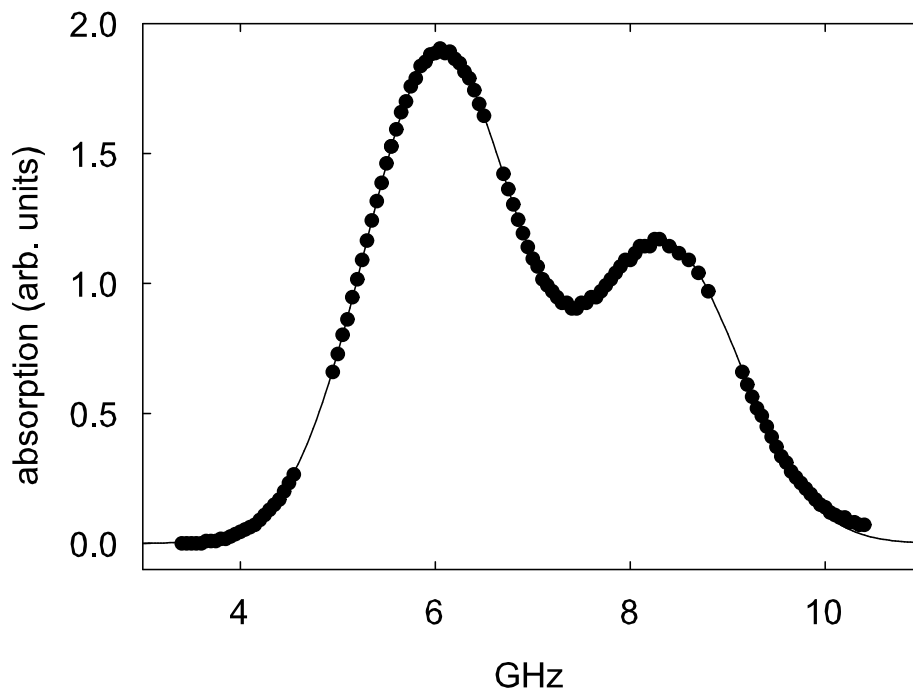


Figure 3.20: Doppler-broadened profile of the  $2^3S_1 - 2^3P_1$  and  $2^3S_1 - 2^3P_2$  transitions observed when the scan laser offset frequency is varied and single-beam transmission is measured. The line corresponds to a fit to two Gaussians with equal widths. Gaps in this profile are due to mode hops of the laser.

frequency of the scan laser is varied, and transmitted light power through the cell,  $t$ , is recorded. If  $t_0$  is the transmission in the absence of helium or away from the resonance, then the absorption coefficient  $\alpha$  is proportional to  $-\ln(t/t_0)$ , since  $t = t_0 e^{-\alpha L}$ , where  $L$  is the length of the cell. This quantity is plotted in Fig. 3.20 in the vicinity of  $2^3S_1 - 2^3P_1$  and  $2^3S_1 - 2^3P_2$ .

Assuming thermal equilibrium in the presence of discharge power and heat dissipated from magnet coils, the atoms follow a Maxwellian velocity distribution [47] such that the density of atoms  $N(v_x)$  with velocity  $v_x$  in the direction of laser propagation is

$$N(v_x) = \frac{N}{v_D \sqrt{\pi}} e^{-(v_x/v_D)^2}, \quad (3.14)$$

where  $N$  is the total number of atoms, and the most probable velocity in the Doppler profile  $v_D$  depends on temperature  $T$  as

$$v_D = \sqrt{\frac{2kT}{m}}. \quad (3.15)$$

Therefore, if the standard width of the Gaussian line profile is  $\Delta\omega_D$  and the laser frequency is  $\omega$ , the temperature of the atoms is found from

$$T = \frac{mc^2}{k} \left( \frac{\Delta\omega_D}{\omega} \right)^2. \quad (3.16)$$

The Doppler line shape in Fig. 3.20 yields a temperature of 330 K for the metastable atoms. The average atom velocity,

$$\bar{v} = \sqrt{\frac{8kT}{\pi m}}, \quad (3.17)$$

yields the second-order Doppler shift [47]

$$\delta\omega_{D2} = -\omega \frac{\bar{v}^2}{2c^2} = -2.68 \text{ kHz}. \quad (3.18)$$

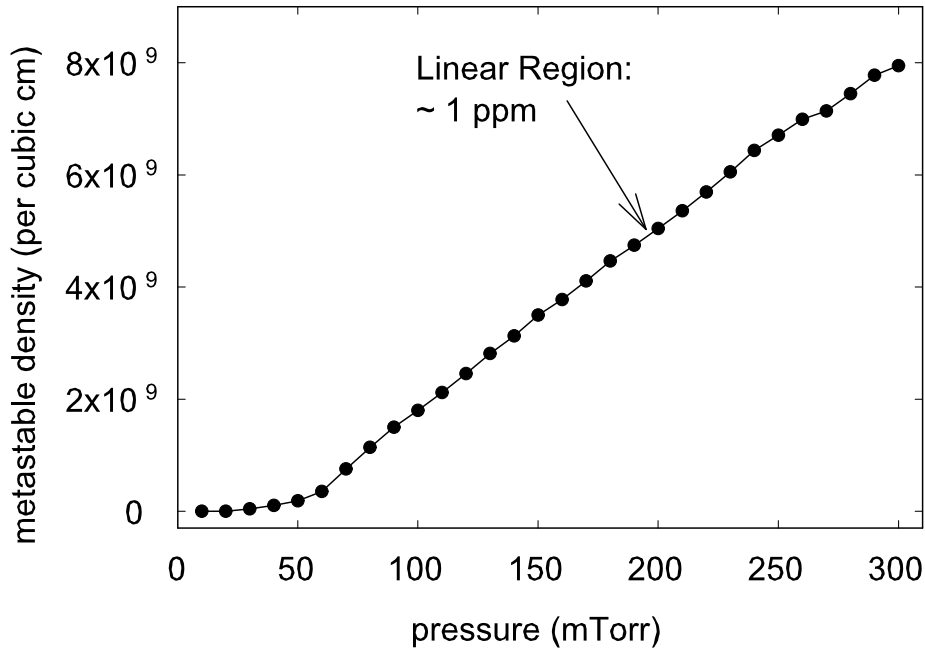


Figure 3.21: Density of metastable  $2^3\text{S}$  helium atoms in the discharge cell as a function of pressure, estimated from single-beam absorption. Below 50 mTorr, discharge is ineffective. In the linear region at higher pressures, the fraction of  $2^3\text{S}$  atoms is on the order of 1 ppm.

The second-order Doppler shift cancels for fine structure intervals, but must be taken into account in a measurement of  $2^3\text{S} - 2^3\text{P}$  optical transitions. The width illustrates the importance of Doppler-free spectroscopy which eliminates the effect of the first order Doppler shift.

For a metastable helium sample at 330 K, the most probable velocity along the laser beam propagation direction is  $v_D = 1.2 \times 10^5$  cm/s and the average velocity is  $\bar{v} = 1.4 \times 10^5$  cm/s, corresponding to kinetic energies of 0.030 eV and 0.041 eV, respectively.

The single-beam absorption technique gives a rough estimate of the density of metastable atoms in the cell. Transmission through the cell is recorded as a function

of pressure. The relationship between incident light power  $i$  and transmitted power  $t$  is

$$t = ie^{-\alpha L} = ie^{-n'_* \sigma_0 L}, \quad (3.19)$$

where the cell length  $L = 0.15$  m,  $\alpha$  is the absorption coefficient,  $\sigma_0$  is the resonant absorption cross section, and  $n'_*$  is the density of metastable He\* in the resonant velocity group. It follows that

$$n'_* = \frac{-\ln(t/i)}{\sigma_0 L}. \quad (3.20)$$

The total metastable density  $n_*$  is estimated as

$$n_* \approx n'_* \frac{\Delta\omega_D}{\gamma} \simeq 500n'_*, \quad (3.21)$$

where  $\Delta\omega_D$  is the Doppler-broadened line width and  $\gamma$  is the homogeneous pressure-broadened line width. This quantity is plotted in Fig. 3.21 as a function of pressure. At low pressures below 50 mTorr the discharge is not efficient. At higher pressures, the metastable density depends linearly on pressure, as expected.

Since the density of ground state helium atoms at room temperature is known to be

$$n = p \times 3.2 \times 10^{13} / \text{cm}^3 \quad (3.22)$$

where  $p$  is pressure in mTorr, the relative fraction of  $2^3\text{S}$  atoms in the cell can be estimated from Fig. 3.21. It is about 1 ppm at a 5 W discharge power, independent of pressure above about 50 mTorr. The small proportion of metastable atoms in the cell implies that most collisions contributing to thermalization and line shifts and broadening take place between metastable and ground state atoms, since collisions between two metastables are exceedingly rare.

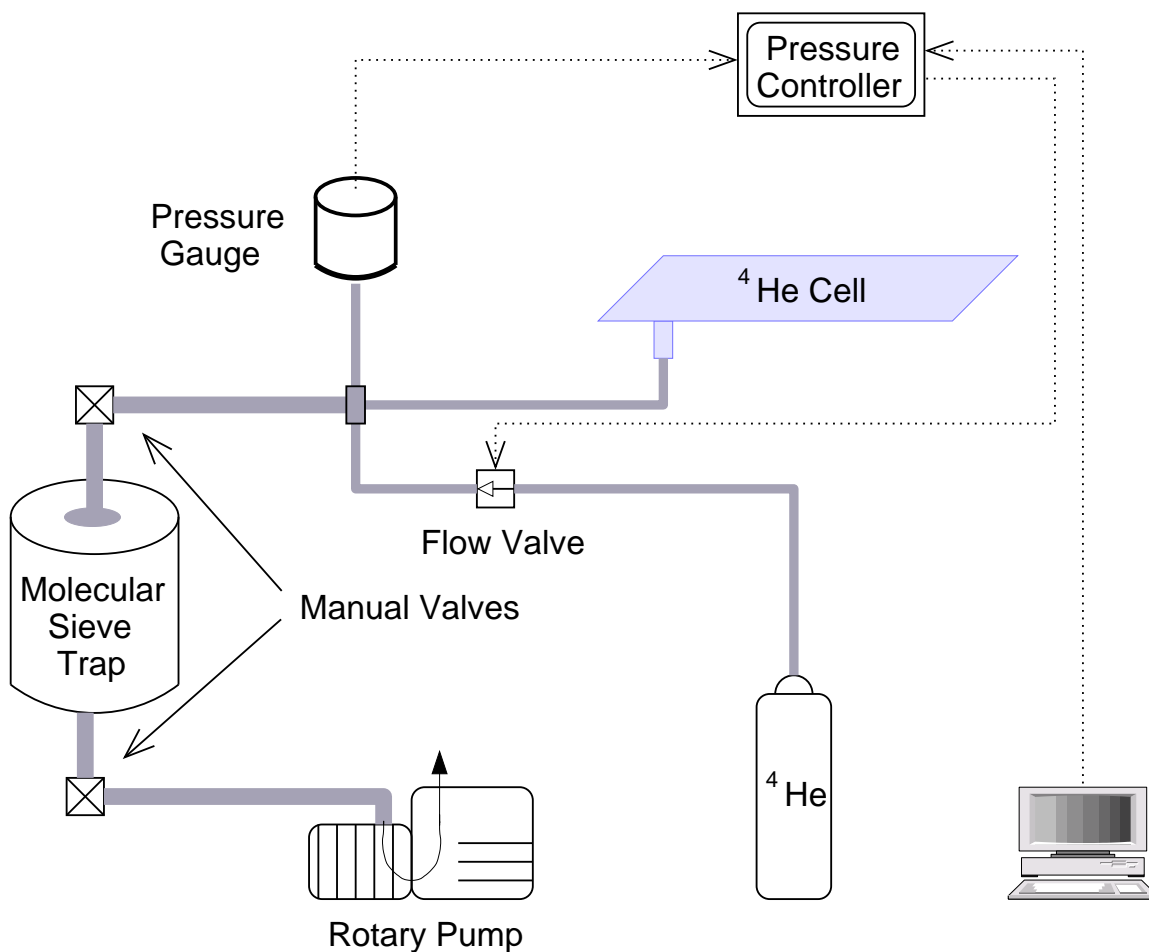


Figure 3.22: Pressure regulation system.

### 3.5 Pressure Regulation

A pressure regulation system controls the amount of helium in the discharge cell to allow the study of the effect of collisions on the fine structure intervals. The schematic of the system is shown in Fig. 3.22. Pressurized  $^4\text{He}$  of 99.999% purity is delivered to the cell from a bottle through a MKS 248 control valve. The valve precisely modulates the flow of helium when control current is applied to its internal solenoid, increasing the size of the orifice. The actual pressure is measured with the MKS 627 Baratron

temperature-controlled absolute pressure transducer. It has a variable capacitance sensor that compares the pressure to a fixed reference pressure of  $10^{-4}$  mTorr. The transducer can be zeroed by pumping on the cell with a turbo pump that is capable of achieving higher vacuum than the rotary pump. This procedure was performed before collecting the fine structure interval data. The pressure is regulated to 0.1 mTorr, which corresponds to pressure shifts of the  $2^3S_1 - 2^3P_J$  lines by less than 0.2 kHz, and to shifts of the fine structure intervals of about 10 Hz, and thus is more than sufficient resolution for studies of pressure-related effects in helium. The flow valve and pressure transducer are controlled with the MKS 250 controller. The gain and time constant for the pressure regulation system are manually adjusted on the face of the controller to provide the best regulation at the pressure range of interest. The cell is continuously pumped by the Varian SD-91 rotary vane vacuum pump. It is separated from the cell by a foreline trap that is placed between two manual valves. The foreline trap protects the helium cell from backstreaming pump oil. It contains molecular sieve material that is regenerated about once a year by baking the trap at  $250^\circ$  C while pumping on it.

## 3.6 $^3\text{He}$ Frequency Reference

The fine structure interval measurement requires only a stable optical frequency reference, rather than an absolute frequency standard, since the intervals depend on differences between  $2^3S_1 - 2^3P_J$  optical frequencies. The  $^3\text{He}$   $2^3S_1 - 2^3P_0$  ( $F = 1/2$ ) transition was chosen as the frequency reference since it is only several gigahertz away from the  $^4\text{He}$   $2^3S - 2^3P$  transition frequency. Fig. 3.23 compares  $^3\text{He}$  and  $^4\text{He}$  energy

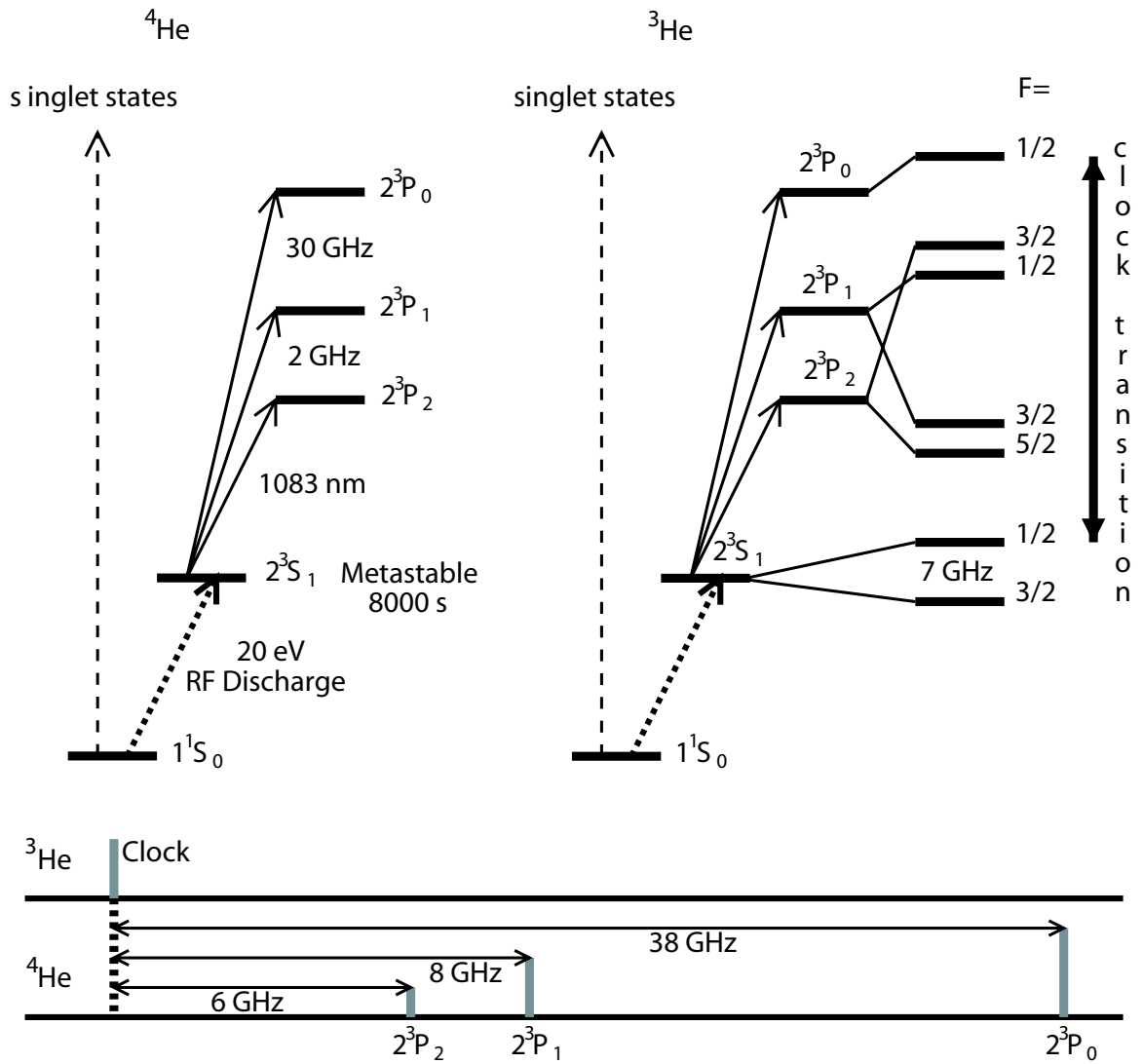


Figure 3.23: Comparison of  $^3\text{He}$  and  $^4\text{He}$  energy levels.

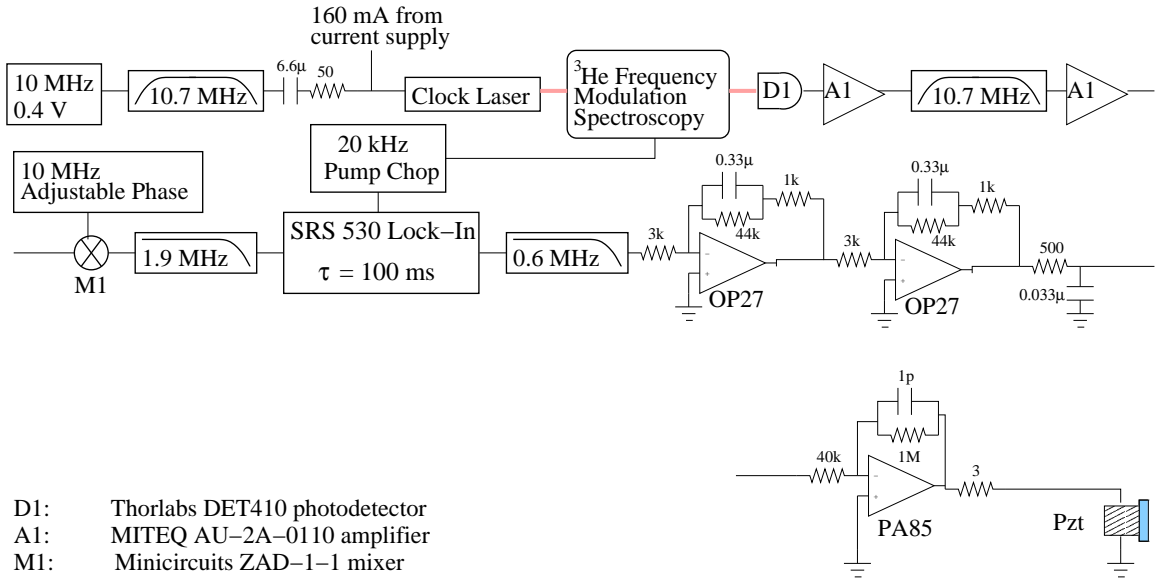


Figure 3.24: Clock laser lock to a  $^3\text{He}$  transition. Resistor values are in ohms, capacitor values are in farads.

levels and offset frequencies for  $^4\text{He}$   $2^3\text{S}_1 - 2^3\text{P}_{2,1,0}$  transitions. The clock laser is locked to this transition using frequency modulation spectroscopy.

Frequency modulation spectroscopy is closely related to saturation spectroscopy to be described in Sec. 3.7, with the difference that laser frequency is modulated. This frequency modulation translates into amplitude modulation of the Lorentzian absorption signal. Phase-sensitive detection then yields a derivative of the absorption signal. The derivative is dispersive, and its linear slope in the vicinity of the zero crossing provides the feedback signal for locking the laser to the transition.

The clock laser lock to  $^3\text{He}$  is illustrated in Fig. 3.24. The laser diode current is modulated at 10 MHz with a modulation index of about 1. Counter-propagating pump and probe beams overlap in a sealed 100 mTorr  $^3\text{He}$  cell. The probe transmission signal from Doppler-free spectroscopy in the cell is detected, amplified, and demodulated by a 10 MHz signal with an adjustable phase. A lock-in amplifier se-

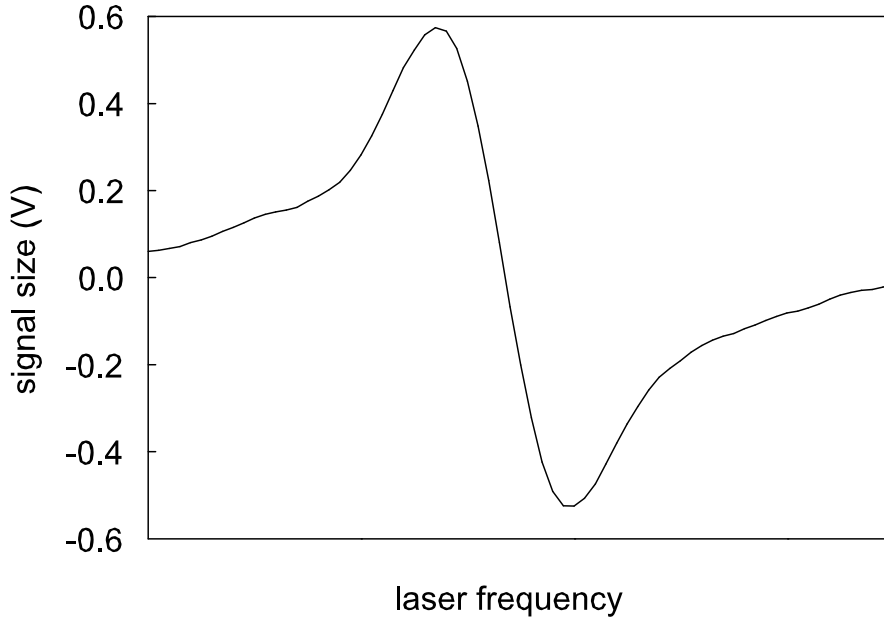


Figure 3.25: Averaged  $^3\text{He}$  derivative signal for locking the clock laser. This line shape is obtained by slowly sweeping the laser frequency.

lects the component of the signal at the pump chop frequency of about 20 kHz. After passing through a compensation circuit, the correction signal is fed back to the clock laser pzt driver. The averaged  $^3\text{He}$  lock signal is shown in Fig. 3.25.

The helium clock stability was measured with a GPS-referenced frequency comb. The comb repetition rate was stabilized to the clock laser and mixed down with a rubidium-clock based frequency synthesizer. The repetition rate was counted and plotted in Fig. 3.26 (a). Allan deviation of the helium clock measured against the rubidium clock is calculated from this trace and is shown in Fig. 3.26 (b). At time scales of a pair of line scans near 100 seconds, clock instability reaches the minimum value of  $3 \times 10^{-12}$ , which corresponds to 0.8 kHz. The details of this measurement will be in the thesis of D. Farkas.

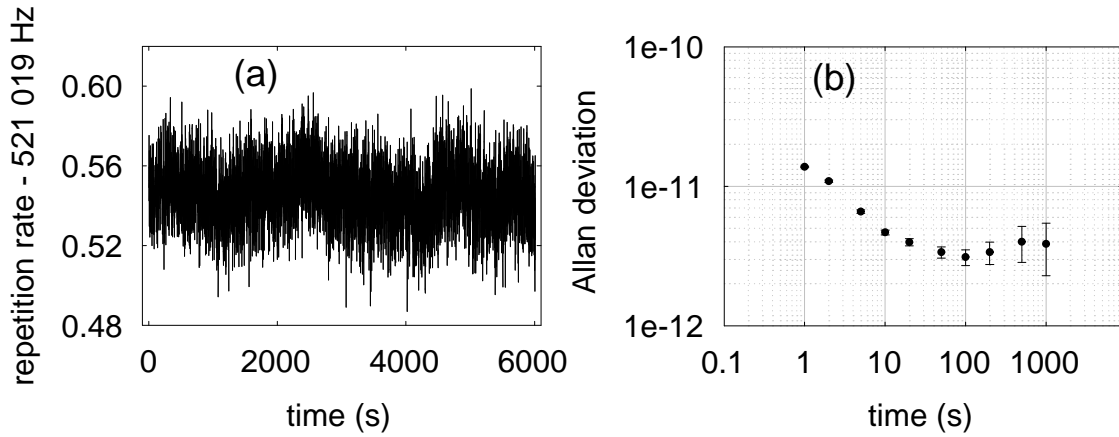


Figure 3.26: Helium clock stability measurement. (a) Repetition rate of a GPS-referenced frequency comb, counted and mixed down with a rubidium-clock based frequency synthesizer. The comb repetition rate is stabilized to the  $^3\text{He}$  clock laser frequency. (b) Allan deviation of the helium clock measured against the rubidium clock, calculated from the plot in (a).

## 3.7 Saturation Spectroscopy of $^4\text{He}$

### 3.7.1 Saturation Spectroscopy Technique

Saturation spectroscopy is a powerful technique that allows suppression of first-order Doppler broadening [47]. Without this suppression, the widths of the  $2^3\text{S} - 2^3\text{P}$  lines would exceed 1 GHz, rather than be close to the natural width of 1.6 MHz. In this velocity-selective method, signal comes from atoms resonant with two laser beams that are generally Doppler-shifted by different amounts. Fig. 3.27 illustrates the principle of saturation spectroscopy with counter-propagating pump and probe beams for a two-level atom. Figs. 3.27 (a) and (b) show velocity distributions of atoms in the ground and excited states, respectively, in the presence of the pump

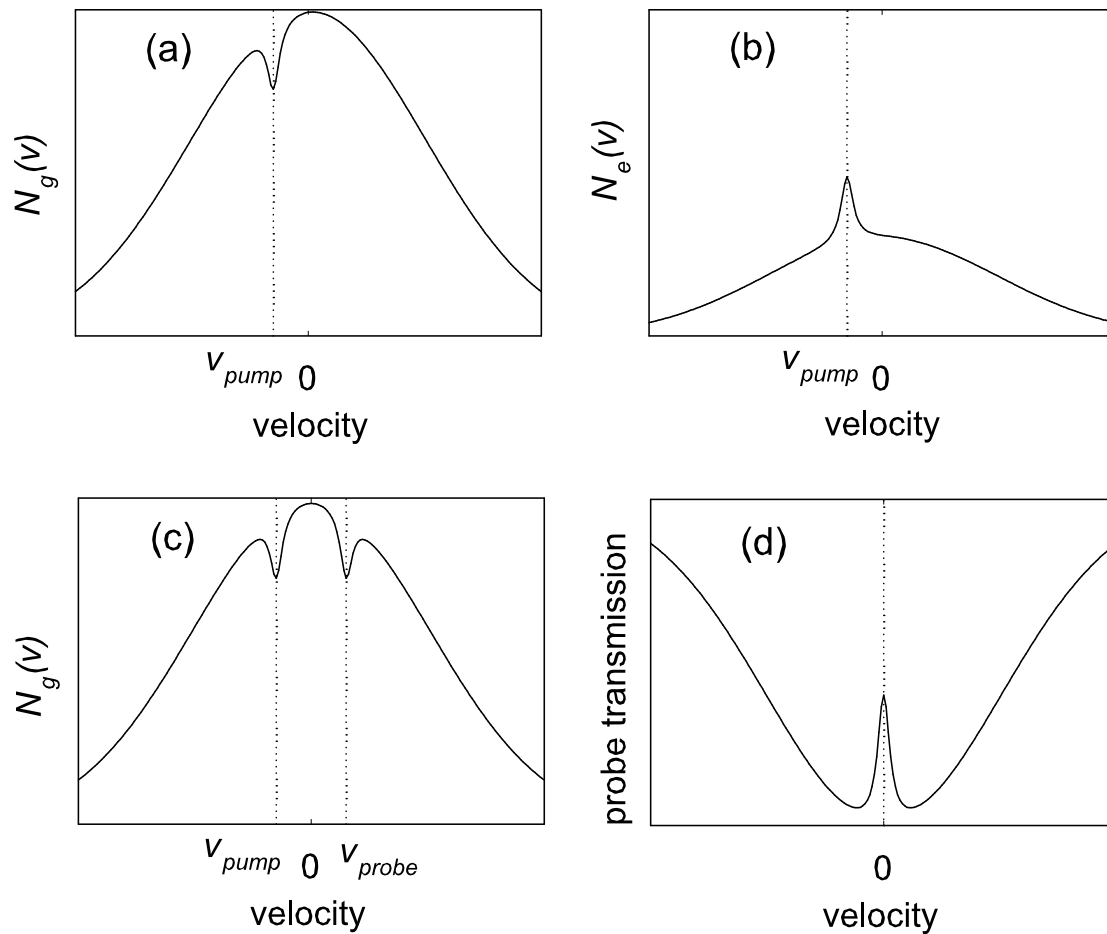


Figure 3.27: Principle of saturation spectroscopy. (a) Velocity distribution of ground state atoms in the presence of the pump beam. (b) Velocity distribution of excited state atoms in the presence of the pump beam. (c) Ground state velocity distribution in the presence of both pump and probe beams. (d) Probe beam transmission in the presence of the pump beam as a function of atomic velocity.

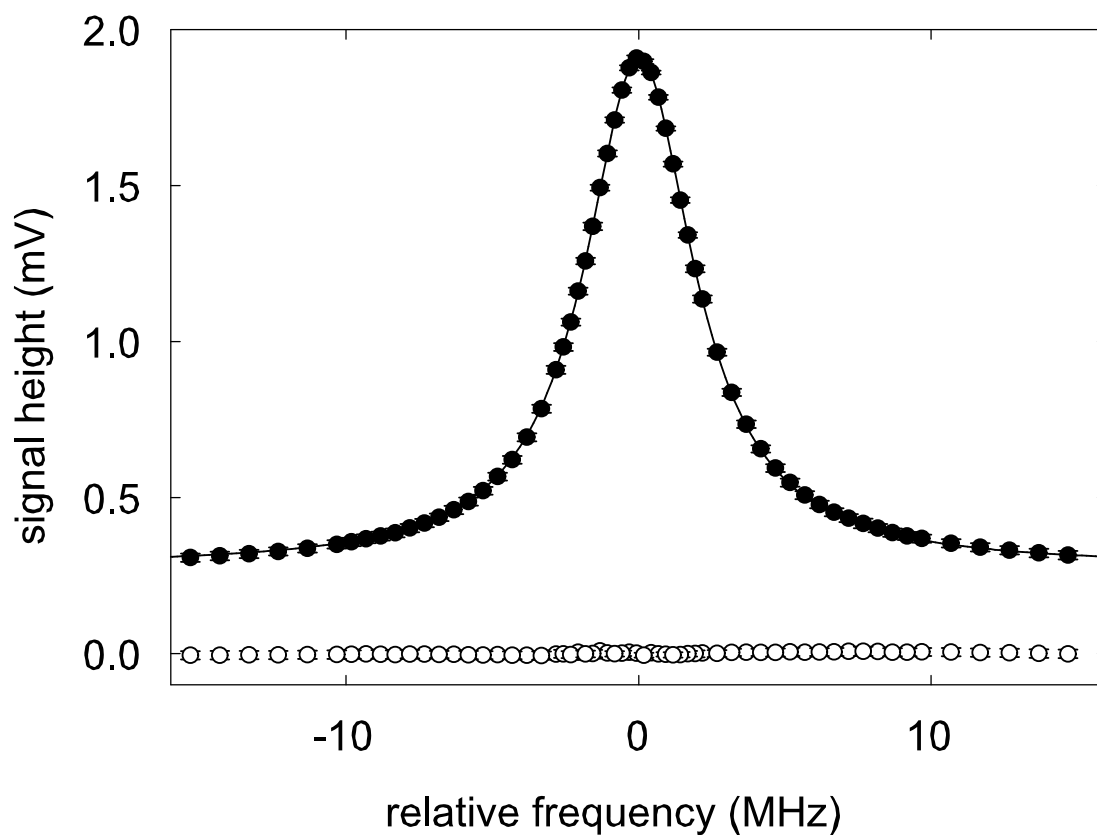


Figure 3.28: Saturation spectroscopy scan of the  ${}^4\text{He } 2^3\text{S}_1 - 2^3\text{P}_2$  transition, Lorentzian fit to the line shape, and fit residuals.

beam. Assuming  $\Delta\omega_L \ll \gamma \ll \Delta\omega_D$ , where  $\Delta\omega_L$  is the laser spectral width,  $\gamma$  is the homogeneous pressure-broadened atomic line width, and  $\Delta\omega_D$  is the Doppler-broadened line width, the pump beam excites a group of atoms moving with velocities  $[(\omega - \omega_0) \pm \gamma]/k$  along the direction of pump propagation, where  $\omega_0$  is the transition frequency. This leaves a so-called Bennet hole [48] in the ground state distribution  $N_g(v)$ . The number of atoms in the resonant velocity group increases for the excited state distribution  $N_e(v)$ . If the energy separation between the ground and excited states is much larger than the thermal energy, as is the case for metastable helium at room temperature,  $N_e(v)$  is essentially zero for all non-resonant velocities. When a counter-propagating probe beam is introduced, it burns another hole in the ground state distribution, as in Fig. 3.27 (c). If pump and probe have the same frequency  $\omega$ , this hole is centered at  $v = (\omega_0 - \omega)/k$ . As the laser frequency is tuned, probe transmission follows the broad Doppler-broadened line shape with a sharp increase at  $v = 0$ . At that point, both pump and probe are resonant with the same atoms, and the decrease of  $N_g(v = 0)$  caused by the pump is detected by the probe. Probe transmission as a function of atomic velocity is shown in Fig. 3.27 (d). In this experiment, there is a 2 MHz frequency offset between pump and probe, so the detected atoms are moving toward the probe beam with a velocity of  $1 \text{ MHz}/k \simeq 20 \text{ cm/s}$ . An example of a saturation spectroscopy  $2^3\text{S}_1 - 2^3\text{P}_2$  line scan is shown in Fig. 3.28.

If no magnetic field is applied to resolve Zeeman sublevels of the ground and excited states, the saturation spectroscopy picture is somewhat more complicated. Since pump and probe are polarized, only certain Zeeman sublevels are coupled by

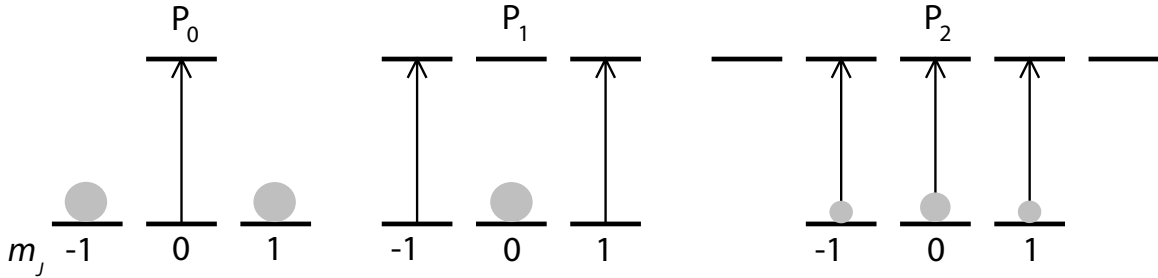


Figure 3.29: Optical pumping for  $2^3S_1 - 2^3P_{0,1,2}$  transitions, assuming linear and parallel pump and probe beam polarizations. Gray circles indicate steady-state populations.

the laser. Fig. 3.29 shows the bright and dark sublevels for a linearly polarized laser. For  $2^3S_1 - 2^3P_0$  and  $2^3S_1 - 2^3P_1$  transitions in steady state, population redistributes to the  $m = \pm 1$  and  $m = 0$  sublevels, respectively. Therefore, many atoms affected by the probe have been optically pumped into dark Zeeman sublevels, and the term *saturation spectroscopy* does not strictly apply, since the number of atoms in the excited  $2^3P_0$  or  $2^3P_1$  state is typically very low.

### 3.7.2 Implementation and Data Collection

The scan laser beam is split into pump and probe beams. Pump and probe are frequency-shifted with AOMs by 80 MHz and 78 MHz, respectively, spatially filtered, and expanded. The pump is chopped with a 30 kHz signal provided to an AOM by a SRS 830 lock-in amplifier. Probe transmission is detected by a photodiode and registered by the lock-in amplifier with a 1 ms time constant. This synchronous detection scheme allows subtraction of the broad Doppler background shown in Fig. 3.27 (d), leaving only what is essentially a Lorentzian signal limited in width by homogeneous pressure broadening.

LabVIEW code controls the data collection process. A data collection program takes as input the relevant experimental parameters such as pressure, optical power, transitions to be studied, and point patterns to be used in scanning line shapes. The computer controls the phase frequency detector for laser offset lock, and reads data from the lock-in amplifier for each scan laser frequency. Typically, about 100 readings are made at each frequency at a 512 Hz sampling rate. For a  $f_{JJ'}$  fine structure interval, the  $2^3S_1 - 2^3P_{J'}$  and  $2^3S_1 - 2^3P_J$  scans are alternated in an ABBA pattern. Subsequent pairwise subtraction gives the value of  $f_{JJ'}$ . The ABBA pattern helps cancel linear drifts of the reference frequency.

## Chapter 4

# Light-Pressure-Induced Frequency Shifts

The light-pressure effect presents a particular interest because of its strong manifestation in helium interacting with resonant optical radiation. It causes systematic frequency shifts of  $2^3\text{S} - 2^3\text{P}$  transitions and must be properly accounted for in the precision measurement.

The role of the pump beam in saturation spectroscopy is usually viewed in terms of exciting the atoms to the upper level and making them invisible to the probe. In reality, however, the pump also perturbs external atomic degrees of freedom, imparting a momentum kick each time a photon is absorbed. This modifies the velocity distribution of the sample, and leads to frequency shifts [49].

Light-pressure effects have been previously observed by other research groups. Grimm and Mlynek studied shifts of probe absorption profiles for closed transitions in ytterbium vapor [50, 51, 52] due to the dissipative light scattering force. Minardi

and coworkers encountered light-pressure shifts for closed and open transitions while working on the helium fine structure measurement in an atomic beam, and explained them [53, 54] through the scattering and dipole forces. They used fluorescence detection rather than probe transmission which led to an additional light intensity dependence of the frequency shifts. In both cases, atoms were described as two-level systems, and line shifts of up to about 20% of the natural width  $\Gamma$  were reported.

Light-pressure-induced shifts of  $2^3S - 2^3P$  helium lines that are degenerate in the absence of a magnetic field were observed in the course of fine structure measurements in a discharge cell. In particular, parallel and perpendicular pump and probe polarization configurations,  $\text{lin}\|\text{lin}$  and  $\text{lin}\perp\text{lin}$ , were studied. The first case can generally be described as a two-level system with or without loss, depending on the angular momentum of the excited  $2^3P$  state. The second case must be viewed as a multilevel system, and leads to line shifts as large as  $\Gamma/2$ . The sign of the line shift in a multilevel system depends on the relationship between the angular momenta  $J_e$  and  $J_g$ , where  $e$  and  $g$  are the excited and metastable states  $2^3P_J$  and  $2^3S_1$ . Moreover, if  $J_e \leq J_g$ , the dependence of the frequency shift on the parameter  $\tau$  that sets the duration of coherent pumping has a discontinuity and changes sign when  $1/\tau \sim \Gamma/2$ .

Previous studies of optical pressure mentioned above have relied on varying the laser beam diameter in order to vary the duration  $\tau$  of the pump beam interaction with the atoms, and hence to vary the size of the light-pressure-induced shift. This work shows that varying pressure in a gas cell allows a very clean characterization of this systematic effect. There is no uncertainty associated with having to model the intensity profile of the pump, as is the case when the laser beam diameter is varied.

Instead,  $\tau$  is inversely proportional to pressure  $p$  at sufficiently high pressures, with a proportionality constant that is determined from pressure broadening of the spectral line. Light-pressure-induced shifts then go away at high pressures as collisions quickly interrupt the interaction of the light and atoms. Of course, collisions in the cell lead to other line shifts, but if the pressure is low enough for these shifts to be linear, the line centers are simply extrapolated to zero pressure.

The results for the lin $\perp$ lin case are unexpected, since they show that smooth variation of a continuous experimental parameter such as pressure can result in a highly discontinuous behavior of the absorption line center. Moreover, they demonstrate that extreme dependences of line centers on polarization can occur even when no dependences are expected from standard saturation spectroscopy theory.

These studies reveal two ways of carrying out the measurements of helium fine structure intervals,  $f_{JJ'}$ , while reducing or eliminating the light-pressure systematic effect. The first method exploits different sensitivities to light polarization of  $2^3S_1 - 2^3P_J$  and  $2^3S_1 - 2^3P_{J'}$  optical transitions. A pump and probe polarization arrangement can be found that makes line shifts nearly identical, and subsequently they cancel upon calculation of the fine structure interval. The second method consists of resolving Zeeman sublevels of  $2^3S$  and  $2^3P$ , and inducing optical transitions between those sublevels of  $2^3S$  and  $2^3P_J$ , and  $2^3S$  and  $2^3P_{J'}$ , that have the same spontaneous-decay branching ratios from  $2^3P_J$  as from  $2^3P_{J'}$ . Light-pressure-induced shifts are then the same for both optical transitions, which leads to cancellation when fine structure intervals are computed. This method introduces additional systematic effects from magnetic shifts, but for moderate fields they are well understood and

easily corrected.

Light-pressure-induced line shifts are particularly strong in helium because of its small mass and large recoil. However, the effect may not be negligible for other more massive atoms. Line shifts are proportional to  $\epsilon_r \tau \propto \tau \hbar / (m \lambda^2)$ , where the optical interaction time  $\tau$  is limited by collisions, transit time, or other experimental constraints, and  $\epsilon_r$  is the recoil frequency. In cases of large  $\tau$  or small mass or wavelength, line shifts are considerable.

## 4.1 Theory of the Light-Pressure Effect for a Two-Level Atom

The light-pressure contribution to absorption and dispersion profiles in a gas of two-level atoms has been worked out by Grimm and Mlynek [50, 51]. The atoms have a resonance frequency  $\omega_0$ , natural line width (FWHM)  $\Gamma$ , and Doppler width  $\Delta\omega_D \gg \Gamma$ . The light field is a monochromatic traveling plane wave, which is a reasonable approximation for spatially expanded laser beams.

Doppler-free spectroscopy is typically described in terms of the pump beam saturating the transition and thus increasing probe transmission [47]. In this case, the internal quantum state of the atom is altered by the pump, and the transmission signal is a symmetric Lorentzian with the natural line width. However, external atomic states such as momentum are also affected by the pump. Pump photons cause atomic velocities to redistribute so that they no longer form a smooth Doppler profile. The measured probe transmission is sensitive to this deformation of the velocity profile.

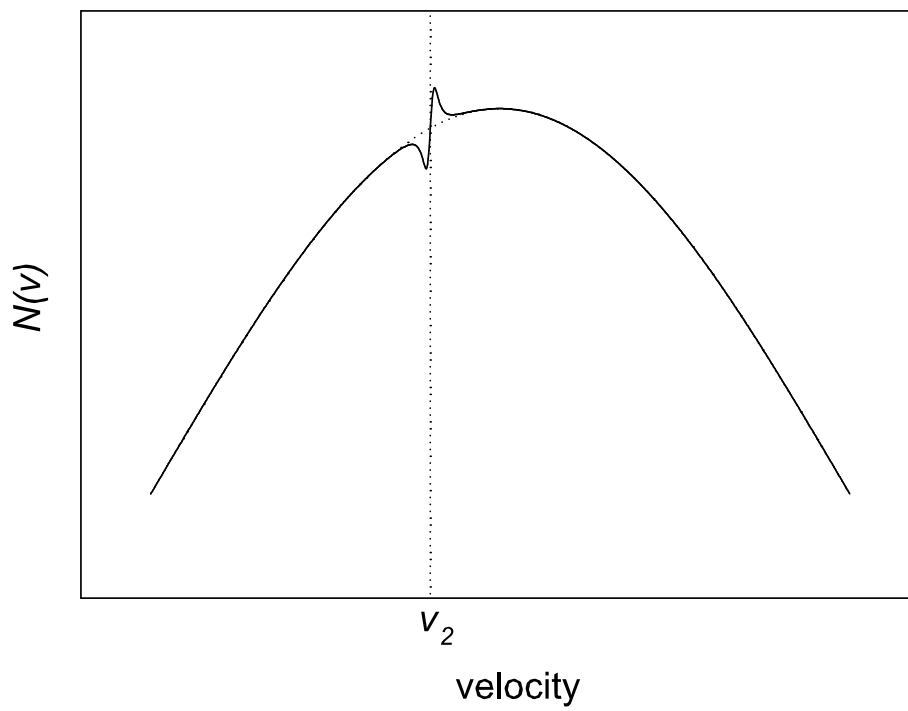


Figure 4.1: Doppler profile with a dispersive modification resulting from momentum transfer by the pump beam. In this example, atoms on the left half of the distribution are moving toward the pump which is red-detuned.

Each cycle of atomic excitation by the pump followed by spontaneous emission is characterized by an average momentum transfer of  $\hbar k$  from the laser field to the atom, where  $k = 2\pi/\lambda$  is the wave number. This momentum quantum corresponds to the angular recoil frequency of

$$\epsilon_r = \frac{\hbar k^2}{2m}. \quad (4.1)$$

For the  $2^3\text{S} - 2^3\text{P}$  transition in helium,  $\epsilon_r = 2\pi \times 42$  kHz, much smaller than  $\Gamma = 2\pi \times 1.6$  MHz. For very small recoils, optical pressure is described by the classical scattering force

$$F_s(v) = \hbar k \Gamma P_e(v), \quad (4.2)$$

where the excitation probability is

$$P_e(v) = \frac{s}{2} \frac{(\Gamma/2)^2}{k^2(v - v_2)^2 + (\Gamma/2)^2}. \quad (4.3)$$

Here  $s$  is the saturation parameter and  $v_2$  is velocity resonant with the pump. The initial one-dimensional atomic velocity distribution is a Doppler profile  $N_0(v)$ , and evolution of  $N(v)$  is described by the continuity equation [55]

$$\frac{\partial}{\partial t} N(v, t) + \frac{\partial}{\partial v} \left( \frac{\partial v}{\partial t} N(v, t) \right) + \frac{\partial}{\partial x} \left( \frac{\partial x}{\partial t} N(v, t) \right) = 0, \quad (4.4)$$

where  $x$  is the spatial coordinate along the laser beam propagation. Since the atomic ensemble is uniform in space,  $\partial/\partial x$  vanishes, and

$$\frac{\partial}{\partial t} N(v, t) + \frac{\partial}{\partial v} \left( \frac{\partial v}{\partial t} N(v, t) \right) = 0, \quad (4.5)$$

$$\frac{\partial}{\partial t} N(v, t) = -\frac{1}{m} \frac{\partial}{\partial v} [F_s(v) N(v, t)]. \quad (4.6)$$

Valid if the modification of  $N(v)$  is small, the first-order perturbative solution to this equation is

$$N(v, t) = N_0(v) - N_0(v_2) \frac{t}{m} \frac{\partial}{\partial v} F_s(v). \quad (4.7)$$

To obtain eq. (4.7), the unperturbed distribution  $N_0(v)$  was substituted into the right-hand term of eq. (4.6). It was also assumed that in the large-Doppler-width limit, the only velocity group affected by the scattering force  $F_s(v)$  is in the vicinity of  $v_2$  and thus  $N_0(v) \approx N_0(v_2)$  in the last term of eq. (4.7). In the case of a continuous laser excitation, velocity distribution reaches steady state  $N(v, t) = N(v)$ , and  $t$  in eq.(4.7) becomes  $\tau$ , the effective coherent interaction time of the pump with the atoms. For the closed transitions in this experiment,  $\tau$  is limited by collisions of the metastable atoms with ground state helium in the cell. With this substitution, the new velocity profile is

$$N(v) = N_0(v) + N_0(v_2) \epsilon_r \tau \frac{sk(v - v_2)\Gamma^3/2}{[k^2(v - v_2)^2 + (\Gamma/2)^2]^2}. \quad (4.8)$$

The extent of velocity modification is set by dimensionless parameters  $\epsilon_r \tau$  and  $s$  in eq. (4.8). The perturbative approach is justified if  $\epsilon_r \tau, s \ll 1$ . Fig. 4.1 shows the dispersive kink that appears on the Doppler profile as a result of photon recoil.

Propagation of the probe beam through the cell is equivalent to multiplication of its amplitude by a factor of  $e^{-A-iD} \equiv e^{-C}$ , where  $A$  and  $D$  are the absorption and dispersion coefficients, respectively. In terms of the optical response of individual atomic velocity groups,

$$C = \int_{-\infty}^{+\infty} N(v)c(v)dv. \quad (4.9)$$

Inside the integral,  $c(v)$  describes the internal and  $N(v)$  the external atomic degrees of freedom. When a pump beam is added to the probe to achieve Doppler-free signals,

the pump modifies not only the internal, but also the external degrees of freedom, affecting both  $c(v)$  and  $N(v)$ .

For weak pump intensities, only terms of  $\mathcal{O}(s^1)$  need to be kept in  $N(v)$  and  $c(v)$ . Written as linear expansions in  $s$ ,

$$c(v) = c_0(v) + sc_1(v), \quad (4.10)$$

$$N(v) = N_0(v) + sN_1(v). \quad (4.11)$$

Then

$$\begin{aligned} C &= \int_{-\infty}^{+\infty} N_0(v)c_0(v)dv + s \int_{-\infty}^{+\infty} N_0(v)c_1(v)dv + s \int_{-\infty}^{+\infty} N_1(v)c_0(v)dv \\ &\equiv C_0 + s(C_{\text{SAT}} + C_{\text{LP}}). \end{aligned} \quad (4.12)$$

In eq. (4.12),  $C_0$  denotes response in the absence of the pump, whereas  $C_{\text{SAT}}$  and  $C_{\text{LP}}$  describe effects due to saturation and optical pressure by the pump, respectively.

If the pump and probe are counter-propagating and their wave numbers are the same, the optical response functions at low intensities are [56]

$$c_0(v) = \frac{k\kappa}{\pi} \frac{1}{ik(v_1 - v) + \Gamma/2} \quad (4.13)$$

and

$$c_1(v) = -\frac{k\kappa}{\pi} \frac{1}{ik(v_1 - v) + \Gamma/2} \cdot \frac{(\Gamma/2)^2}{k^2(v_2 - v)^2 + (\Gamma/2)^2}, \quad (4.14)$$

where  $v_1$  and  $v_2$  are atomic velocities resonant with probe and pump, respectively, and  $\kappa \equiv \pi nL|d|^2/(2\hbar\epsilon_0)$  in terms of the dipole matrix element  $\vec{d}$ , sample length  $L$ , and number density  $n$ .

The saturation effect is given by

$$C_{\text{SAT}} = \int_{-\infty}^{+\infty} N_0(v)c_1(v)dv, \quad (4.15)$$

and

$$A_{\text{SAT}} \equiv \text{Re}(C_{\text{SAT}}) = -\kappa N_0(v_2) \frac{1}{2} \frac{1}{k^2(v_1 - v_2)^2/\Gamma^2 + 1}. \quad (4.16)$$

The light-pressure effect is given by a similar integral. According to eq. (4.12),

$$C_{\text{LP}} = \int_{-\infty}^{+\infty} N_1(v) c_0(v) dv. \quad (4.17)$$

Taking  $N_1(v)$  from eqs. (4.11) and (4.8) and  $c_0(v)$  from eq. (4.13),

$$A_{\text{LP}} \equiv \text{Re}(C_{\text{LP}}) = -\kappa N_0(v_2) \epsilon_r \tau \frac{k(v_2 - v_1)/\Gamma}{[k^2(v_1 - v_2)^2/\Gamma^2 + 1]^2}. \quad (4.18)$$

The total optical response of the gas to first order in  $s$  can now be determined.

The detuning parameter is

$$\delta \equiv \frac{k(v_2 - v_1)}{\Gamma} = \frac{\omega - \omega_0}{\Gamma/2}, \quad (4.19)$$

if the frequency of the pump and probe is  $\omega$ . The factor of 1/2 in the denominator appears because the last term of eq. (4.19) is expressed through the zero-velocity resonance frequency  $\omega_0$ . The Doppler-free absorption coefficient is

$$A_{\text{SAT}} + A_{\text{LP}} \equiv -\kappa N_0(v_2) X(\delta), \quad (4.20)$$

where

$$X(\delta) = \frac{1}{2(\delta^2 + 1)} + \epsilon_r \tau \frac{\delta}{(\delta^2 + 1)^2} \quad (4.21)$$

is a dimensionless function describing the Doppler-free line shape. This result for two-level atoms is derived by Grimm and Mlynek [52, 51] and is presented here to facilitate further discussion.

The first term of  $X(\delta)$  is the symmetric Lorentzian caused by saturation of the transition by the pump. The second term is antisymmetric in  $\delta$  and has the form of

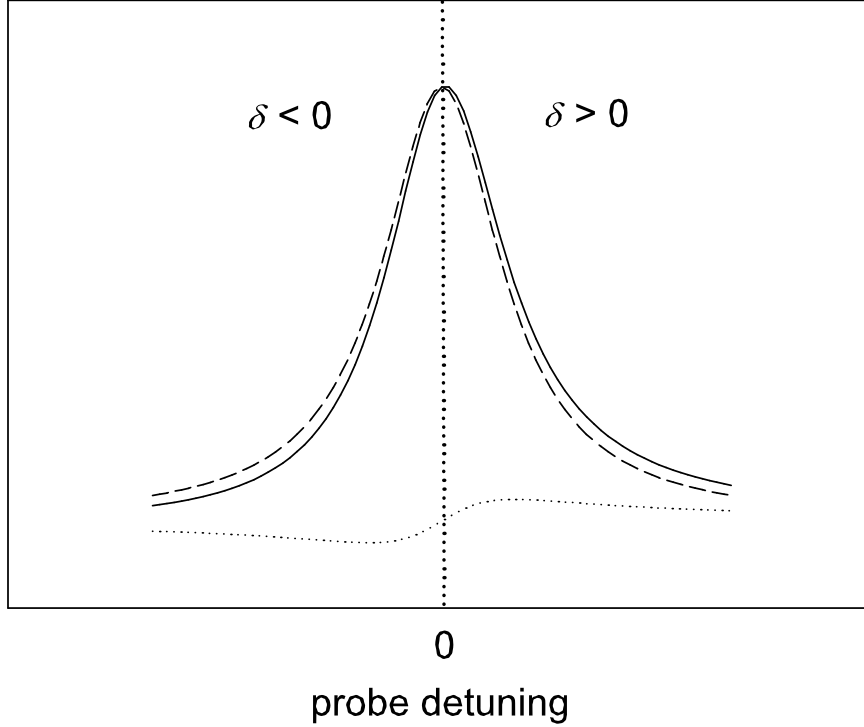


Figure 4.2: Optical pressure by the pump beam effectively superimposes a dispersive component (dotted line) onto the symmetric line shape (dashed line). Here,  $\epsilon_r\tau = 0.05$ , and the resulting line shape (solid line) is a blue-shifted Lorentzian.

a derivative of a Lorentzian, and is due to optical pressure. Note that the strength of the light-pressure effect relative to the saturation effect is independent of laser intensity in this limit of low  $s$ .

If  $\epsilon_r\tau$  is small (in this experiment,  $\epsilon_r\tau < 0.3$ ),  $X(\delta)$  can be viewed as the first two terms of an expansion of

$$F(\delta) = \frac{1}{2} \frac{1}{(\delta - \epsilon_r\tau)^2 + 1}. \quad (4.22)$$

Hence the effect of optical pressure is to shift the line center by  $\delta\omega = \epsilon_r\tau\Gamma/2$ . The observed line shape otherwise remains symmetrical and Lorentzian. Fig. 4.2 shows

the shifted line for  $\epsilon_r \tau = 0.05$ . If the interaction time  $\tau$  is proportional to  $1/p$ , the line center is blue-shifted by an amount inversely proportional to pressure.

Fig. 4.3 helps to visualize the physical reason for the line shift. At negative detunings  $\delta < 0$ , the probe interacts with an increased number of atoms due to the light-pressure kink in the Doppler profile. Its transmission is thus reduced, yielding a smaller signal on the red side of the saturation peak. At positive detunings  $\delta > 0$ , on the other hand, the probe encounters a depleted number of atoms and its transmission is higher, leading to a larger signal on the blue side of the saturation peak. The result is the line shape in Fig. 4.2 (solid line).

## 4.2 Light-Pressure Effect for Helium Atoms with Degenerate Magnetic Sublevels

### 4.2.1 Significance of the Optical and Collisional Time Constants

The sublevel structure of real helium atoms is more complicated than that of a simple two-level atom. An existence of more than one time constant related to the atomic population dynamics is a contrast to the two-level atom. The  $2^3S_1 - 2^3P_J$  helium transitions are closed systems, and the  $2^3S_1 - 2^3P_0$  and  $2^3S_1 - 2^3P_2$  transitions have optically dark  $2^3S$  sublevels to be discussed below. The presence of these dark states gives rise to an optical pumping time constant  $\tau_{op}$ . This time constant refers to the amount of time it takes to transfer the atomic population from

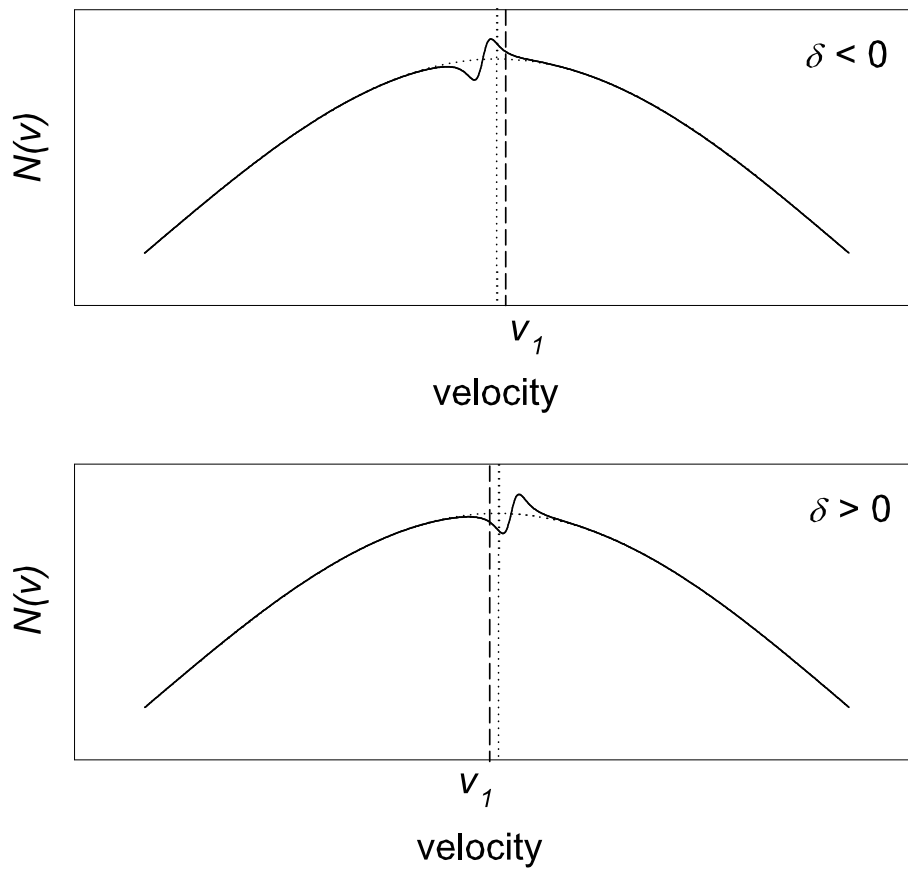


Figure 4.3: Explanation of the blue shift of the saturation peak. At negative detunings, the probe beam, which is resonant with atoms moving with velocity  $v_1$ , samples a larger number of atoms, yielding a lower transmission signal. At positive detunings, the probe samples fewer atoms, and its transmission is higher. The result is a blue-shifted line shape.

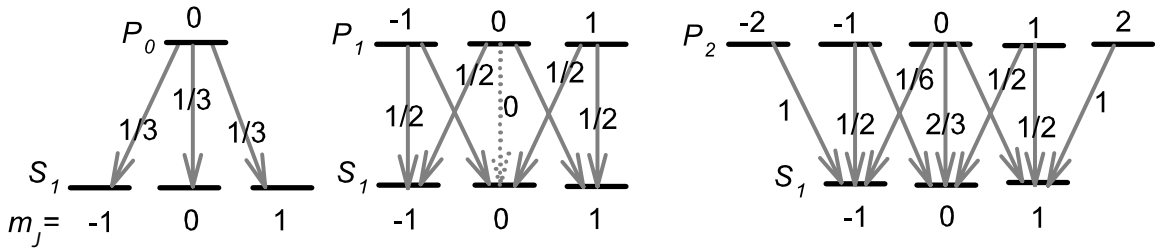


Figure 4.4: Level structures and coupling coefficients for the  $2^3S_1 - 2^3P_0$ ,  $2^3S_1 - 2^3P_1$ , and  $2^3S_1 - 2^3P_2$  transitions.

a ground state sublevel that interacts with the resonant laser to sublevels that do not. Collisions give rise to the collisional time constant inversely proportional to the helium pressure,  $\tau_c \propto 1/p$ , and  $\tau_c$  can be easily varied by changing the gas pressure. As will be shown, the competition of these two time constants results in resonances of the light-pressure-induced shift dependences on helium pressure.

### 4.2.2 The Multilevel Picture of Helium

The function  $X(\delta)$  of eq. (4.21) accurately describes the effect of optical pressure on the saturation line shape only for a two-level atom. The actual energy levels of helium contain  $2J + 1$  degenerate Zeeman sublevels that are important in optical pumping since the laser is polarized. In all three optical helium transitions,  $2^3S_1$  is the effective ground state. Its sublevels are  $m_J = \pm 1$  and  $m_J = 0$ , and it has a degeneracy of 3. Excited states  $2^3P_0$ ,  $2^3P_1$ , and  $2^3P_2$  have degeneracies of 1, 3, and 5, respectively. The level structures and coupling strengths are shown in Fig. 4.4. In the following discussion, the quantization  $\hat{z}$ -axis points in the vertical direction. It is also the direction of the probe beam polarization, which is kept constant. Thus, for

example, a  $\hat{z}$ -polarized beam tuned to  $2^3S_1 - 2^3P_1$  couples the  $m_J = \pm 1$  sublevels of the ground state to the  $m_J = \pm 1$  sublevels of the excited states such that  $\Delta m_J = 0$ , but does not affect the  $m_J = 0$  sublevels since the coupling coefficient vanishes for that particular transition. Then after a few cycles of photon absorption and emission, the atoms are pumped into the  $m_J = 0$  sublevel of the ground state.

In a discharge cell experiment, the time constant that determines the magnitude of the light-pressure-induced frequency shifts for two-level atoms is the collisional time  $\tau_c$ . In the presence of degenerate energy levels and optical pumping, the relative magnitudes of the  $A_{\text{SAT}}$  and  $A_{\text{LP}}$  terms in eq. (4.20) depend on polarization. In this case, the line shift of eq. (4.22) does not have a simple linear dependence on  $\tau_c$ . If, for instance, all atoms are pumped into a sublevel that does not interact with either pump or probe, increasing  $\tau_c$  will have no further effect on the line shape. In this case, a more careful investigation of time-dependent dynamics of the pump-probe interaction with the atoms is necessary in order to determine the relative magnitude of the light-pressure effect.

Theoretical discussion in Sec. 4.1 assumed that optical pressure is due entirely to the pump. Any additional term of  $\mathcal{O}(s^1)$  in eq. (4.12) describing velocity redistribution caused by the probe would vanish when integrated over all velocities. Experimentally, this is due to the inherent asymmetry between pump and probe. The detected quantity is probe transmission, and the probe is always resonant with the atoms that on average see a zero change in the atom number as a result of light pressure by the probe itself. That the average light-pressure-induced velocity profile distortion is zero at exactly the resonant velocity is apparent from Fig. 4.1. In the

more concrete discussion of light pressure in helium below, the effect of the probe on atomic velocities is included, but it only adds a minor correction to the results.

### 4.2.3 Measurement of the Collisional Time Constant

When calculating line shapes, linear pressure shifts and broadening predicted by collision theory [47] must be included. For the  $2^3S_1 - 2^3P_J$  transitions in helium, the linear pressure shift is measured to be  $-1.41(2)$  MHz/Torr and the pressure broadening to be  $25.0(2)$  MHz/Torr, in reasonably close agreement with theoretical calculations [57].

The collisional time constant is found from linear pressure broadening of the  $2^3S - 2^3P$  lines. This time constant is  $1/(n\bar{v}\sigma) \propto 1/p$ , for atomic number density  $n$ , pressure  $p$ , collisional cross section  $\sigma$ , and mean relative velocity of the colliding atoms  $\bar{v}$ . Fig. 4.5 shows the half width of the  $2^3S_1 - 2^3P_1$  line as a function of pressure. The collisional time constant is the inverse of line broadening and equals  $6.4(1)/p$   $\mu$ s, where  $p$  is the pressure in mTorr.

### 4.2.4 Line Shape Calculation for a Multilevel Atom

Time evolution of sublevel populations is adequately described by rate equations, taking into account pump and probe absorption and stimulated emission, as well as spontaneous decay. The rate equations for individual Zeeman sublevels are written in terms of velocity- and frequency-dependent unsaturated transition rates

$$R_i(\omega, kv) = \frac{s_i \gamma^3 / 8}{(\omega - \omega_0 \mp kv)^2 + (\gamma/2)^2}. \quad (4.23)$$

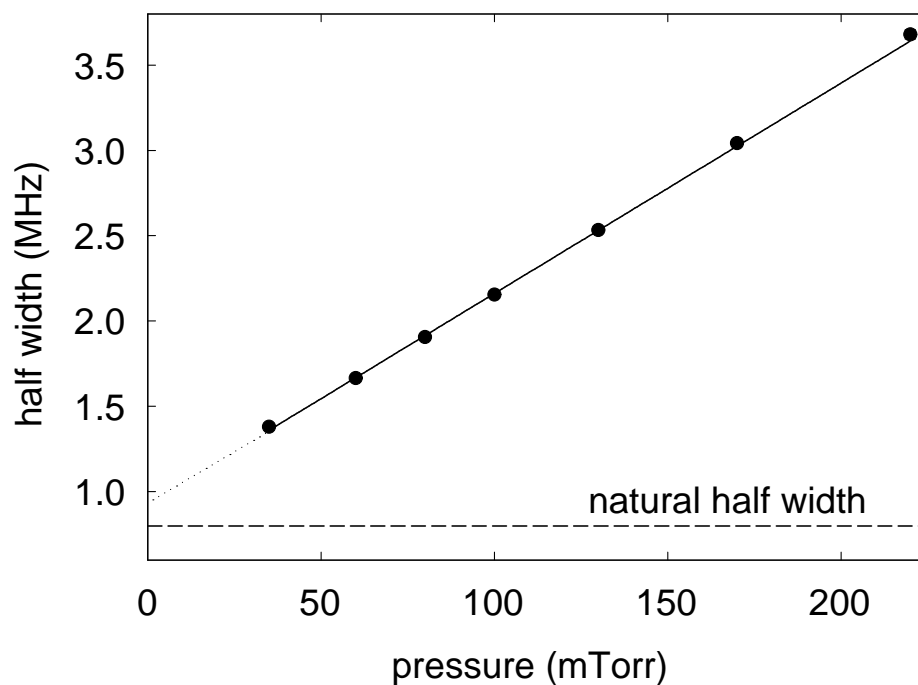


Figure 4.5: Half width of the  $2^3S_1 - 2^3P_1$  line as a function of helium pressure. The line width pressure dependences of the  $2^3S_1 - 2^3P_0$  and  $2^3S_1 - 2^3P_2$  lines agree with that of the  $2^3S_1 - 2^3P_1$  line to about 5%, both from measurements and calculations. The collisional time constant is found from linear pressure broadening. This linearity holds for pressures over about 40 mTorr, when collisional time constants are shorter than optical pumping time constants.

The subscript  $i = 1, 2$  refers to the probe and pump beams, respectively, and  $\gamma = \Gamma + \gamma_c$  is the line width that includes natural width and collisional broadening. The Doppler shift  $kv$  appears with a negative sign for probe and a positive sign for pump because the two beams propagate in opposite directions. The rates  $R_i$  follow from the excitation probability in eq. (4.3), and are incorporated into eq. (4.13) used in the analytical description of the two-level atom dynamics. The transition probability between  $2^3\text{S}(J_g = 1; m_J)$  and  $2^3\text{P}(J_e = 0, 1, 2; n_J)$  is proportional to  $R_i$  and to the coupling coefficient  $C_m^n$  from Fig. 4.4 corresponding to the appropriate  $J_e$ . The time scale of population dynamics is set by the inverse of the natural line width  $\Gamma$ . The transition frequency  $\omega_0$  includes the linear pressure shift.

In order to accurately describe population dynamics of an atom undergoing elastic collisions, it is necessary to include re-equilibration of velocities caused by such collisions. This can be accomplished by adding terms to the rate equations that allow exchange of populations between different velocity groups. These terms can significantly complicate the problem by making rate equations nonlinear. However, a simple approximation of velocity exchanging collisions can be used instead. To simulate collisional velocity equilibration, the terms added to the rate equations of ground state sublevel populations are

$$\dot{g}_m^{\text{coll}} = \gamma_e \left( \frac{1}{2J_g + 1} \sum_{n=-1}^{+1} g_n - g_m \right), \quad (4.24)$$

where  $2J_g + 1 = 3$  is the ground state degeneracy factor. At equilibrium,  $g_m = (g_{-1} + g_0 + g_1)/3$ , and therefore  $\dot{g}_m^{\text{coll}} = 0$ . Eq. (4.24) would be exact if population exchange took place through Zeeman sublevel relaxation rather than through elastic collisions. The factor  $\gamma_e$  is the mean elastic collision rate, proportional to the total

measured collision rate  $\gamma_c$ . It differs slightly between the three optical transitions, since the excited state is not the same for  $2^3S_1 - 2^3P_0$ ,  $2^3S_1 - 2^3P_1$ , and  $2^3S_1 - 2^3P_2$ , and although collisional effects are not explicitly included in the excited state equations (most atoms are in the ground state), they cause the effective  $\gamma_e$  to vary.

Ground and excited state populations of sublevels with total angular momentum projection  $m_J$  are denoted by  $g_m$  and  $e_m$ . The quantities  $e_m$ ,  $g_m$ ,  $R_1$ ,  $R_2$  depend on  $\omega$ ,  $kv$ ,  $s_1$ , and  $s_2$ . The angle of pump polarization with respect to probe polarization is  $\theta$ . The stationary rate equations are

$$\begin{aligned} \dot{g}_m = 0 = & \Gamma \sum_{n=m-1}^{m+1} C_m^n e_n + C_m^m (R_1 + \cos^2 \theta R_2) (e_m - g_m) \\ & + \sum_{n=m\pm 1} \frac{1}{2} C_m^n \sin^2 \theta R_2 (e_n - g_m) + \dot{g}_m^{\text{coll}}, \end{aligned} \quad (4.25)$$

$$\begin{aligned} \dot{e}_{m'} = 0 = & \Gamma e_{m'} + C_{m'}^{m'} (R_1 + \cos^2 \theta R_2) (e_{m'} - g_{m'}) \\ & + \sum_{n=m'\pm 1} \frac{1}{2} C_n^{m'} \sin^2 \theta R_2 (e_{m'} - g_n), \end{aligned} \quad (4.26)$$

where the symmetry  $g_m = g_{-m}$  and  $e_m = e_{-m}$  is exploited.

Once the steady-state velocity-dependent sublevel populations are obtained, they are modified by optical pressure as in eq. (4.8). This modification is proportional to  $\tau$  and to the dispersive functions which are defined as

$$D_i(\omega, kv) = \frac{s_i \epsilon_r (\omega - \omega_0 \mp kv) \gamma^3 / 2}{[(\omega - \omega_0 \mp kv)^2 + (\gamma/2)^2]^2} \quad (4.27)$$

for the probe and pump beams.

The probe absorption coefficient is

$$A_1(\omega, p, s_1, s_2) = a_0 \int \Delta N(\omega, kv, p) \sigma_1(\omega, kv) dv, \quad (4.28)$$

where  $a_0$  is an overall pressure-dependent multiplicative factor,  $\Delta N$  is the population difference between the ground and excited sublevels coupled by the probe, pressure  $p$  appears because of its effect on  $\tau_c$ , and the cross section of the probe beam's interaction with the atoms is

$$\sigma_1(\omega, kv) = \sigma_0 \frac{(\gamma/2)^2}{(\omega - \omega_0 - kv)^2 + (\gamma/2)^2}. \quad (4.29)$$

Finally, the Doppler-free transmission signal observed in the experiment is

$$S(\omega, p) = A_1(\omega, p, s_1, 0) - A_1(\omega, p, s_1, s_2), \quad (4.30)$$

since synchronous detection subtracts the signal obtained with the pump beam turned off.

If the functions  $D_i(\omega, kv)$  are neglected, this description and specifically eq. (4.30) give ordinary Lorentzian saturation signal shapes. The effect of optical pressure is entirely included in  $D_i$ , which are used to modify the ground-excited state population difference  $\Delta N$ . The resulting  $\Delta N$  is inserted into eq. (4.28), and the saturation signal is computed from eq. (4.30). The signal profile  $S(\omega, p)$  then includes the effect of light pressure as well as the ordinary saturation contribution.

### 4.2.5 The Two-Level Atom

As a check, the two-level result of Sec. 4.1 is recovered. The two-level atom interacts with  $\hat{z}$ -polarized pump and probe. Its ground and excited state populations are  $g(\omega, kv)$  and  $e(\omega, kv)$ , respectively. The steady-state rate equations describing its

population dynamics, according to eqs. (4.25), (4.26), are

$$\begin{aligned} \dot{g}(\omega, kv) = 0 = R_1(\omega, kv)[e(\omega, kv) - g(\omega, kv)] \\ + R_2(\omega, kv)[e(\omega, kv) - g(\omega, kv)] + \Gamma e(\omega, kv), \end{aligned} \quad (4.31)$$

$$\begin{aligned} \dot{e}(\omega, kv) = 0 = R_1(\omega, kv)[g(\omega, kv) - e(\omega, kv)] \\ + R_2(\omega, kv)[g(\omega, kv) - e(\omega, kv)] - \Gamma e(\omega, kv), \end{aligned} \quad (4.32)$$

$$g(\omega, kv) + e(\omega, kv) = 1. \quad (4.33)$$

The population difference which determines  $A_1$  of eq. (4.28) is

$$\Delta N(\omega, kv, s_2) = [g(\omega, kv, s_2) - e(\omega, kv, s_2)] \cdot [1 - \tau_c D_1(\omega, kv) - \tau_c D_2(\omega, kv, s_2)], \quad (4.34)$$

where  $s_2 = 0$  if the pump is turned off.

Using eqs. (4.28) and (4.30), it is straightforward to compute line shapes of the expected probe transmission signals and to find their frequency shifts. The results are shown in Fig. 4.6, where the linear pressure broadening and shift values measured in the helium experiment are used. At higher pressures, only the linear pressure shift is apparent. At lower densities, however, there is a shift inversely proportional to pressure. In fact, if  $\tau_c = 1/\gamma_c$ , where  $\gamma_c = 0.0138 \Gamma p / \text{mTorr}$  from line broadening measurements, the shift of  $\omega_0$  is exactly  $\delta\omega = \epsilon_r \tau_c \Gamma / 2$ , as predicted by the analytical description of Sec. 4.1 and eq. (4.22). The numerical approach of directly solving the rate equations and the analytical approach of calculating the probe absorption coefficient as in eq. (4.16) are equivalent, and the numerical approach is used below to predict line center shifts for real helium transitions.

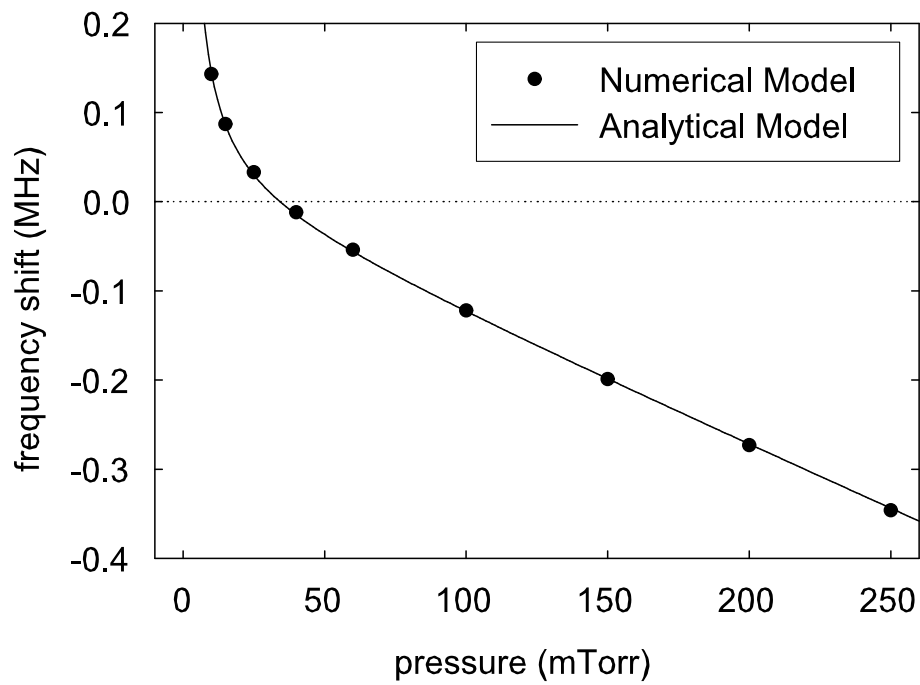


Figure 4.6: The computed frequency shifts of a two-level atom due to optical pressure. The analytical and numerical calculations of the probe transmission signal give equivalent results.

### 4.2.6 The $2^3S_1 - 2^3P_0$ Transition

The rate equations describing  $2^3S_1 - 2^3P_0$  are

$$\dot{g}_1 = 0 = \frac{1}{3} \sin^2 \theta \frac{R_2}{2} (e_0 - g_1) + \frac{1}{3} \Gamma e_0 + \gamma_e \left( \frac{1}{3} \sum_n g_n - g_1 \right), \quad (4.35)$$

$$\dot{g}_0 = 0 = \frac{1}{3} R_1 (e_0 - g_0) + \frac{1}{3} \cos^2 \theta R_2 (e_0 - g_0) + \frac{1}{3} \Gamma e_0 + \gamma_e \left( \frac{1}{3} \sum_n g_n - g_0 \right), \quad (4.36)$$

$$\dot{e}_0 = 0 = \frac{1}{3} R_1 (g_0 - e_0) + \frac{1}{3} \cos^2 \theta R_2 (g_0 - e_0) + \frac{1}{3} \sin^2 \theta R_2 (g_1 - e_0) - \Gamma e_0, \quad (4.37)$$

$$2g_1 + g_0 + e_0 = 1, \quad (4.38)$$

assuming that  $g_m, e_m, R_1, R_2$  depend on  $\omega, kv, s_1,$  and  $s_2$ . The transition rates are weighted by the coupling coefficients shown in Fig. 4.4.

Population difference that enters the absorption coefficient (4.28) is found analogously to eq. (4.34),

$$\Delta N = g_0 \left( 1 - \frac{1}{3} \tau_c D_1 - \frac{1}{3} \tau_c \cos^2 \theta D_2 \right) - e_0 \left( 1 - \frac{1}{3} \tau_c D_1 - \frac{1}{3} \tau_c D_2 \right). \quad (4.39)$$

### 4.2.7 The $2^3S_1 - 2^3P_1$ Transition

The rate equations for  $2^3S_1 - 2^3P_1$  are

$$\begin{aligned} \dot{g}_1 = 0 = & \frac{1}{2} R_1 (e_1 - g_1) + \frac{1}{2} \cos^2 \theta R_2 (e_1 - g_1) + \frac{1}{2} \sin^2 \theta \frac{R_2}{2} (e_0 - g_1) \\ & + \frac{1}{2} \Gamma e_1 + \frac{1}{2} \Gamma e_0 + \gamma_e \left( \frac{1}{3} \sum_n g_n - g_1 \right), \end{aligned} \quad (4.40)$$

$$\dot{g}_0 = 0 = \frac{1}{2} \sin^2 \theta R_2 (e_1 - g_0) + \Gamma e_1 + \gamma_e \left( \frac{1}{3} \sum_n g_n - g_0 \right), \quad (4.41)$$

$$\begin{aligned} \dot{e}_1 = 0 = & \frac{1}{2} R_1 (g_1 - e_1) + \frac{1}{2} \cos^2 \theta R_2 (g_1 - e_1) + \frac{1}{2} \sin^2 \theta \frac{R_2}{2} (g_0 - e_1) \\ & - \Gamma e_1, \end{aligned} \quad (4.42)$$

$$\dot{e}_0 = 0 = \frac{1}{2} \sin^2 \theta R_2 (g_1 - e_0) - \Gamma e_0, \quad (4.43)$$

$$2g_1 + g_0 + 2e_1 + e_0 = 1. \quad (4.44)$$

The population difference needed to find the absorption coefficient (4.28) is

$$\Delta N = 2(g_1 - e_1) \left(1 - \frac{1}{2} \tau_c D_1 - \frac{1}{2} \tau_c \cos^2 \theta D_2 - \frac{1}{4} \tau_c \sin^2 \theta D_2\right). \quad (4.45)$$

### 4.2.8 The $2^3S_1 - 2^3P_2$ Transition

The equations for  $2^3S_1 - 2^3P_2$  are

$$\begin{aligned} \dot{g}_1 = 0 = & \frac{1}{2} R_1 (e_1 - g_1) + \frac{1}{2} \cos^2 \theta R_2 (e_1 - g_1) + \sin^2 \theta \frac{R_2}{2} (e_2 - g_1) \\ & + \frac{1}{6} \sin^2 \theta \frac{R_2}{2} (e_0 - g_1) + \Gamma e_2 + \frac{1}{2} \Gamma e_1 + \frac{1}{6} \Gamma e_0 + \gamma_e \left(\frac{1}{3} \sum_n g_n - g_1\right), \end{aligned} \quad (4.46)$$

$$\begin{aligned} \dot{g}_0 = 0 = & \frac{2}{3} R_1 (e_0 - g_0) + \frac{2}{3} \cos^2 \theta R_2 (e_0 - g_0) + \frac{1}{2} \sin^2 \theta R_2 (e_1 - g_0) \\ & + \Gamma e_1 + \frac{2}{3} \Gamma e_0 + \gamma_e \left(\frac{1}{3} \sum_n g_n - g_0\right), \end{aligned} \quad (4.47)$$

$$\dot{e}_2 = 0 = \sin^2 \theta \frac{R_2}{2} (g_1 - e_2) - \Gamma e_2, \quad (4.48)$$

$$\begin{aligned} \dot{e}_1 = 0 = & \frac{1}{2} R_1 (g_1 - e_1) + \frac{1}{2} \cos^2 \theta R_2 (g_1 - e_1) + \frac{1}{2} \sin^2 \theta \frac{R_2}{2} (g_0 - e_1) \\ & - \Gamma e_1, \end{aligned} \quad (4.49)$$

$$\begin{aligned} \dot{e}_0 = 0 = & \frac{2}{3} R_1 (g_0 - e_0) + \frac{2}{3} \cos^2 \theta R_2 (g_0 - e_0) + \frac{1}{6} \sin^2 \theta R_2 (g_1 - e_0) \\ & - \Gamma e_0, \end{aligned} \quad (4.50)$$

$$2g_1 + g_0 + 2e_2 + 2e_1 + e_0 = 1. \quad (4.51)$$

The total population difference is

$$\begin{aligned}
\Delta N = & 2g_1\left(1 - \frac{1}{2}\tau_c D_1 - \frac{1}{2}\tau_c \cos^2 \theta D_2 - \frac{7}{12}\tau_c \sin^2 \theta D_2\right) \\
& + g_0\left(1 - \frac{2}{3}\tau_c D_1 - \frac{2}{3}\tau_c \cos^2 \theta D_2 - \frac{1}{2}\tau_c \sin^2 \theta D_2\right) \\
& - 2e_1\left(1 - \frac{1}{2}\tau_c D_1 - \frac{1}{2}\tau_c \cos^2 \theta D_2 - \frac{1}{4}\tau_c \sin^2 \theta D_2\right) \\
& - e_0\left(1 - \frac{2}{3}\tau_c D_1 - \frac{2}{3}\tau_c \cos^2 \theta D_2 - \frac{1}{6}\tau_c \sin^2 \theta D_2\right).
\end{aligned} \tag{4.52}$$

### 4.3 Results and Comparison with Experiment

The solutions to equations in Secs. 4.2.6 - 4.2.8 describing sublevel population dynamics of the helium atom in the presence of light pressure are compared to the experimental results at orthogonal and parallel polarizations of the pump and probe beams. The light-pressure-induced shifts in the orthogonal polarization configuration exhibit a striking discontinuity as a function of helium pressure in the discharge cell. At the singular pressure value, the collisional time constant equals the optical pumping time constant,  $\tau_c \sim \tau_{op} \sim 2/\Gamma$ . The competition between the two time constants forces a sign change of the saturation signal, but not of the light-pressure-induced component of the line shape, leading to large and discontinuous line shifts.

#### 4.3.1 Discontinuous Frequency Shifts Obtained with Orthogonal Pump and Probe Polarizations

Including optical pressure in the line shape calculation yields excellent agreement with experiment, and confirms the hypothesis that velocity profile deformation by the light scattering force is the cause for strong nonlinear line center dependences on

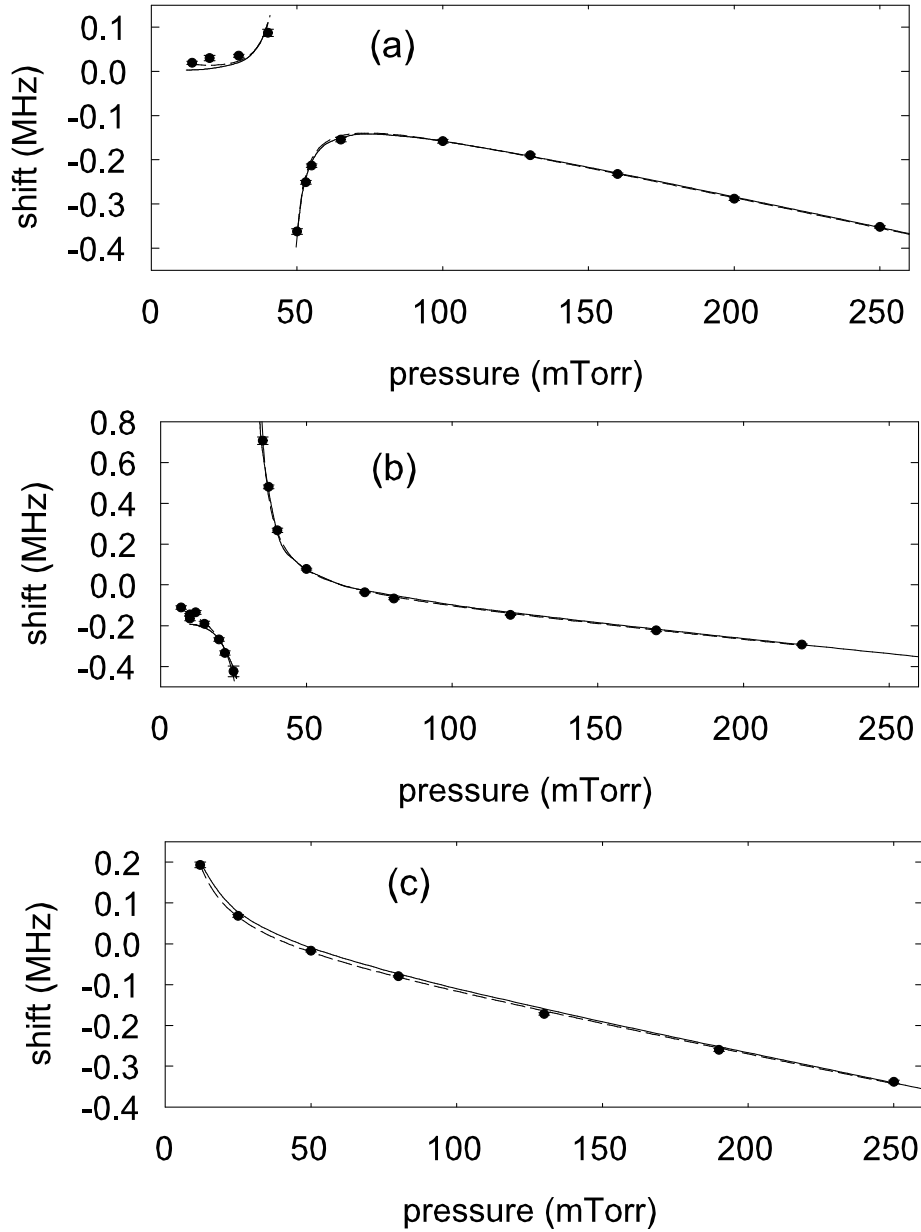


Figure 4.7: Frequency shifts due to optical pressure for (a)  $2^3S_1 - 2^3P_0$ , (b)  $2^3S_1 - 2^3P_1$ , and (c)  $2^3S_1 - 2^3P_2$ , and lin $\perp$ lin polarization configuration. The circles denote experimental values and include statistical error bars, the solid curves are calculated shifts, and the dashed curves are  $1/(p - p_0)$  fits to the data as explained in the text.

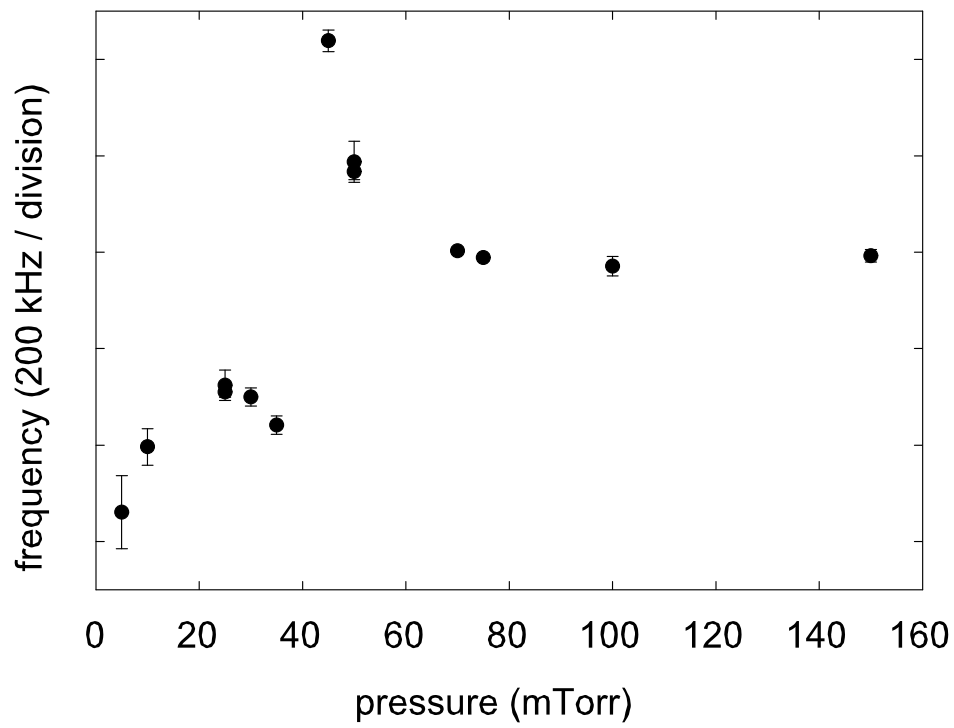


Figure 4.8: The  $f_{12}$  fine structure interval measured with the lin\_lin polarization configuration.

pressure. Fig. 4.7 shows data (circles) and predictions (solid curves) for all three optical transitions and the lin $\perp$ lin pump and probe polarization configuration ( $\theta = 90^\circ$ ). At higher pressures, the most prominent feature is the linear pressure shift. At lower densities, velocity-equilibrating collisions become rare, and the light-pressure effect is the dominant feature. All three curves exhibit significant qualitative differences, and, in addition, the  $2^3S_1 - 2^3P_0$  and  $2^3S_1 - 2^3P_1$  curves show highly discontinuous behavior as a function of helium pressure  $p$ . Fig. 4.8 shows the value of the  $f_{12}$  fine structure interval vs. pressure measured at  $\theta = 90^\circ$ .

Although the curves in Fig. 4.7 emerge from a combination of equations that describe population dynamics and velocity profile deformation by light pressure, they are not difficult to understand on an intuitive basis. The  $2^3S_1 - 2^3P_2$  transition in Fig. 4.7 (c) happens to be the simplest. In this case, all ground state sublevels interact with the probe as shown in Fig. 4.4, and the situation is quite similar to the two-level case illustrated in Fig. 4.6. The shift is  $\epsilon_r\tau$  as in eq. (4.22), and  $\tau = \tau_c \propto 1/p$ .

The  $2^3S_1 - 2^3P_1$  transition in Fig. 4.7 (b) is more complicated, and the line center has an effective singularity at  $p_0 = 32$  mTorr. Fig. 4.4 shows that the coupling coefficient between the  $m_J = 0$  sublevels vanishes in this case. Therefore, if the probe is  $\hat{z}$ -polarized, the  $m_J = 0$  ground sublevel is a dark state into which the atom's population is optically pumped. If the pump is then introduced such that the polarization arrangement is lin $\perp$ lin, the pump can restore some of the population to the  $m_J = \pm 1$  sublevels. Optical pumping is only significant at lower pressures, when the optical time constant  $1/\Gamma$  is close to the collisional time constant  $1/\gamma_c$ . If the pressure is low enough, probe transmission changes from *increased* to *decreased*

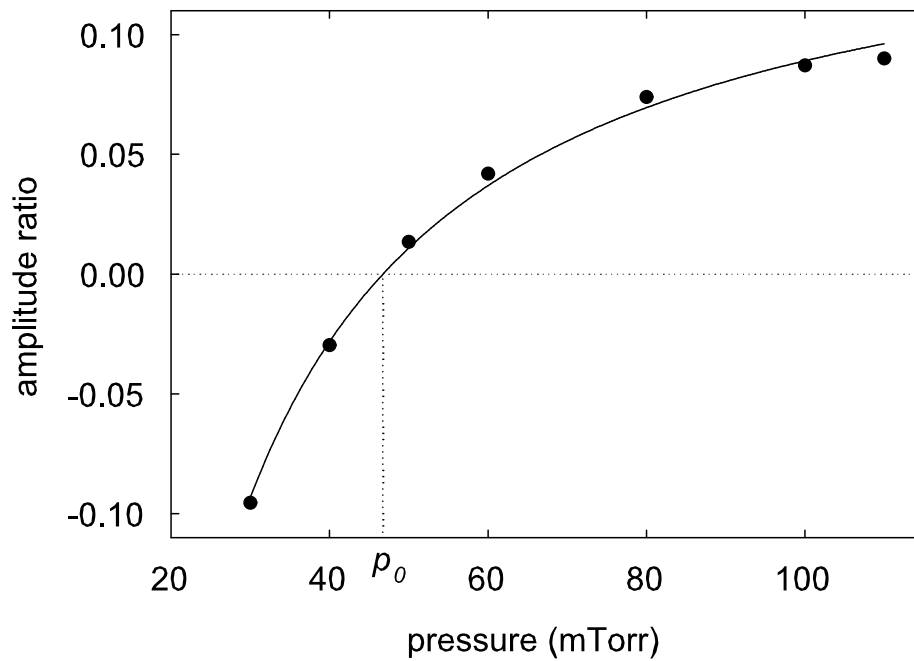


Figure 4.9: Calculated ratios of the  $2^3S_1 - 2^3P_0$  signal amplitudes in the lin $\perp$ lin configuration to the signal amplitudes of a two-level atom. The pressure dependence is nearly proportional to  $1 - p_0/p$  (fitted curve).

in the presence of the pump. In other words, at a special value of pressure,  $p_0$ , the saturation signal amplitude vanishes, and becomes negative at lower pressures. Since the effect of the scattering force is always of the same sign, the resulting line shift changes sign at  $p_0$ . This situation is equivalent to flipping the sign of the symmetric component of the signal shown by the dashed line in Fig. 4.2, while keeping the sign of the dispersive component (dotted line) unchanged. The result is a red shift of the line instead of a blue shift.

In the case of  $2^3S_1 - 2^3P_1$ , line shift can still be described by the function of eq. (4.22), if  $\tau$  is proportional to  $1/(p - p_0)$  rather than  $1/p$ . This is seen from referring to eq. (4.21) of the two-level theoretical description. If the first term of  $X(\delta)$  is multiplied by  $1 - p_0/p$ , then the frequency shift of the Lorentzian in eq. (4.22) is proportional to  $1/(p - p_0)$ , as long as the shift does not exceed the half width of the line (otherwise, the signal to noise ratio becomes small and the shift so large that perturbative approximations do not hold). When  $J_e \leq J_g$ , the saturation signal amplitude in the  $\text{lin}\perp\text{lin}$  configuration is indeed proportional to  $1 - p_0/p$ . Fig. 4.9 shows the calculated dependence of  $2^3S_1 - 2^3P_0$  signal amplitude on pressure, fitted to  $1 - p_0/p$ . The  $2^3S_1 - 2^3P_0$  and  $2^3S_1 - 2^3P_1$  signal amplitude dependences on  $p$  are similar, except the zero crossings occur at slightly different pressures. The discontinuity point  $p_0$  can be estimated as the pressure at which  $\gamma_c \sim \Gamma/2$ . In other words, at  $p_0$  the collisional time constant becomes approximately equal to one cycle of optical pumping, which leads to the change from probe transmission to probe absorption and to discontinuous behavior of light-pressure-induced line shifts.

The  $2^3S_1 - 2^3P_0$  transition also has dark states which are  $m_J = \pm 1$  for a  $\hat{z}$ -

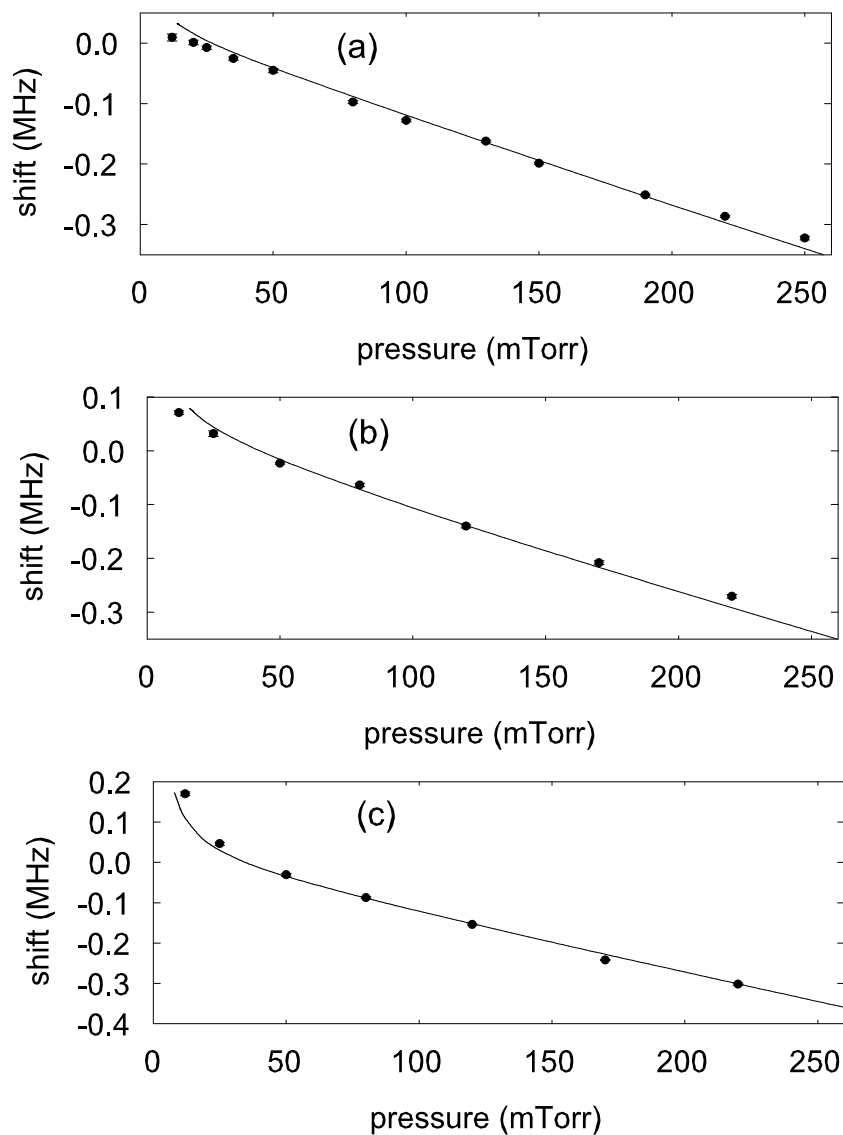


Figure 4.10: Frequency shifts due to optical pressure for (a)  $2^3S_1 - 2^3P_0$ , (b)  $2^3S_1 - 2^3P_1$ , and (c)  $2^3S_1 - 2^3P_2$ , and lin||lin polarization configuration. The circles denote experimental values and include statistical error bars, and the solid curves are calculated shifts.

polarized probe, and its line center in Fig. 4.7 (a) shows a singularity at 47 mTorr. The overall sign of the light-pressure-induced shift here is reversed, because in the lin $\perp$ lin configuration, the probe interacts with the  $m_J = 0$  sublevels, but the pump beam cannot exert pressure on the  $m = 0$  ground state sublevel. Therefore the probe beam picks up only the deformation of the excited state velocity distribution, whereas in the  $2^3S_1 - 2^3P_1$  and  $2^3S_1 - 2^3P_2$  cases the deformation of the ground state distributions plays a dominant role.

In addition to theoretical predictions, Fig. 4.7 shows fits to the data (dashed lines). The fitting function is

$$f(p) = \frac{a}{p - p_0} - 0.00141 p, \quad (4.53)$$

where  $p_0 = 0$  for  $P_2$ , the coefficient of the second term is the previously measured linear pressure shift,  $p$  is in mTorr,  $f$  is in MHz, and  $a \propto \epsilon_r \tau$ .

### 4.3.2 Collisional Parameters Obtained from Discontinuous Frequency Shifts

The theory of light pressure in a gas cell is based on essentially two parameters,  $\gamma_e$  and  $\tau_c$ . Velocity-equilibrating collision rate  $\gamma_e$  differs by approximately 20% for  $2^3S_1 - 2^3P_0$ ,  $2^3S_1 - 2^3P_1$ , and  $2^3S_1 - 2^3P_2$ , since it is a phenomenological constant and is affected by differences in the level structure. The rate  $\gamma_e$  is uniquely determined by discontinuity points in Figs. 4.7 (a) and (b), and equals  $0.39 \gamma_c$  and  $0.52 \gamma_c$  for  $2^3S_1 - 2^3P_0$  and  $2^3S_1 - 2^3P_1$ , respectively. The  $2^3S_1 - 2^3P_2$  transition is relatively insensitive to the exact value of  $\gamma_e$ , which was chosen to be  $0.5 \gamma_c$  for computational

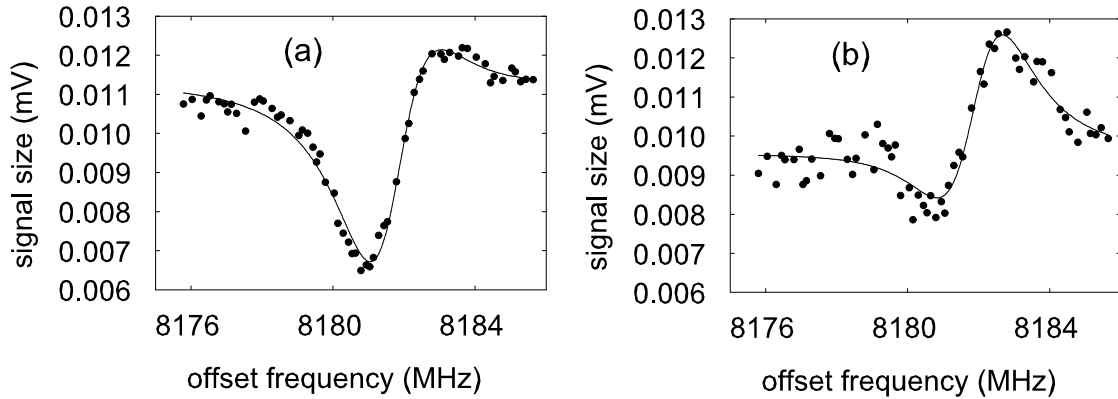


Figure 4.11: Direct manifestation of optical pressure creating a dispersive kink in the helium velocity distribution. The data are taken for  $2^3S_1 - 2^3P_1$  in the lin $\perp$ lin configuration at (a) 30 mTorr and (b) 32 mTorr pressures. The dashed curves are line shapes predicted by the theory of light pressure.

purposes. The second parameter,  $\tau_c$ , is also transition-dependent, since collisions interrupt the coherent action of the pump slightly differently as the pump couples different sublevels in all three transitions. From the lin $\perp$ lin data,  $\tau_c$  was found to be  $1.8/\gamma_c$ ,  $2.5/\gamma_c$ , and  $1.2/\gamma_c$  for  $2^3S_1 - 2^3P_0$ ,  $2^3S_1 - 2^3P_1$ , and  $2^3S_1 - 2^3P_2$ , respectively.

The constants  $\gamma_e$  and  $\tau_c$  are expected to also have a mild dependence on  $\theta$ . However, they were kept unchanged when the theory was used to predict light-pressure-induced shifts for the lin $\parallel$ lin polarization configuration ( $\theta = 0^\circ$ ). The qualitative agreement is very good and is shown in Fig. 4.10. In this arrangement,  $2^3S_1 - 2^3P_2$  is affected the most, since it is a closed system and resembles a two-level system in both lin $\perp$ lin and lin $\parallel$ lin cases.  $2^3S_1 - 2^3P_1$ , and especially  $2^3S_1 - 2^3P_0$ , are affected less, since they are open systems in this case, optical pumping severely limits  $\tau$ , and light-pressure-induced shifts do not become large.

### 4.3.3 Direct Observation of Light Pressure Near Discontinuity Points

In the discontinuous  $\text{lin} \perp \text{lin } 2^3\text{S}_1 - 2^3\text{P}_0$  and  $2^3\text{S}_1 - 2^3\text{P}_1$  data sets, signal quality near  $p_0$  is poor since the Lorentzian signal amplitude vanishes at that point, according to Fig. 4.9. Therefore, a line center value cannot be obtained for  $p_0$  and the nearby pressure values. When the Lorentzian component of eq. (4.21) vanishes, however, the dispersive component can still be observed. When line shapes of the  $2^3\text{S}_1 - 2^3\text{P}_1$  transition are collected near  $p_0 = 31.5$  mTorr, the effect of light pressure is seen directly, as illustrated in Fig. 4.11. The first line shape is taken for  $p < p_0$  and demonstrates a significant red shift, while the second line shape corresponds to  $p > p_0$  and shows an equivalently large blue shift. The distance between the peaks is almost 2 MHz, or a full line width.

## 4.4 Light-Pressure Effect at Magnetic Resonance

A qualitative confirmation of the light-pressure effect is obtained by resolving the  $2^3\text{S}$  Zeeman sublevels with a  $\hat{z}$ -directed magnetic field, and choosing the field strength such that the 60 MHz rf discharge satisfies the magnetic resonance condition with the field. (Chapter 6 describes effects of magnetic resonance in greater detail.) At this field of approximately 21.7 G, the ground state sublevels are split by several line widths, and the  $2^3\text{S}_1 (m_J = 0) - 2^3\text{P}_0 (m'_J = 0)$  transition can be selectively driven with vertically polarized pump and probe.

Away from magnetic resonance, optical pumping into the  $2^3\text{S}_1 (m_J = \pm 1)$  sub-

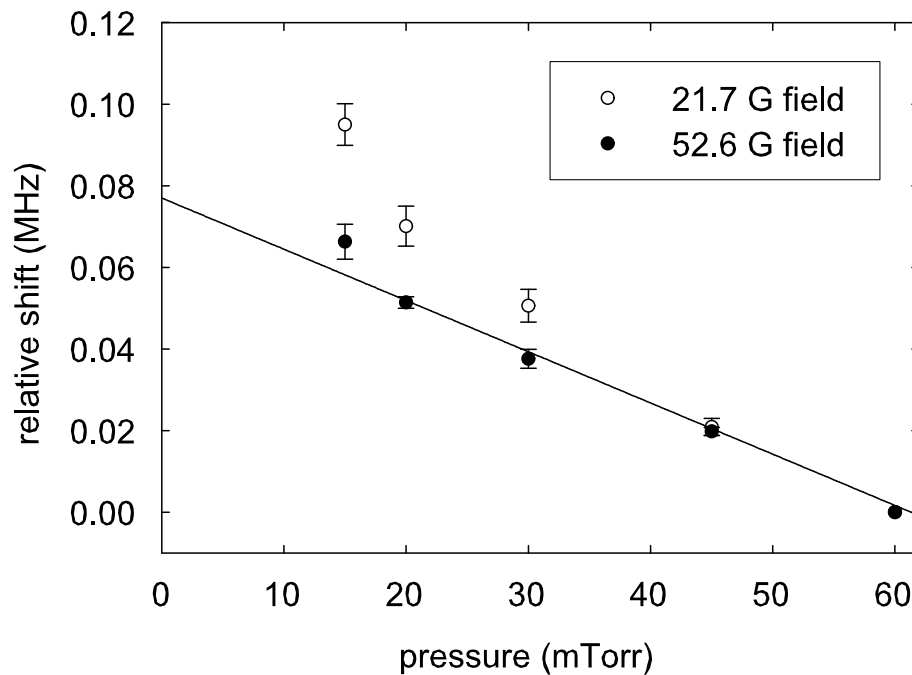


Figure 4.12: Light-pressure-induced shifts at magnetic resonance. Filled circles show the  $2^3S_1(m_J = 0) - 2^3P_0(m'_J = 0)$  transition frequencies in the presence of a 52.6 G magnetic field. This field value is far from magnetic resonance. A straight line reflecting linear pressure shifts is drawn through the points. Open circles show the same transition frequencies in the presence of a 21.7 G field that satisfies the  $2^3S$  magnetic resonance condition with the 60 MHz rf discharge. Light-pressure-induced shifts are strongly enhanced, since atoms undergo repeated interactions with pump photons.

levels strongly suppresses light-pressure-induced frequency shifts, as in Fig. 4.10 (a). At magnetic resonance, the populations of all  $2^3S_1$  sublevels are mixed with the rf field, and atoms undergo multiple interaction with pump photons, which leads to larger light-pressure-induced shifts. Fig. 4.12 confirms the enhancement of frequency shifts at magnetic resonance.

## 4.5 Controlling Light-Pressure-Induced Line Shifts

Understanding the origins of light-pressure-induced line shifts helps minimize their effect on the fine structure measurements. There are two ways to reduce the impact of optical pressure.

From Figs. 4.7 and 4.10 it is evident that  $2^3S_1 - 2^3P_2$  is much less sensitive to  $\theta$  than  $2^3S_1 - 2^3P_0$  and  $2^3S_1 - 2^3P_1$ . At  $\theta \simeq 30^\circ$ , the pressure curve for  $2^3S_1 - 2^3P_1$  looks qualitatively similar to the  $2^3S_1 - 2^3P_2$  curve. The  $f_{12}$  fine structure interval is plotted vs. pressure for  $\theta = 30^\circ$  in Fig. 4.13, and at this angle the dependence of the interval on pressure is significantly suppressed.

This method of choosing the optimal  $\theta$  is generally not adequate for a high precision fine structure measurement, since residual light-pressure-induced shifts remain at low pressures due to intrinsic differences between sublevel structure of the two optical transitions which leads to different degrees of velocity profile distortion. However, the  $f_{12}$  interval can be measured in a way that allows light-pressure-induced shifts to cancel entirely. Such a measurement is achieved by resolving Zeeman sublevels with a  $\hat{z}$ -directed magnetic field and measuring optical transition frequencies only between sublevels with those  $m_J$  values that have the same coupling strengths for both  $2^3S_1$

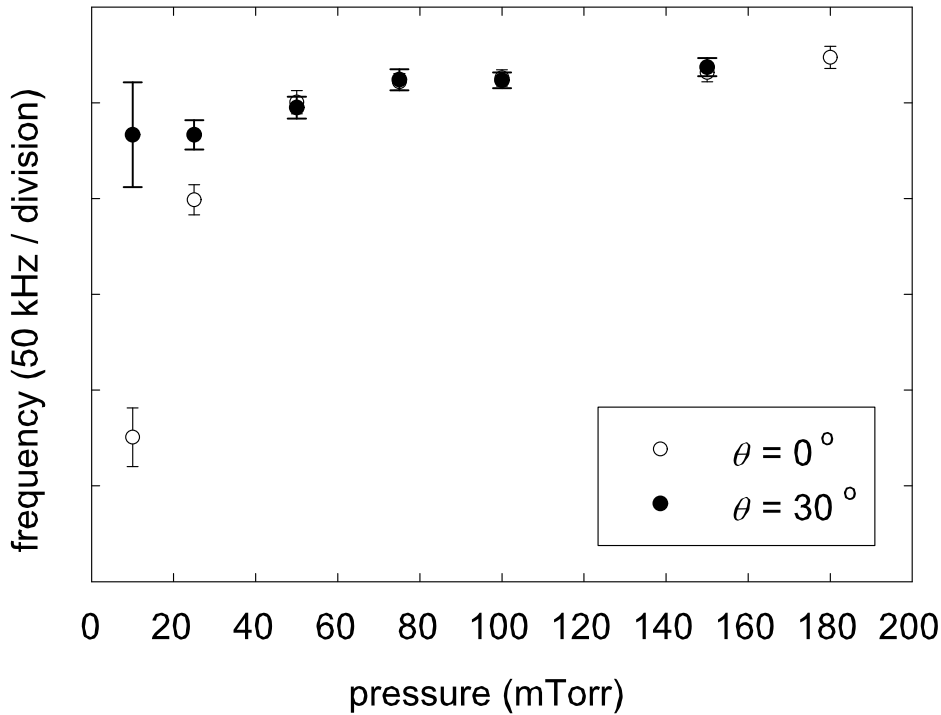
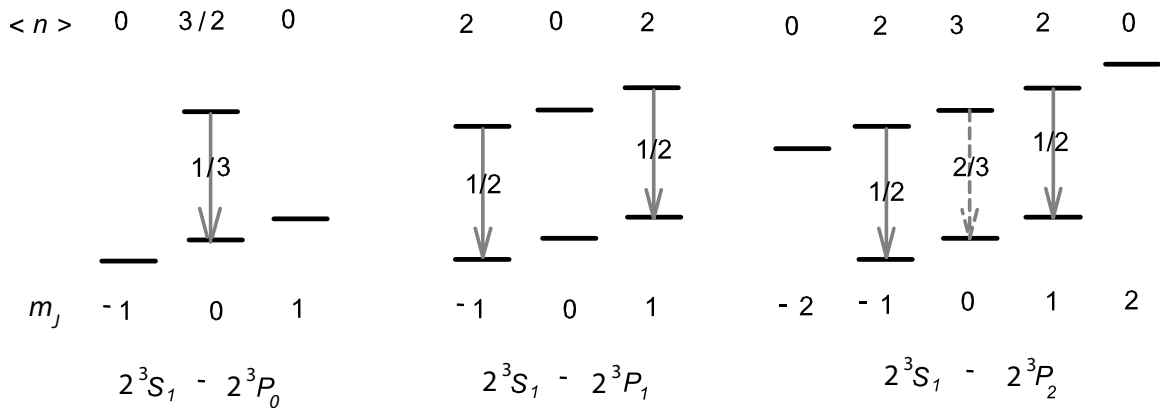

 Figure 4.13: The  $f_{12}$  fine structure interval at  $\theta = 0^\circ$  and  $\theta = 30^\circ$ .


Figure 4.14: Magnetically resolved  $f_{12}$  measurement unaffected by light-pressure shifts. Shifts cancel for  $(m_J = \pm 1) - (m'_J = \pm 1)$ . If instead  $(m_J = 0) - (m'_J = 0)$  is used for  $2^3S_1 - 2^3P_2$ , shifts do not cancel because mean numbers of scattered photons,  $\langle n \rangle$ , are not the same. The difference between these two  $f_{12}$  measurements can serve as a calibration for  $f_{01}$  and  $f_{02}$  light-pressure-induced shifts.

–  $2^3P_1$  and  $2^3S_1 - 2^3P_2$ . The scattering force then affects velocity distributions in equivalent ways, and the difference  $f_{12}$  is free of shifts. The unique choice of optical transitions follows from a consideration of coupling coefficients (Fig. 4.4):  $m_J = \pm 1$  sublevels must be coupled with  $\hat{z}$ -polarized pump and probe, as shown in Fig. 4.14.

The  $f_{01}$  and  $f_{02}$  intervals do not allow such cancellation of light-pressure-induced shifts. However, if  $f_{12}$  is measured using the  $(m_J = 0) - (m'_J = 0)$  transition for  $2^3S_1 - 2^3P_2$  (Fig. 4.14), along with the  $(m_J = \pm 1) - (m'_J = \pm 1)$  result it can be used as a calibration of shifts for  $f_{01}$  and  $f_{02}$ . Aside from the linear pressure shift, there would be a residual light-pressure-induced shift, since the mean numbers of scattered photons,  $\langle n \rangle$ , differ for  $2^3S_1 - 2^3P_1$  and  $2^3S_1 - 2^3P_2$  in this case. The difference between the two  $f_{12}$  pressure dependences can be scaled by the difference in  $\langle n \rangle$  to obtain the light-pressure-induced shift corrections for  $f_{01}$  and  $f_{02}$ . Sec. 6.4 describes the light-pressure corrections applied to the fine structure interval data.

# Chapter 5

## Zeeman Effect in Helium

Light-pressure-induced shifts discussed in Chapter 4 are suppressed if atoms are optically pumped out of resonance before they accumulate significant recoil velocity from absorbing multiple pump photons. This optical pumping occurs naturally if the laser is linearly polarized and the magnetic sublevels are split with a magnetic field parallel to the light polarization axis.

Although the magnetic field shifts measured frequencies, these shifts can be corrected much more accurately than light-pressure shifts. A constant magnetic field is applied to the helium cell, and corrections are made to the measured interval values. These corrections are based on extensive experimental and theoretical work [32, 58] with helium in a magnetic field.

## 5.1 Theoretical Description of the Zeeman Effect

### 5.1.1 Frequency Shifts

An external magnetic field  $B$  mixes states with different total angular momenta  $J$  and  $J'$ . The angular momentum projection onto the field axis,  $m_J$ , is a good quantum number. The magnetic field coupling of  $2^3\text{P}$  energy levels with equal  $m_J$  values results in a quadratic level shift in addition to the linear Zeeman splitting of magnetic sublevels. The atomic Hamiltonian in the presence of the external field consists of the unperturbed and Zeeman components,

$$\mathcal{H} = H_0 + H_{\text{Zeeman}}. \quad (5.1)$$

The unperturbed Hamiltonian  $H_0$  leads to the energies  $\epsilon_J$  for the  $2^3\text{P}_J$  states.

The Zeeman Hamiltonian  $H_{\text{Zeeman}}$  is taken only to first order in  $B$ , as second order terms are proportional to  $(\mu_B B)^2/R_\infty$ , where  $R_\infty$  is the Rydberg constant, and are too small to be considered here. It is written as [59]

$$H_{\text{Zeeman}} = g_L \mu_B \vec{L} \cdot \vec{B} + g_S \mu_B \vec{S} \cdot \vec{B} + \vec{\mu}_{\text{rel}} \cdot \vec{B}. \quad (5.2)$$

The relativistic correction to the magnetic moment  $\vec{\mu}_{\text{rel}}$  effectively results in small corrections to  $g_L$  and  $g_S$ , as well as an additional small  $g$ -factor,  $g_x$ . The spin  $g$ -factor for a free electron is [6, 5]

$$g_S = 2.002\,319, \quad (5.3)$$

and the orbital magnetic moment is [58]

$$g_L = 0.999\,863. \quad (5.4)$$

The corrected  $g$ -factors used to compute Zeeman corrections for the  $2^3\text{P}$  state of helium are based on recently calculated values that are in close agreement with experimental measurements [58],

$$g'_S = 2.002\,239, \quad (5.5)$$

$$g'_L = 0.999\,874, \quad \text{and} \quad (5.6)$$

$$g_x = -0.000\,005. \quad (5.7)$$

The  $g$ -factor for the helium  $2^3\text{S}$  state has also been calculated to a very high accuracy [60, 58],

$$g_S^{2\text{S}} = 2.002\,237. \quad (5.8)$$

The magnetic field shifts the metastable  $2^3\text{S}_1(m_J)$  states by  $\mu_B B m_J g_S^{2\text{S}}$ . The splitting in this case has no quadratic component since the  $2^3\text{S}$  state lies far from all other energy levels and mixing is avoided. The Bohr magneton is [5]

$$\mu_B = \frac{e\hbar}{2m_e} = 1.399\,625 \text{ MHz/G}. \quad (5.9)$$

Below, the total Hamiltonian  $\mathcal{H}$  for the  $2^3\text{P}_J$  states of helium is written in matrix representation, where the matrix elements are of the form  $\langle J', m_J | H_0 + H_{\text{Zeeman}} | J, m_J \rangle$ .

When  $m_J = \pm 2$ , the matrix consists of a single term, since only  $J = 2$  contributes and there is no mixing of different angular momenta.

$$\frac{\langle 2, m_J = \pm 2 | \epsilon_2 + \frac{1}{2}\mu_B B m_J (g'_L + g'_S + \frac{1}{15}g_x) | 2, m_J = \pm 2 \rangle}{\epsilon_2 + \frac{1}{2}\mu_B B m_J (g'_L + g'_S + \frac{1}{15}g_x)} \quad (5.10)$$

Mixing of  $J = 2, 1$  with  $m_J = \pm 1$  results in a  $2 \times 2$  matrix.

$ 1, m_J = \pm 1\rangle$	$ 2, m_J = \pm 1\rangle$	
$\epsilon_1 + \frac{1}{2}\mu_B B m_J (g'_L + g'_S - \frac{1}{3}g_x)$	$\frac{1}{2}\mu_B B (g'_L - g'_S + \frac{2}{15}g_x)$	(5.11)
$\frac{1}{2}\mu_B B (g'_L - g'_S + \frac{2}{15}g_x)$	$\epsilon_2 + \frac{1}{2}\mu_B B m_J (g'_L + g'_S + \frac{1}{15}g_x)$	

Finally, the external field mixes  $J = 2, 1, 0$  with  $m_J = 0$ . This leads to a  $3 \times 3$  matrix.

$ 0, m_J = 0\rangle$	$ 1, m_J = 0\rangle$	$ 2, m_J = 0\rangle$	
$\epsilon_0$	$\sqrt{\frac{2}{3}}\mu_B B (g'_L - g'_S - \frac{1}{6}g_x)$	$0$	(5.12)
$\sqrt{\frac{2}{3}}\mu_B B (g'_L - g'_S - \frac{1}{6}g_x)$	$\epsilon_1$	$\sqrt{\frac{1}{3}}\mu_B B (g'_L - g'_S + \frac{2}{15}g_x)$	
$0$	$\sqrt{\frac{1}{3}}\mu_B B (g'_L - g'_S + \frac{2}{15}g_x)$	$\epsilon_2$	

Diagonalizing matrices (5.10-5.12) leads to the following corrections  $\delta\omega_{\text{Zeeman}}(J, m_J)$  to the  $2P_J$  energy levels,

$$\delta\omega_{\text{Zeeman}}(0, 0) = (0.044\,304\text{ kHz/G}^2)B^2, \quad (5.13)$$

$$\delta\omega_{\text{Zeeman}}(1, \pm 1) = \pm(2.100\,917\text{ MHz/G})B + (0.214\,762\text{ kHz/G}^2)B^2, \quad (5.14)$$

$$\delta\omega_{\text{Zeeman}}(2, \pm 1) = \pm(2.100\,916\text{ MHz/G})B - (0.214\,762\text{ kHz/G}^2)B^2, \quad (5.15)$$

$$\delta\omega_{\text{Zeeman}}(2, 0) = -(0.286\,350\text{ kHz/G}^2)B^2. \quad (5.16)$$

The coefficients in eqs. (5.13-5.16) are needed to only 6 digits of precision in order for the associated magnetic correction errors to be as small as several hertz. Since experimentally these coefficients are known to about 7 digits of precision, and theoretically to many more, the only source of error introduced by the magnetic field arises from the uncertainty in  $B$ , as long as  $B$  is sufficiently small, as is the case in this work.

### 5.1.2 Line Shapes in a Magnetic Field

An applied magnetic field resolves Zeeman sublevels of both the metastable  $2^3S_1$  state and the excited  $2^3P_J$  states. Doppler-free pump and probe saturation spectroscopy is used to study the  $2^3S_1 - 2^3P_J$  transitions, and polarization directions for the pump and probe can be independently set. Depending on the polarization configuration, the resulting line shapes are qualitatively different. They exhibit different numbers of resonance peaks, and some show crossover resonances that arise from the pump and probe interacting with moving atoms. This section gives an overview of the line shapes for parallel and perpendicular pump and probe polarizations. The parallel polarization configuration was chosen for the fine structure interval measurements because of the relative simplicity of the line shapes.

For small  $B$ , the  $g_J$  value from a simple vector model,

$$g_J \approx 1 + \frac{J(J+1) + S(S+1) - L(L+1)}{2J(J+1)}, \quad (5.17)$$

gives

$$g_J^{2S} \approx 2, \quad \text{and} \quad (5.18)$$

$$g_J^{2P} \approx \frac{3}{2}. \quad (5.19)$$

The Zeeman frequency shifts are

$$\Delta_Z = m_J g_J \Delta \quad (5.20)$$

for small  $B$ , where

$$\Delta \equiv \mu_B B \simeq 1.4 \frac{\text{MHz}}{\text{G}} \times B. \quad (5.21)$$

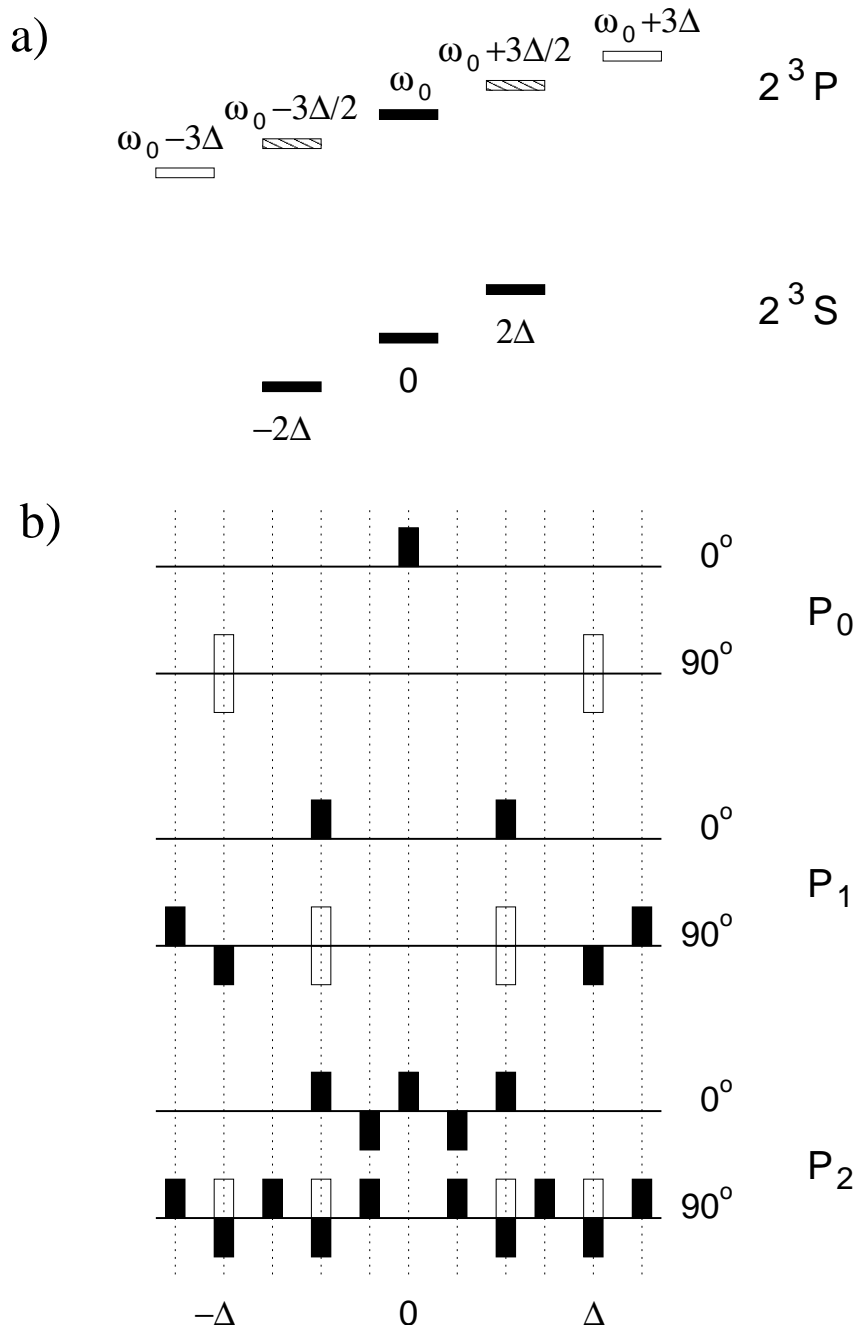


Figure 5.1: (a) Schematic representation of linear Zeeman splitting for  $2^3S$  and  $2^3P$ . The unperturbed transition frequency is  $\omega_0$ , and  $\Delta = \mu_B B$ . (b) Peak locations for the  $2^3S_1 - 2^3P_{0,1,2}$  transitions at  $0^\circ$  and  $90^\circ$  angles between pump and probe polarization directions. Black marks face up or down depending on whether they correspond to peaks with positive or negative amplitudes. White marks correspond to the peaks that have positive or negative amplitudes depending on helium pressure.

Fig. 5.1 (a) illustrates the linear splitting of the  $2^3S$  and  $2^3P$  energy levels in a magnetic field as given by eq. (5.20). Measured line shapes in a magnetic field depend on pump and probe polarizations. Fig. 5.1 (b) shows saturation peak locations for the three  $2^3S_1 - 2^3P_J$  transitions and  $0^\circ$  and  $90^\circ$  angles between pump and probe polarizations. Pump polarization is parallel to the direction of the external field. Black marks facing up or down correspond to peaks with positive or negative amplitudes. White marks correspond to peaks with amplitudes that are positive or negative depending on helium pressure.

Real saturation peaks in Fig. 5.1 (b) are always positive, in a sense that probe transmission increases in the presence of the pump. Pump and probe interact with atoms in the zero velocity group, in the absence of a frequency offset between them. Crossover resonances occur when pump and probe interact with moving atoms. For instance, when the  $2^3S - 2^3P$  transition is studied in the  $0^\circ$  configuration, one of the crossover dips arises when the pump is resonant with  $2^3S_1 (m_J = 0) - 2^3P_2 (m_J = 0)$  and the probe is resonant with  $2^3S_1 (m_J = 1) - 2^3P_2 (m_J = 1)$ . If, as in this example, pump and probe are not coupled to a common atomic sublevel, the crossover resonance always has a negative sign, with a diminishing amplitude toward higher pressures. The coupling between pump and probe in this case occurs through spontaneous emission alone, and at high pressures collisional de-excitation dominates over spontaneous emission. If pump and probe interact with different velocity groups but are coupled to the same excited state sublevel, as for  $2^3S_1 (m_J = 0) - 2^3P_0 (m_J = 0)$  and  $2^3S_1 (m_J = 1) - 2^3P_0 (m_J = 0)$ , the crossover resonance has a positive amplitude at high pressures and a negative amplitude at low pressures. At high pressures, saturation of the upper

level dominates, and probe transmission increases in the presence of the pump. At low pressures, optical pumping into  $2^3S_1 (m_J = 1)$  through spontaneous emission leads to a decrease of probe transmission in the presence of the pump. Finally, if pump and probe are coupled to the same  $2^3S$  sublevel but different  $2^3P$  sublevels, as for  $2^3S_1 (m_J = 0) - 2^3P_2 (m_J = 0)$  and  $2^3S_1 (m_J = 0) - 2^3P_2 (m_J = 1)$ , the crossover resonance always has a positive amplitude, since optical pumping plays no role.

For the fine structure measurements, pump and probe polarizations were fixed to be parallel to each other and to the external magnetic field. This configuration leads to the simplest spectra, as shown in the upper traces of Fig. 5.1 (b). The  $2^3S_1 - 2^3P_0$  and  $2^3S_1 - 2^3P_1$  line shapes contain one and two cleanly resolved peaks, respectively, at the magnetic field of approximately 50 G. Even in the simplest polarization configuration, however, the  $2^3S_1 - 2^3P_2$  line shape has two negative crossover peaks, as well as three positive resonances. The presence of crossover resonances is inherent in the nature of this transition and cannot be circumvented by a choice of light polarization. Larger magnetic fields are needed to achieve a Zeeman resolution of  $2^3S_1 - 2^3P_2$  comparable to that of the other two transitions. This is planned for the future of this experiment. At the low fields used here, the presence of the crossover resonances in close proximity to the real resonances is not expected to cause an appreciable error in the frequency measurements due to the symmetry of the line shape, since the average of the two outermost peak frequencies is the measured quantity. The measurements of the  $2^3S_1 - 2^3P_2$  linear Zeeman splitting, however, may be affected by the presence of the crossover resonances, and can lead to the field measurement errors on the order of 10 mG. For this reason, the Zeeman splitting of the  $2^3S_1 - 2^3P_1$  line was used for

the magnetic field measurements.

### 5.1.3 Calculation of the Magnetic Field from Line Splitting

The magnitude of the magnetic field in the discharge cell is extracted from Zeeman splitting of the  $2^3S_1 - 2^3P_1$  saturation peaks with  $m_J, m'_J = -1$  and  $m_J, m'_J = 1$ , as in Fig. 6.1 (b). This quantity is not affected by the quadratic shift of eq. (5.14). The splitting of the  $2^3S$  state is obtained from eqs. (5.8) and (5.9),

$$\Delta_{Z_S} = \mu_B g_S^{2S} = 2.802\,381 \text{ MHz/G.} \quad (5.22)$$

The  $2^3P_1$  splitting is given by eqs. (5.11) and (5.14),

$$\Delta_{Z_1} = \frac{1}{2}\mu_B(g'_L + g'_S - \frac{1}{6}g_x) = 2.100\,917 \text{ MHz/G.} \quad (5.23)$$

The measured splitting of the  $2^3S_1 - 2^3P_1$  line, or half the distance between the two peaks in Fig. 5.1 (b), is

$$d_1 \equiv \Delta_{Z_S} - \Delta_{Z_1} = 0.701\,464 \text{ MHz/G.} \quad (5.24)$$

Finally, eq. (5.24) yields the value of the magnetic field,

$$B = 1.42559(d_1/\text{MHz}) \text{ G.} \quad (5.25)$$

Splitting  $d_2$  of the  $2^3S_1 - 2^3P_2$  peaks with  $m_J, m'_J = -1$  and  $m_J, m'_J = 1$  yields the same  $B$  value as eq. (5.25).

## 5.2 Magnetic Field Coils

A uniform magnetic field in the helium cell is created with a set of two rectangular coils in the Helmholtz configuration. The cross section of the coils is shown in Fig.

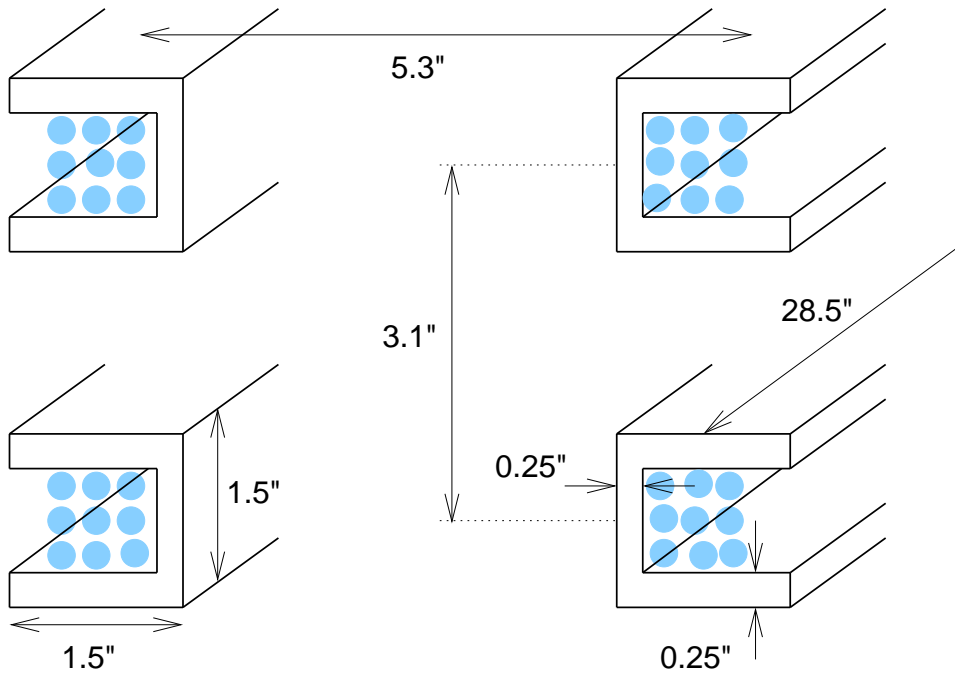


Figure 5.2: Cross section of the rectangular coils used to create a uniform vertical magnetic field in the helium cell.

5.2 along with relevant dimensions. Gauge 16 magnet wire is wound on aluminum supports with a 0.054" pitch. Each coil consists of 14 layers, with 17 turns in each layer. Constant current through the coils is provided by Agilent 6612C 20V, 2A DC power supply. In addition to the vertical field coils, the cell is surrounded by a solenoid designed to provide a transverse magnetic field for study of systematic effects. The solenoid consists of 360 turns of gauge 16 magnet wire wound on aluminum tubing with a 3.5" outer diameter. Resistances of the vertical field coils and the solenoid are 1.5 and 10.6 ohms, respectively. The magnetic coil assembly is enclosed in a single-layer  $\mu$ -metal magnetic shield. The shield is 30" long and has a thickness of 0.04".

Since a magnetic field inhomogeneity can give rise to systematic errors, the field

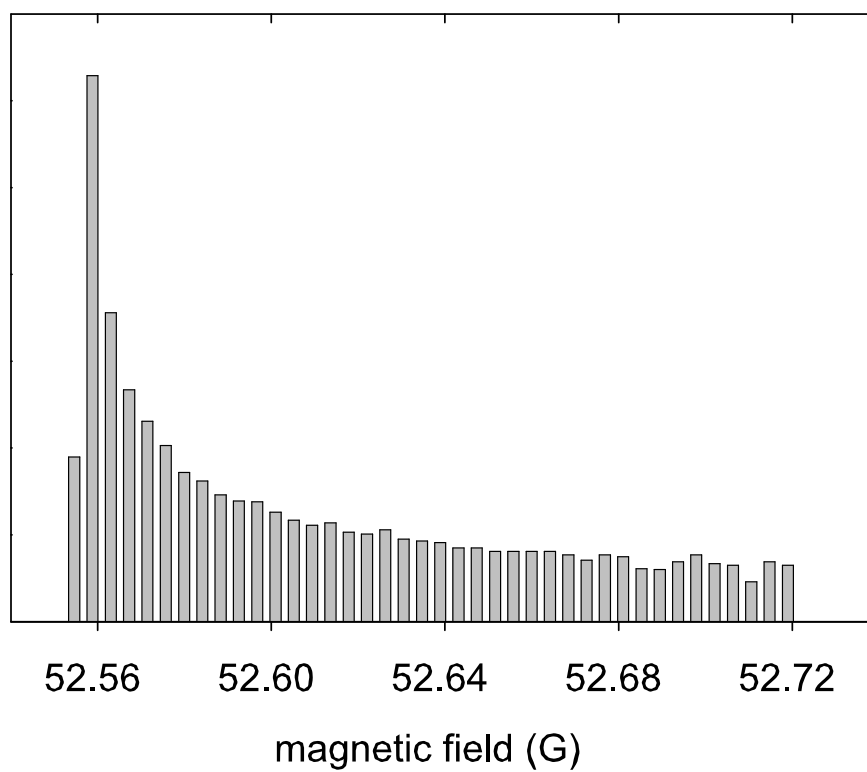


Figure 5.3: Calculated distribution of vertical magnetic field strengths about the measured average field in the illuminated region of the helium cell, assuming this region is spatially uniform, which is the case for an optically thin medium.

distribution in the illuminated region of the cell was calculated by substituting the coil geometry into the Biot-Savart law,

$$\vec{B}(\vec{r}) = \frac{I}{c} \oint \frac{d\vec{s}' \times (\vec{r} - \vec{r}')}{|\vec{r} - \vec{r}'|^3}. \quad (5.26)$$

The resulting field distribution about the measured average field is plotted as a histogram in Fig. 5.3. This calculation accounted for the finite cross section of the coils. The field inhomogeneity introduces errors in two ways. First, the observed line shape is broadened and, in general, slightly non-Lorentzian, since the net signal is a superposition of signals arising from all atoms in the cell, and the atoms see the field distribution of a finite width. This can lead to errors in the line centers and in the measurement of the average magnetic field. The second cause of error is the fact that the average field squared,  $\langle B \rangle^2$ , does not equal  $\langle B^2 \rangle$ . The former is the quantity used in the quadratic magnetic shift correction, and the latter is the average of actual quadratic shifts experienced by the atoms. This effect is negligible for the fields and quadratic shift coefficients involved in this experiment. For helium in a 50 G magnetic field produced by the coils in this setup, all errors associated with the field inhomogeneities are very small. This was ascertained by simulating a line shape based on an atomic ensemble exposed to the field distribution of Fig. 5.3. If the actual field distribution is five times less homogeneous than that depicted in Fig. 5.3, it was determined that the errors on fine structure intervals due to magnetic line shape distortion and error on the average field measurement resulting from inhomogeneities do not exceed 0.1 kHz.

A histogram of magnetic field measurements representing a typical data run is shown in Fig. 5.4. The standard deviation of the measurements for approximately

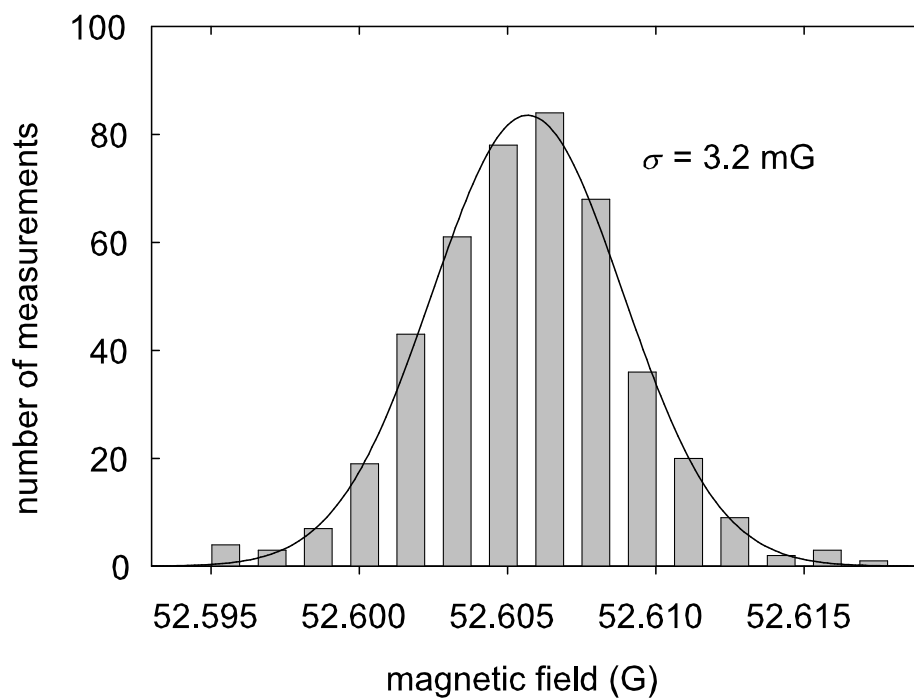


Figure 5.4: Magnetic field measurement histogram of a typical data run. The standard deviation of the measurements is only 3.2 mG.

30 hours of data collection is about 3 mG.

# Chapter 6

## Systematic Study of the Fine Structure Intervals

The excellent signal to noise ratio attained by performing helium spectroscopy in a discharge cell facilitates the careful investigation of possible systematic errors. These are described below, and include velocity changing collisions, pressure shifts, light-pressure-induced shifts, light shifts, discharge power shifts, and magnetic shifts.

### 6.1 Measured Line Shapes

The measured line shapes for the  $2^3S_1 - 2^3P_J$  optical transitions are shown in Figs. 6.1 (a, b, c). The  $2^3S_1 - 2^3P_0$  and  $2^3S_1 - 2^3P_1$  lines are fitted to a single and double Lorentzian with a flat background, respectively, and the  $2^3S_1 - 2^3P_2$  line is fitted to a sum of three positive and two negative Lorentzians with a flat background. The small error bars on the points are statistical, and correspond to standard errors

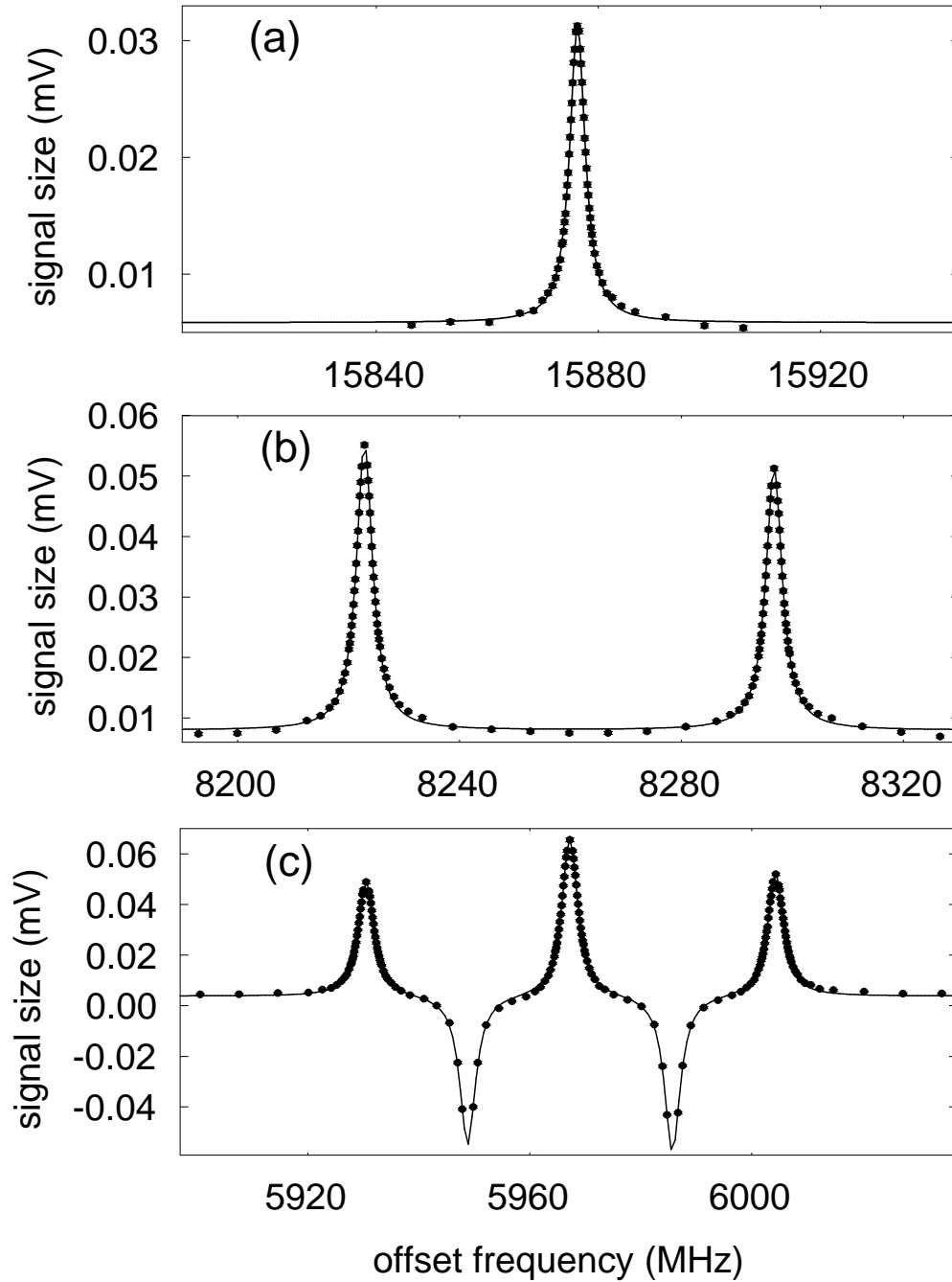


Figure 6.1: Line shapes of (a)  $2^3S_1 - 2^3P_0$ , (b)  $2^3S_1 - 2^3P_1$ , and (c)  $2^3S_1 - 2^3P_2$  helium transitions at a 30 mTorr pressure in a 52.6 G magnetic field parallel to the pump and probe polarization axis. The basic configuration of peaks and crossover resonances is as depicted in Fig. 5.1 for parallel pump and probe polarizations.

of the mean of 300 individual lock-in readings. Each scan consists of about 100 points, and the total averaging and readout time for each point is about 1 s. The total duration of a pair of line scans corresponds to the highest stability region of the optical reference frequency, as shown in Fig. 3.26.

## 6.2 Velocity Changing Collisions

The advantage of saturation spectroscopy with pump and probe beams lies in the possibility of interrogating a single atomic velocity group, thus eliminating Doppler broadening. If atomic velocities do not change during the  $0.5 \mu\text{s}$  it takes to optically pump the atom into a dark state, the spectral width of the measured line corresponds to the natural lifetime of the excited level, possibly broadened by mechanisms such as laser power or phase changing collisions. However, if atomic velocities change in the course of a pumping and probing cycle, for instance through collisions with other atoms, a new broadening mechanism arises. After interacting with the pump beam, some atoms undergo collisions that alter their velocity by an amount greater than  $\sim \gamma/k$ , which corresponds to the natural line width. The hole in the velocity profile burned by the pump beam partially diffuses to other velocity groups. The degree of this velocity diffusion depends on the typical collision strength as well as the number of collisions that occur in a detection cycle.

Velocity diffusion is observed in the helium experiment as a broad thermal pedestal under the narrow saturation signal. Pumped metastable atoms contributing to the pedestal have undergone velocity changing collisions (vcc) with ground state helium atoms, while the atoms contributing to the narrow peak have undergone only phase

changing and very weak velocity changing collisions.

The width of the vcc pedestal in metastable helium is typically over ten times broader than the saturation signal width. Therefore, if a spectral line is scanned over a frequency interval of just several widths and fitted to a Lorentzian profile, the residuals resulting from the vcc pedestal are not very noticeable. However, scanning over a much wider frequency range exposes the vcc pedestal in fit residuals, and necessitates a more detailed consideration of the effects of velocity changing collisions that can slightly shift the frequencies extracted from the data.

### 6.2.1 Line Shape Including Velocity Changing Collisions

Rate equations leading to a Lorentzian line profile for a closed atomic system were considered in Sec. 4.2 in the context of optical pressure. In the presence of a magnetic field, Zeeman degeneracies are removed, and the atom is nearly a two-level system with velocity  $v$  and equilibrium ground and excited state populations  $g(\omega, kv)$  and  $e(\omega, kv)$  that depend on the laser frequency  $\omega$ . The decay rates are  $\gamma_g$  and  $\gamma_e$ , and the repopulation rates are

$$\Lambda_g = \gamma_{eg}e + C_g, \quad (6.1)$$

$$\Lambda_e = C_e, \quad (6.2)$$

where  $\gamma_{eg}$  is the decay path from level  $e$  to level  $g$  and  $e$ , and  $C_g$  and  $C_e$  are the rates of population of  $g$  and  $e$  through discharge and other means. The rate equations [47] are

$$\begin{aligned} \dot{g}(\omega, kv) = 0 = & R_1(\omega, kv)[e(\omega, kv) - g(\omega, kv)] + R_2(\omega, kv)[e(\omega, kv) - g(\omega, kv)] \\ & - \gamma_g g(\omega, kv) + \gamma_{eg} g(\omega, kv) + C_g, \end{aligned} \quad (6.3)$$

$$\begin{aligned} \dot{e}(\omega, kv) = 0 = R_1(\omega, kv)[g(\omega, kv) - e(\omega, kv)] + R_2(\omega, kv)[g(\omega, kv) - e(\omega, kv)] \\ - \gamma_e e(\omega, kv) + C_e, \end{aligned} \quad (6.4)$$

where the transition rates  $R_1$  and  $R_2$  induced by the probe and pump are defined in eq. (4.23) and are proportional to the respective saturation parameters,  $s_1$  and  $s_2$ .

The steady-state solution of these equations reveals that for small light intensities and a large Doppler width,

$$\beta(\omega, kv, s_2 = 0) - \beta(\omega, kv) \propto R_2(\omega, kv), \quad (6.5)$$

where  $\beta$  is  $g$  or  $e$ , and assuming that the repopulation rates  $\Lambda_{g,e}$  are not significantly changed by the radiation field. Eqs. (4.28-4.30) then yield the observed probe transmission signal

$$S(\omega) = S_0 \frac{1}{1 + \frac{(\omega - \omega_0)^2}{(\gamma/2)^2}}, \quad (6.6)$$

where the line width  $\gamma = \gamma_g + \gamma_e$ . This standard Doppler-free spectroscopy signal corresponds to the first term of the line shape in eq. (4.21) that was obtained starting from the known velocity-dependent absorption coefficient.

Velocity changing collisions are incorporated into the model by adding cross-relaxation terms [61] to the rate eqs. (6.3-6.4),

$$[\dot{\beta}(\omega, kv)]_x = -\beta(\omega, kv) \int W_\beta(v \rightarrow v') dv' + \int \beta(\omega, kv') W_\beta(v' \rightarrow v) dv'. \quad (6.7)$$

$W(v \rightarrow v')$  is a collision kernel, or a probability density that an atom changes its velocity from  $v$  to  $v'$  as a result of a collision.

In the strong collision model considered in [61], atoms fully thermalize after a single collision. The collision kernel is then independent of the initial velocity  $v$ ,

$$W_\beta^{\text{strong}}(v \rightarrow v') = \gamma_\beta^x \frac{1}{\sqrt{\pi} v_D} e^{-(v'/v_D)^2}, \quad (6.8)$$

where  $\gamma_\beta^x$  is the cross-relaxation rate of  $\beta$  due to elastic collisions.  $W_\beta^{\text{strong}}$  reflects the Maxwellian velocity distribution of eq. (3.14).

In the more general situation of weak collisions that is valid when atoms do not lose memory of their initial velocities after a single collision, the simplest collision kernel [62, 63] is

$$W(v \rightarrow v') = \gamma^x \frac{1}{\sqrt{\pi}u} e^{-(v'-\alpha v)^2/u^2}, \quad (6.9)$$

where  $\alpha v$  is the average velocity of an atom with initial velocity  $v$  following a collision, and

$$u \equiv \sqrt{1 - \alpha^2} v_D. \quad (6.10)$$

The parameter  $\alpha$  is related to the strength of a collision. For very weak collisions,  $\alpha \approx 1$ , while for strong collisions  $\alpha \approx 0$ . In the limit of very strong collisions,  $\alpha = 0$ , and eq. (6.8) is recovered from eq. (6.9).

The addition of cross-relaxation terms in eq. (6.7) to the rate eqs. (6.3-6.4) leads to the modified versions of eqs. (6.5) and (6.6),

$$\beta_x(\omega, kv, s_2 = 0) - \beta_x(\omega, kv) \propto R_2(\omega, kv) + C'_x \int R_2(\omega, kv') e^{-(v-\alpha v')^2/u^2} dv' \quad (6.11)$$

and

$$S_x(\omega) = S_0 \left[ \frac{1}{1 + \frac{(\omega - \omega_0)^2}{(\gamma/2)^2}} + C_x \exp \left( -\frac{(\omega - \omega_0)^2}{\left(\frac{1-\alpha}{1+\alpha}\right) (kv_D)^2} \right) \right], \quad (6.12)$$

where  $C_x$  is the cross-relaxation parameter.

Figs. 6.2 (a) and 6.3 (a) show scans of the  $2^3S_1 - 2^3P_0$  and  $2^3S_1 - 2^3P_1$  lines, respectively, at the pressure of 80 mTorr. The scans span several line widths in order to measure the vcc pedestal. The solid lines are Lorentzian fits to the data, and normalized fit residuals are shown below the line scans. Since the fits ignore the vcc

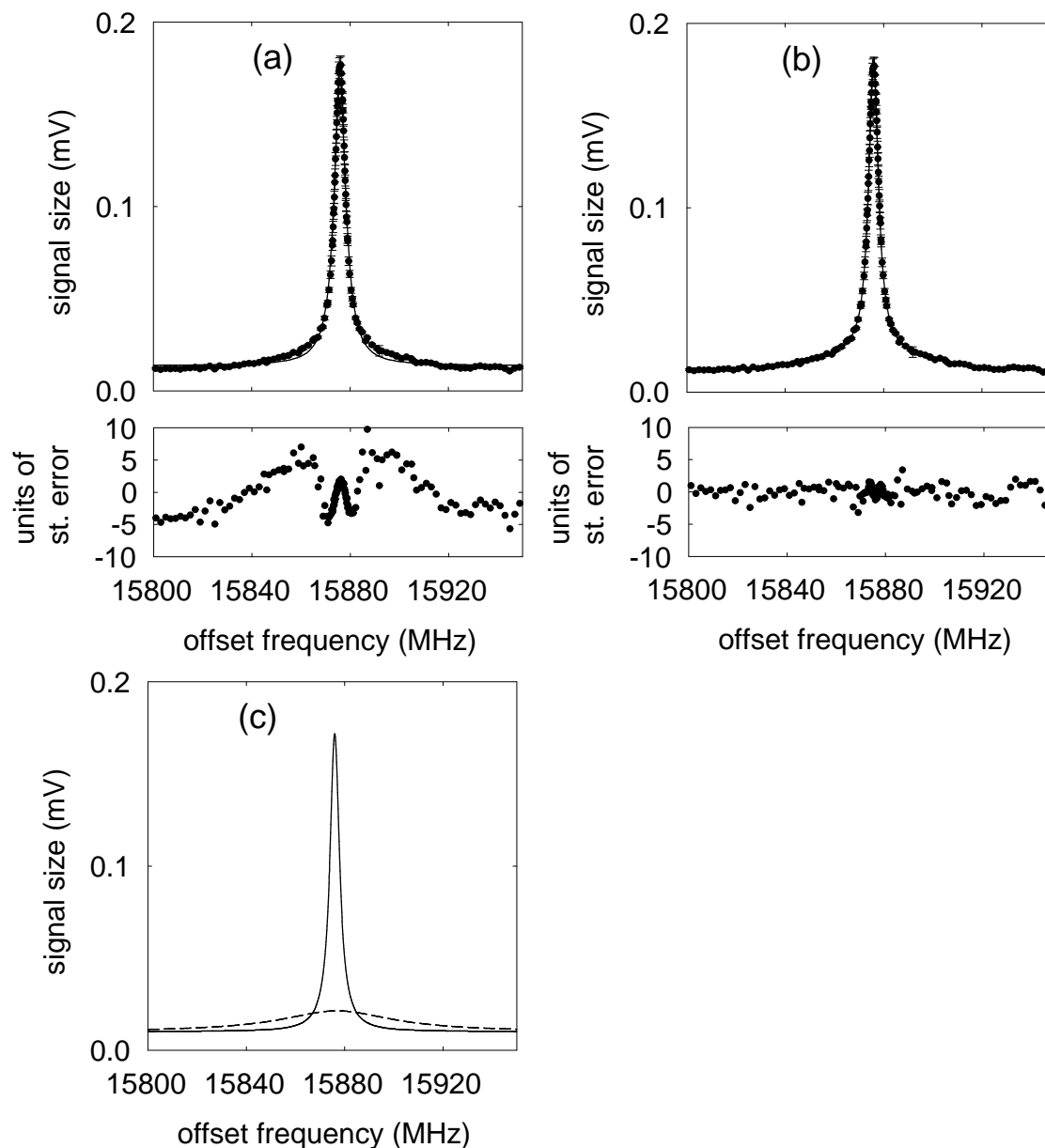


Figure 6.2: The  $2^3S_1 - 2^3P_0$  line scan at 80 mTorr, showing a large portion of the broad background. (a) The line is fitted to only a single Lorentzian. Fit residuals, weighted and normalized by the statistical errors on the points, are shown below. (b) The line is fitted to a sum of a Lorentzian peak and a broad Gaussian background. Normalized weighted fit residuals are shown. (c) The saturation and vcc contributions to the line shape obtained from the fit in (b) are shown separately, using solid and dashed lines, respectively.

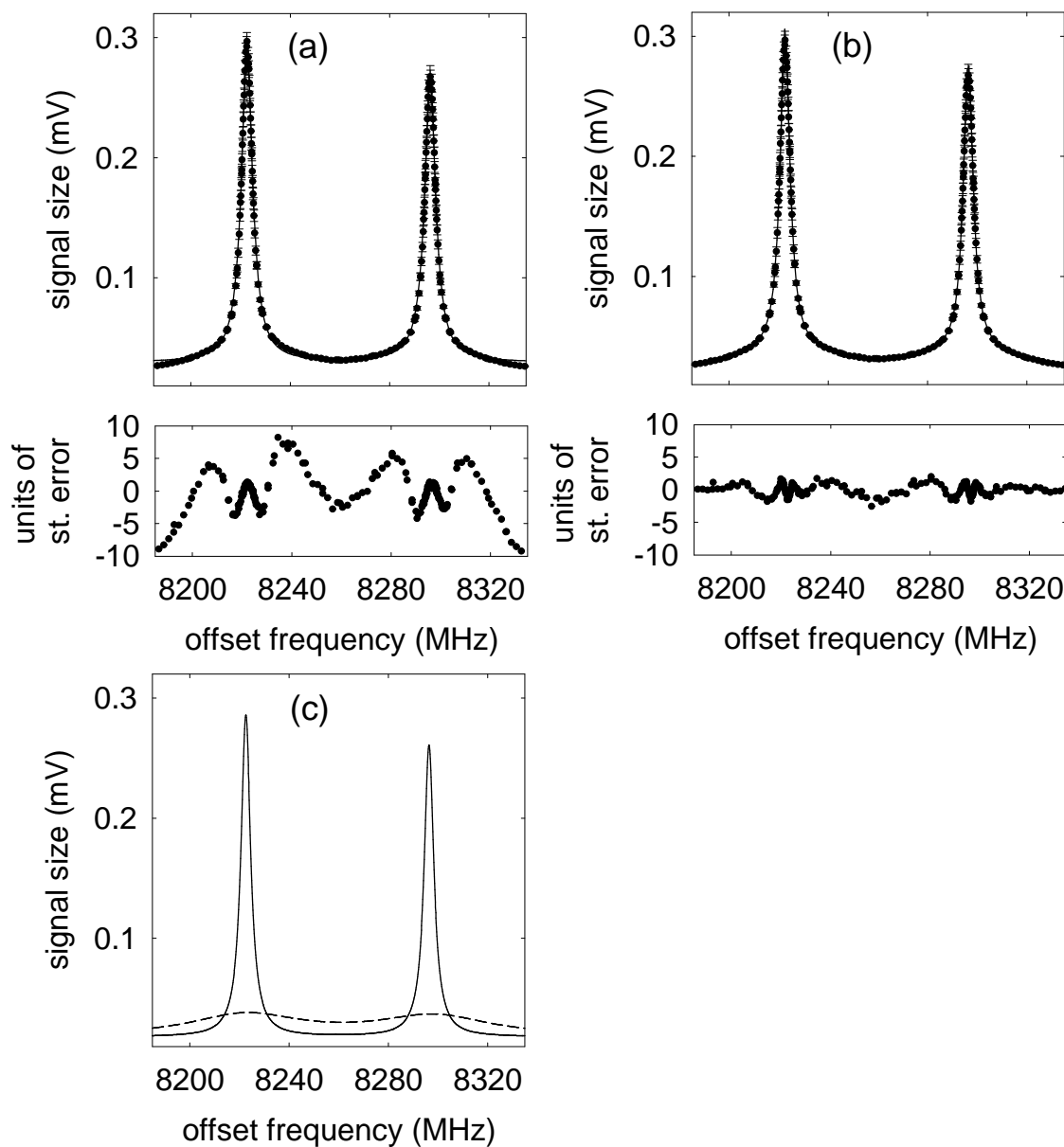


Figure 6.3: The  $2^3S_1 - 2^3P_1$  line scan at 80 mTorr, showing a large portion of the broad background. (a) The spectrum is fitted to a sum of two Lorentzians. Fit residuals, weighted and normalized by the statistical errors on the points, are shown below. (b) The spectrum is fitted to a sum of two Lorentzian peaks and broad Gaussian backgrounds corresponding to each narrow peak. Normalized weighted fit residuals are clearly smaller. (c) The saturation and vcc contributions to the line shape obtained from the fit in (b) are shown separately, using solid and dashed lines, respectively.

pedestal, the residuals show pronounced broad backgrounds. In Figs. 6.2 (b) and 6.3 (b), the same data sets are shown with fits that are superpositions of narrow Lorentzians and broad backgrounds. The residuals are significantly reduced. Figs. 6.2 (c) and 6.3 (c) show the narrow and broad components of the signals found from the fits in parts (b).

The typical  $C_x$  values measured in this experiment are about 0.055, which corresponds to a pedestal contribution that is about 5% of the peak height. The typical broad background half width is 20 MHz, which yields

$$\alpha = 0.998. \quad (6.13)$$

This parameter describes the magnitude of a typical collisional velocity change. A value of  $\alpha$  so close to 1 is characteristic of very weak vcc. According to eq. (6.10), it corresponds to a collisional rms velocity change

$$\Delta v_{\text{rms}} = \sqrt{\frac{1 - \alpha^2}{2}} v_D \simeq 0.045 v_D \sim 50 \text{ m/s}. \quad (6.14)$$

This implies that helium vcc in the discharge cell have very large impact parameters, leading to small path deflections.

The widths of the helium vcc pedestals only weakly depend on pressure, while their heights increase by a larger factor over the same pressure range, as shown in Fig. 6.4. It is an indication that the observed pedestals are most likely due to a single velocity changing collision, and their widths are fixed by  $\Delta v_{\text{rms}}$  of a single collision. As pressure increases, more atoms undergo vcc, leading to an increase of the pedestal height. Some atoms may experience more than a single vcc in one probing cycle, particularly at the higher end of the pressure range, but these atoms contribute to

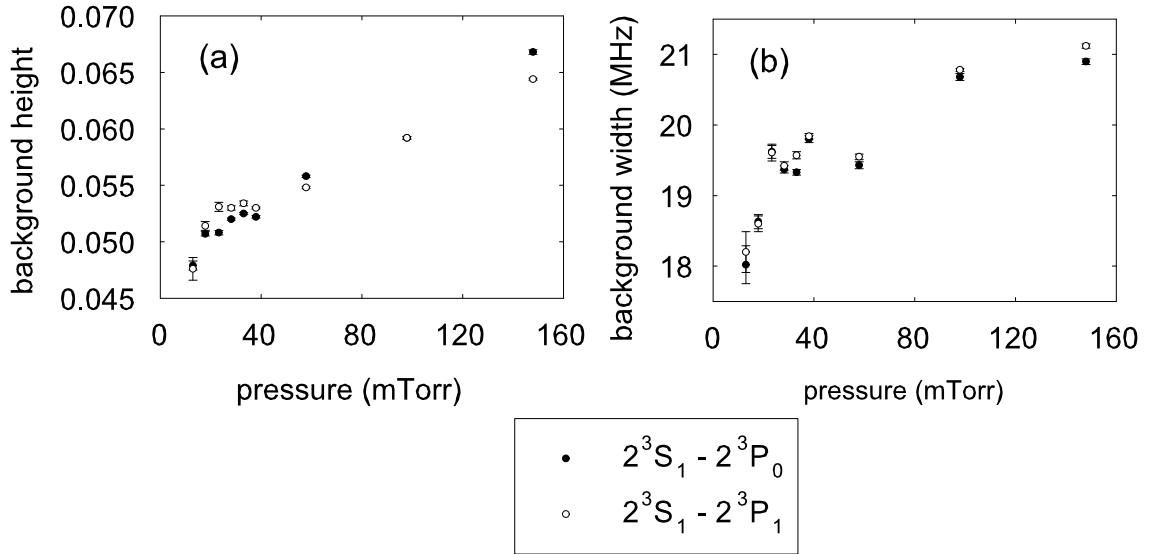


Figure 6.4: Parameters of the broad signal backgrounds arising from velocity changing collisions. (a) Relative heights. (b) Gaussian half widths.

increasingly smaller and broader pedestals [64]. Given the single-collision assumption, the cross relaxation coefficient is expected to be [64]

$$C_x = \frac{\gamma}{kv_D} \sqrt{\frac{\pi}{1 - \alpha^2}} \frac{\gamma_{2S}^x}{\gamma_0 + \gamma_{2S}^x}. \quad (6.15)$$

Since the  $2^3P$  state quickly decays, only the cross-relaxation rate of the metastable state  $\gamma_{2S}^x$  contributes to the vcc pedestal. This is the rate at which velocity changing collisions of metastable atoms with ground state helium atoms take place. The rate of  $2^3S$  Zeeman sublevel relaxation is  $\gamma_0$ . This is the combined rate of the processes that quench the metastable state sublevel population.

For metastable helium, the cross section for collisional relaxation of Zeeman sublevels is extremely small due to the zero angular momentum of the ground state  $1^1S$  atoms with which they collide. The metastable state quenching collision cross section is also negligible due to spin conservation. Therefore, the rate constant introduced in

eq. (6.15) that limits vcc,  $\gamma_0$ , is most likely determined by transit time. For optical beams with diameter  $d = 1$  cm, transit time is [50]

$$\tau_t = \frac{\pi d}{4v_D} = 9.6 \mu\text{s}. \quad (6.16)$$

Then  $\gamma_0 = 1/\tau_t \simeq 0.1$  MHz.

Eq. (6.15) for  $C_x$  is consistent with observations. In the limit of  $\gamma^x \gg \gamma_0$ ,  $C_x \simeq 0.1$ , close to the observed values.

The vcc pedestal is frequency shifted relative to the narrow saturation peak by about 2 MHz, or 5% of its width. The shift is accounted for in line fitting by allowing the center frequency of the pedestal be a free parameter. The physical origin of this shift is not currently understood. The frequency offset between pump and probe beams  $\delta_0 = 2$  MHz can cause a shift of the pedestal

$$\delta\omega_{\text{offset}} = \frac{\delta_0}{2} \frac{1 - \alpha}{1 + \alpha} = 1 \text{ kHz} \quad (6.17)$$

due to a slight anisotropy of collisional velocity changes resulting from the non-zero initial atomic velocity. This is much too small to account for the observed shift. In addition, the offset  $\delta_0$  was varied with no effect on the center frequency of the pedestal. The shift is also independent of other experimental parameters including pressure, optical power, and laser beam geometry. An interesting feature of the shift is that it typically has different values for the two peaks of the  $2^3\text{S}_1 - 2^3\text{P}_1$  line, but the average of the two values nearly equals the  $2^3\text{S}_1 - 2^3\text{P}_0$  vcc pedestal shift.

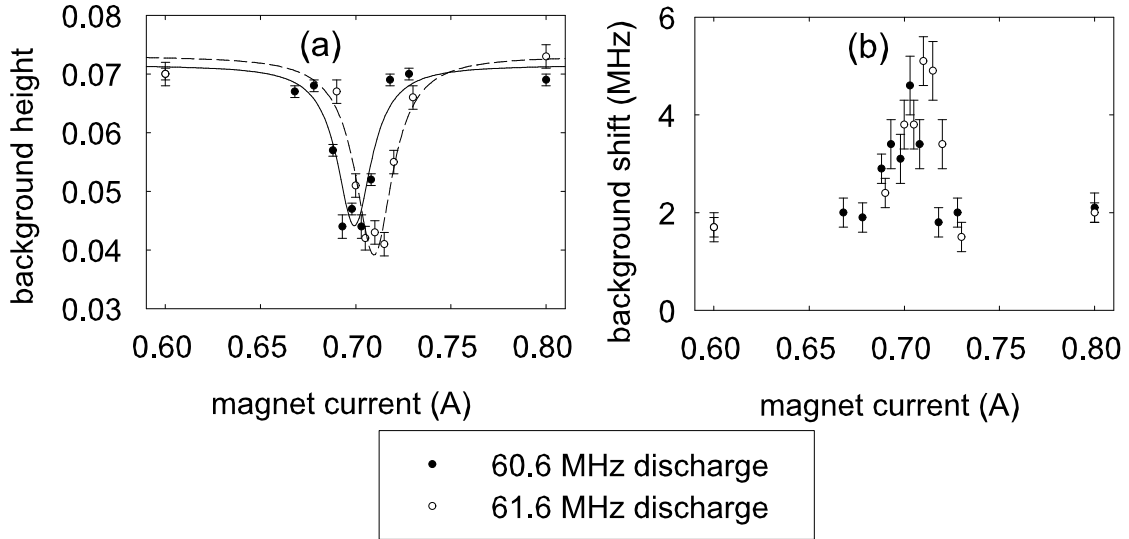


Figure 6.5: Magnetic resonance of the 60 MHz rf discharge with the  $2^3\text{S}$  Zeeman splitting occurs at a vertical magnetic field of about 21.7 gauss, set by the coil current of 0.7 A. (a) Relative height of the broad background, for 60.6 and 61.6 discharge frequencies. (b) Relative frequency shift of the broad background, for 60.6 and 61.6 discharge frequencies.

## 6.2.2 Limiting Velocity Changing Collisions with Magnetic Resonance

Broad pedestals characteristic of velocity changing collisions depend on the number of such collisions during the lifetime of the metastable state, or  $\gamma_{2\text{S}}^x/\gamma_0$ , as in eq. (6.15). One way to increase  $\gamma_0$  and thus limit the vcc pedestal is by applying a transverse rf magnetic field that induces magnetic resonance transitions between the  $2^3\text{S}$  Zeeman sublevels [65]. This broadens the  $2^3\text{S}$  state and shortens its lifetime.

The rf discharge used to create metastable atoms typically operates at 60.6 MHz. This frequency is resonant with the  $2^3\text{S}$  Zeeman splitting at the field of about 21.7 Gauss, or the magnet coil current of 0.70 A. Fig. 6.5 (a) shows the shape of the magnetic resonance as the relative vcc background height decreases at the correct

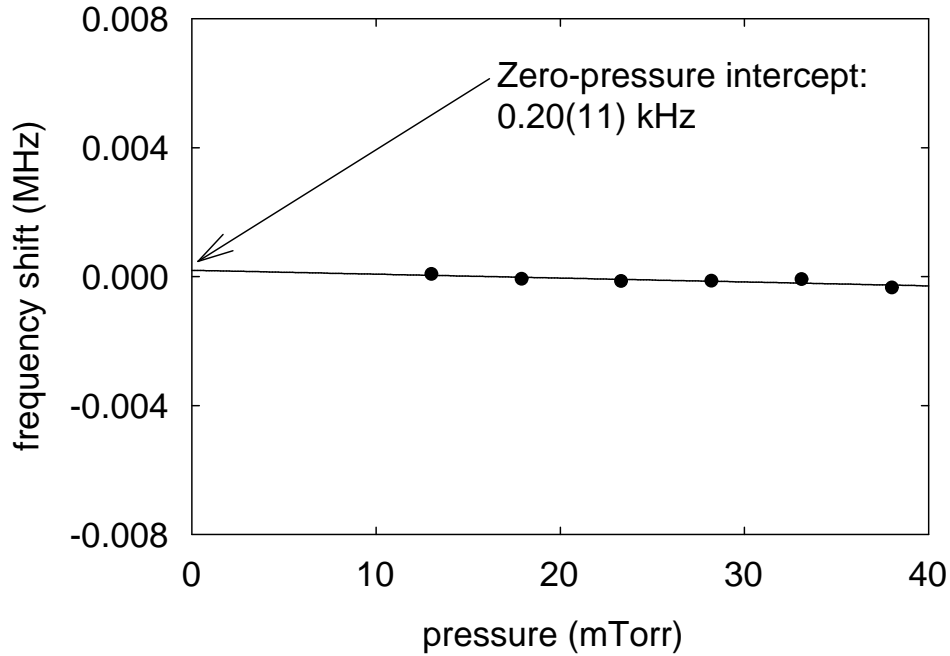


Figure 6.6: The  $2^3P_0 - 2^3P_1$  interval error that arises if vcc pedestals are not accounted for in the line fits. The zero-pressure intercept provides an estimate of the vcc error for the  $2^3P_{0,1} - 2^3P_2$  intervals.

current setting. Filled and open circles correspond to the discharge frequencies of 60.6 and 61.6 MHz, and the respective resonances are separated by 0.01 A, as predicted. At the rf power necessary to operate the discharge, the decrease in the vcc background is about 50%, and the full width of the resonance is 0.74(6) G. Fig. 6.5 (b) shows the relative frequency shift of the pedestal in the vicinity of the magnetic resonance. It indicates that the advantage of background reduction may be outweighed by the increase of the frequency shift in the magnetic resonance regime.

### 6.2.3 Systematic Errors Due to Velocity Changing Collisions

The vcc background Gaussians are shifted with respect to the saturation signal peaks. This causes small shifts of the resonance lines. For the fine structure measurements, the  $2^3S_1 - 2^3P_0$  and  $2^3S_1 - 2^3P_1$  line scans were fitted with full line shapes including narrow Lorentzians and broad Gaussian vcc pedestals, as well as with only Lorentzian line shapes. The systematic error introduced by vcc was estimated as the difference between the Lorentzian and the composite function fits, which was found to be the strictest available test of line shifts related to vcc. This error is plotted as a function of helium pressure in Fig. 6.6 and linearly extrapolated to zero pressure. The broad backgrounds for  $2^3S_1 - 2^3P_2$  line shapes are not readily measurable at the 50 G field since they are poorly resolved due to the presence of crossover resonances. Line shapes in the  $2^3P_{0,1} - 2^3P_2$  data sets were fitted to Lorentzians without broad backgrounds. Since the broad backgrounds are understood to have the same origin for all three optical transitions, the error due to vcc on both those intervals is taken to be twice the zero-pressure intercept value in Fig. 6.6, or 0.40 kHz. The vcc error assigned to the  $f_{01}$  interval is simply the zero-pressure intercept value, or 0.20 kHz. Although both the  $2^3S_1 - 2^3P_0$  and  $2^3S_1 - 2^3P_1$  scans were fitted to full line shapes, including the vcc contributions, the error was assigned because the cause of frequency shifts of the broad backgrounds, and essential element of the composite line fitting, is not currently known.

### 6.3 Linear Pressure Shifts

The fine structure interval measurements in a discharge cell are affected by collisional systematic shifts other than those related to vcc pedestals discussed in Sec. 6.2. When an atom approaches another atom in the cell, its energy levels are shifted as a result of the interaction between the atoms [47]. Pressure-related corrections are expected to be on the order of several kilohertz [57].

The assumptions applicable to this experiment are that a duration of a collision is much shorter than average time between collisions, that spectral lines are well separated, and that the atomic density is low and only binary collisions play a significant role [66]. These assumptions lead to Lorentzian line shapes with modified widths and line centers due to collisional broadening and shifts. Broadening and shift are proportional to pressure in the binary collision regime.

Inelastic collisions change the internal energy of an atom, and are also known as quenching collisions. Effectively, this process shortens the atomic lifetime and results in an additional damping term so that the decay rate  $\Gamma$  becomes  $\Gamma + \gamma_{\text{inel}}$ . Inelastic collisions generally do not lead to line shifts [47] and are therefore less important to this measurement than elastic collisions.

Elastic collisions are sometimes called phase changing collisions. If an atom is represented as a damped oscillator, inelastic collisions change the oscillation amplitude, while elastic collisions change its phase. Any energy transfer in an elastic collision results from atomic velocity changes. These collisions also give rise to broad pedestals in the line shapes described in Sec. 6.2. Elastic collisions lead to spectral broadening and shifts, and are considered below.

### 6.3.1 Linear Pressure Shift and Broadening Model

The simplest elastic collision model [47] describes the excited atomic electron as a damped oscillator with an amplitude at time  $t$  given by

$$y(t) = y_0 e^{i\omega_0 t + i\eta(t) - \Gamma t/2}, \quad (6.18)$$

where  $\eta(t)$  is the collisional phase shift accumulated over time  $t$ ,

$$\eta(t) = \int_0^t (\omega(t) - \omega_0) dt = \int_0^t \Delta\omega(t) dt. \quad (6.19)$$

It is useful to define the correlation function

$$\phi(\tau) = \frac{1}{y_0^2} e^{-i\omega_0 \tau} \lim_{t \rightarrow \infty} \frac{1}{t} \int_{-t/2}^{t/2} y^*(t) y(t + \tau) dt = \lim_{t \rightarrow \infty} \frac{1}{t} \int_{-t/2}^{t/2} e^{i(\eta(t+\tau) - \eta(t))} dt \equiv \langle e^{i\Delta\eta(\tau)} \rangle, \quad (6.20)$$

while temporarily neglecting the spontaneous decay rate  $\Gamma$ . Some algebra reveals that  $\phi(\tau)$  is directly related to the line shape  $L(\omega)$  through the Fourier transform of  $y(t)$ ,

$$L(\omega) \propto |\text{FT}(y)|^2 = \frac{y_0^2}{2\pi} \lim_{\tau \rightarrow \infty} \int_{-\tau/2}^{\tau/2} \phi(\tau) e^{i(\omega_0 - \omega)\tau} d\tau. \quad (6.21)$$

From eq. (6.20),

$$d\phi(\tau) = \phi(\tau + d\tau) - \phi(\tau) = \phi(\tau) \langle e^{i\varepsilon} - 1 \rangle, \quad (6.22)$$

where  $\varepsilon$  is the phase shift during a differential time interval  $d\tau$ . In time  $d\tau$ , the atom in a gas of number density  $n$  collides  $d\xi$  times, where

$$d\xi = 2\pi r dr n \bar{v} d\tau, \quad (6.23)$$

the impact parameter ranges from  $r$  to  $dr$ , and  $\bar{v}$  is the average relative velocity. If time average in eq. (6.22) is replaced with ensemble average, then

$$\langle e^{i\varepsilon} - 1 \rangle = 2\pi n \bar{v} d\tau \int_0^\infty \langle e^{i\eta(r)} - 1 \rangle r dr = -n \bar{v} d\tau (\sigma_b - i\sigma_s), \quad (6.24)$$

where the cross sections for broadening and shift are

$$\sigma_b \equiv 2\pi \int_0^\infty [1 - \cos \eta(r)] r dr, \quad (6.25)$$

$$\sigma_s \equiv 2\pi \int_0^\infty [\sin \eta(r)] r dr. \quad (6.26)$$

Combining eqs. (6.22) and (6.24) yields

$$\phi(\tau) = e^{-n\bar{v}\tau(\sigma_b - i\sigma_s)}. \quad (6.27)$$

Including the radiative and inelastic collisional damping rates,  $\Gamma$  and  $\gamma_{\text{inel}}$ , and substituting eq. (6.27) into eq. (6.21), gives the final line shape [47]

$$L(\omega) = \frac{1}{2\pi} \frac{(\Gamma + \gamma_{\text{inel}})/2 + n\bar{v}\sigma_b}{(\omega - \omega_0 - n\bar{v}\sigma_s)^2 + [(\Gamma + \gamma_{\text{inel}})/2 + n\bar{v}\sigma_b]^2}. \quad (6.28)$$

Since  $\gamma_{\text{inel}} \propto n$ , the line is shifted and broadened linearly with number density  $n$ , or, equivalently, with pressure  $p$ .

Shift and broadening cross sections in eqs. (6.26) and (6.25) depend on the phase shift parameter  $\eta$ . Phase shifts depend sensitively on the precise form of interaction between the atom and its perturber. If, for instance, the ground and excited levels of the atom at a distance  $r$  from the perturber see the potentials

$$V_g(b) = \frac{v_g}{r^k}, \quad (6.29)$$

$$V_e(b) = \frac{v_e}{r^k} \quad (6.30)$$

for an integer  $k \simeq 6$ , the phase shift parameter is [47]

$$\eta(b) = \int_{-\infty}^{\infty} \Delta\omega dt \propto \frac{v_g - v_e}{\bar{v}r^{k-1}}, \quad (6.31)$$

assuming a negligible atomic path deflection during a collision. The proportionality constant in eq. (6.31) can be positive or negative, depending on the relative orientation of atomic angular momenta. Typically, small impact parameters give rise to line broadening, whereas both small and large impact parameters contribute to line shifts.

### 6.3.2 Pressure Shifts and Broadening in Helium

Collisions that shift and broaden helium spectra relevant to this experiment occur predominantly between an atom in the  $2^3\text{S}$  or  $2^3\text{P}$  state and a ground state  $1^1\text{S}$  atom. Collisions between two metastables, and especially between a  $2^3\text{P}$  atom and a metastable atom, are extremely rare since the metastables make up only about 1 part in  $10^6$  of all helium atoms in the cell, as illustrated in Fig. 3.21.

For dilute helium near room temperature, the calculated elastic cross sections for collisions of  $2^3\text{S}$  and  $2^3\text{P}$  atoms with ground state atoms are approximately  $150 \text{ \AA}^2$  and  $200 \text{ \AA}^2$ , respectively [57]. The inelastic,  $J$ -changing collision cross sections  $\sigma_{\text{inel}}^{JJ'}$  are  $\sigma_{\text{inel}}^{02} \simeq 40 \text{ \AA}^2$ ,  $\sigma_{\text{inel}}^{12} \simeq 20 \text{ \AA}^2$ , and  $\sigma_{\text{inel}}^{01} \simeq 0 \text{ \AA}^2$ . The calculated values [57] for pressure shifts and broadening of  $2^3\text{S}_1 - 2^3\text{P}_J$  helium transitions are  $\bar{v}\sigma_s = -1.9 \text{ MHz/Torr}$  and  $\bar{v}\sigma_b = 12 \text{ MHz/Torr}$ . The  $J$ -dependence of these coefficients is very weak, since at room temperature collisional energies are much greater than the fine structure splitting. Differences of a few percent are not ruled out by the calculations. Since these differences would lead to fine structure interval shifts on the order of 1 kHz in the 0 – 50 mTorr pressure range, they are carefully measured and corrected.

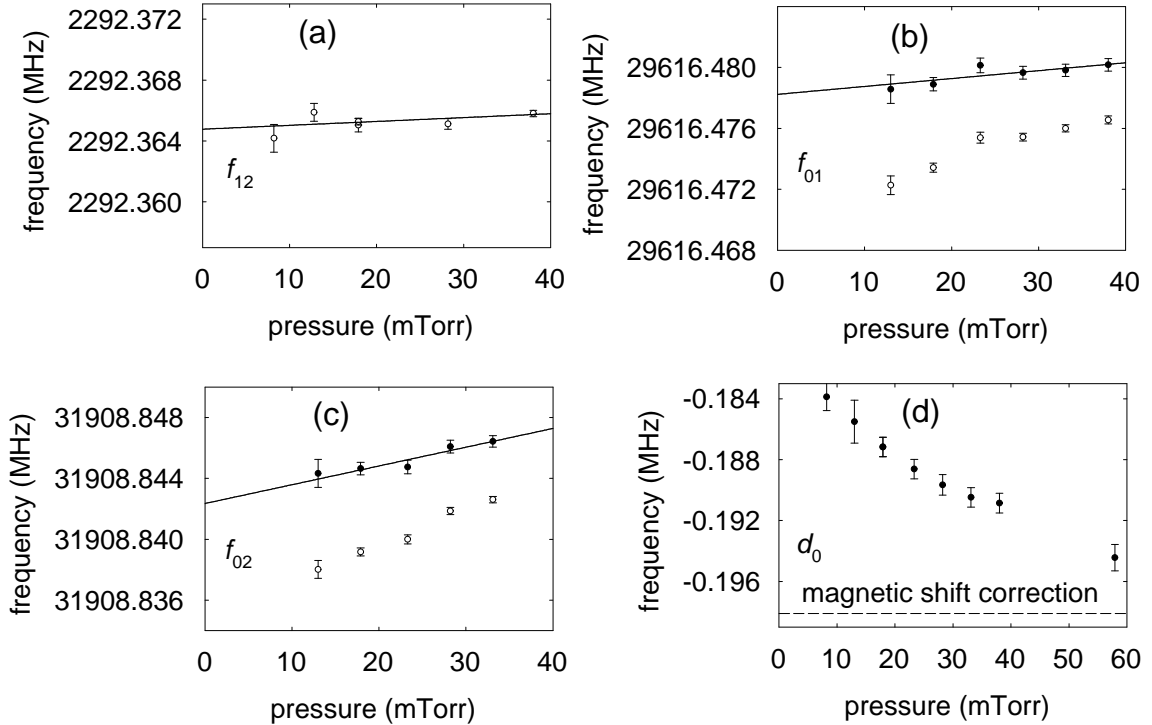


Figure 6.7: Linear extrapolation of the fine structure interval values to zero pressure. (a) The  $2^3P_1 - 2^3P_2$  interval. (b) The  $2^3P_0 - 2^3P_1$  interval. Open circles are the raw measurements, and filled circles include corrections for the light-pressure effect. (c) The  $2^3P_0 - 2^3P_2$  interval. Open circles are the raw measurements, and filled circles include corrections for the light-pressure effect. (d) Frequency offset of the  $m_J, m'_J = 0$  peak from the average of the  $m_J, m'_J = \pm 1$  peaks of the  $2^3S_1 - 2^3P_2$  transition, defined as  $d_0$ , as a function of pressure. The value of  $d_0$  corrected for the magnetic shift is proportional to the light-pressure-induced shift at that pressure.

### 6.3.3 Systematic Pressure Shift Corrections

Fine structure intervals are measured at several pressure points. Linear extrapolation to zero pressure yields the interval values corrected for pressure shifts. The interval measurements at different pressures appear as open circles in Figs. 6.7 (a), (b), and (c) for  $f_{12}$ ,  $f_{01}$ , and  $f_{02}$ , respectively.

The linear fit to the  $f_{12}$  interval pressure dependence is done directly from the mea-

sured values, and the zero-pressure intercept is 2 292.364 77(37) MHz. The measured slope is 0.025(13) MHz/Torr. The linear fits to the  $f_{01}$  and  $f_{02}$  interval pressure dependences are done after applying corrections for the nonlinear light-pressure-induced shifts, as explained in Sec. 6.4. These shifts are the subject of Chapter 4.

## 6.4 Light-Pressure-Induced Shifts

Light-pressure-induced shifts of the fine structure intervals are corrected as described in Sec. 4.5. The principle that allows for easy correction is illustrated in Fig. 4.14. For a resolved atomic level, the average number of photons  $\langle n \rangle$  scattered by a driven transition is inversely proportional to the decay rate out of that transition [53]. Thus, according to the coupling coefficients in Fig. 4.14,

$$2^3S_1 - 2^3P_0 (m_J, m'_J = 0) : \langle n \rangle = 1.5, \quad (6.32)$$

$$2^3S_1 - 2^3P_1 (m_J, m'_J = \pm 1) : \langle n \rangle = 2, \quad (6.33)$$

$$2^3S_1 - 2^3P_2 (m_J, m'_J = \pm 1) : \langle n \rangle = 2, \quad (6.34)$$

$$2^3S_1 - 2^3P_2 (m_J, m'_J = \pm 0) : \langle n \rangle = 3. \quad (6.35)$$

The light-pressure-induced shift is proportional to  $\langle n \rangle$ .

Since  $\langle n \rangle = 2$  for both  $2^3S_1 - 2^3P_1 (m_J, m'_J = \pm 1)$  and  $2^3S_1 - 2^3P_2 (m_J, m'_J = \pm 1)$ , light-pressure-induced shifts cancel for the  $f_{12}$  interval if the  $m_J, m'_J = \pm 1$  sublevels are probed. The pairs of optical transitions of  $f_{01}$  and  $f_{02}$ , however, scatter different numbers of photons, and this mismatch is  $\delta \langle n \rangle = 0.5$ . The light-pressure-induced shifts can be directly measured by comparing the  $2^3S_1 - 2^3P_2 (m_J, m'_J = 0)$

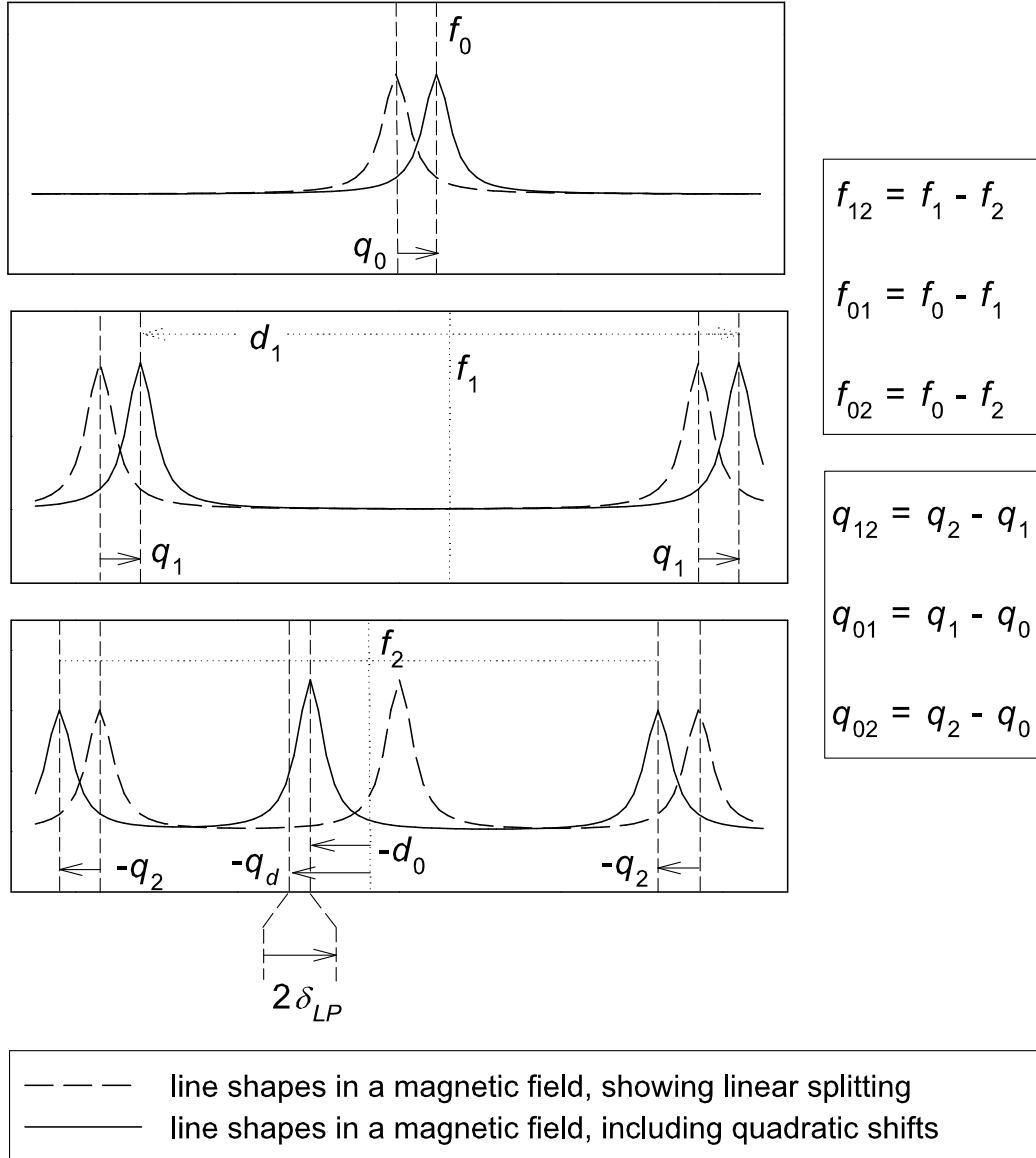


Figure 6.8: The schematic showing how the interval frequencies  $f_{12}$ ,  $f_{01}$ , and  $f_{02}$ , and the frequency  $d_0$  used for light-pressure correction, are measured from the three  $2^3S_1 - 2^3P_J$  transitions. In addition, it shows the quadratic magnetic shifts of the intervals and of  $d_0$ , which are  $q_{12}$ ,  $q_{01}$ ,  $q_{02}$ , and  $q_d$ . The light-pressure-induced shift is described by  $\delta_{LP} = (d_0 - q_d)/2$  and is explicitly shown for the  $2^3S_1 - 2^3P_2$  ( $m_J, m'_J = 0$ ) peak. The quadratic magnetic corrections are computed using the linear splitting  $d_1$ . The crossover peaks of the  $2^3S_1 - 2^3P_2$  transition are omitted for clarity.

peak position with the average of the  $2^3S_1 - 2^3P_2 (m_J, m'_J = \pm 1)$  peak positions. The difference between these two quantities is defined as  $d_0$ , and  $\delta\langle n \rangle = 1$  for this pair of transitions. Fig. 6.7 (d) shows  $d_0(p)$  measured at various helium pressures. If the  $d_0$  magnetic shift correction obtained by using magnetic shift coefficients from Sec. 5.1.1 is  $q_d = -0.198\,12(2)$  MHz, then the light-pressure-induced shift corrections for  $f_{01}$  and  $f_{02}$  as a function of pressure  $p$  are given by  $\delta_{LP}(p) = (d_0(p) - q_d)/2$ . The measured fine structure interval values then depend on  $p$  as follows,

$$f_{12}(p) = (\bar{f}_{12} - q_{12}) + a_{12}p, \quad (6.36)$$

$$f_{01}(p) = (\bar{f}_{01} - q_{01}) + a_{01}p - \frac{d_0(p) - q_d}{2}, \quad (6.37)$$

$$f_{02}(p) = (\bar{f}_{02} - q_{02}) + a_{02}p - \frac{d_0(p) - q_d}{2}, \quad (6.38)$$

where  $\bar{f}_{12}$ ,  $\bar{f}_{01}$ , and  $\bar{f}_{02}$  are the pressure-independent contributions to the measured interval values,  $a_{12}$ ,  $a_{01}$ , and  $a_{02}$  are the three linear pressure shift coefficients discussed in Sec. 6.3,  $q_{12}$ ,  $q_{01}$ , and  $q_{02}$  are the interval magnetic shift corrections, and the  $\delta_{LP}(p)$  term vanishes for  $f_{12}$  and is the same for  $f_{01}$  and  $f_{02}$ . The diagram showing how the interval frequencies  $f_{12}$ ,  $f_{01}$ , and  $f_{02}$ , and the frequency  $d_0$ , as well as their quadratic shifts  $q_{12}$ ,  $q_{01}$ ,  $q_{02}$ , and  $q_d$ , are measured from the three  $2^3S_1 - 2^3P_J$  transitions.

The fine structure interval measurements corrected for the light-pressure-induced shifts are shown with filled circles in Figs. 6.7 (b) and (c) as a function of pressure. The intervals are extrapolated to zero pressure, yielding the intercept values 29 616.478 24(48)(54) MHz and 31 908.842 36(51)(65) MHz for  $f_{01}$  and  $f_{02}$ , respectively. The first error corresponds to the linear pressure shift correction, and the second error corresponds to the light-pressure-induced shift correction, as explained below. The measured slopes are 0.052(25) MHz/Torr and 0.123(32) MHz/Torr.

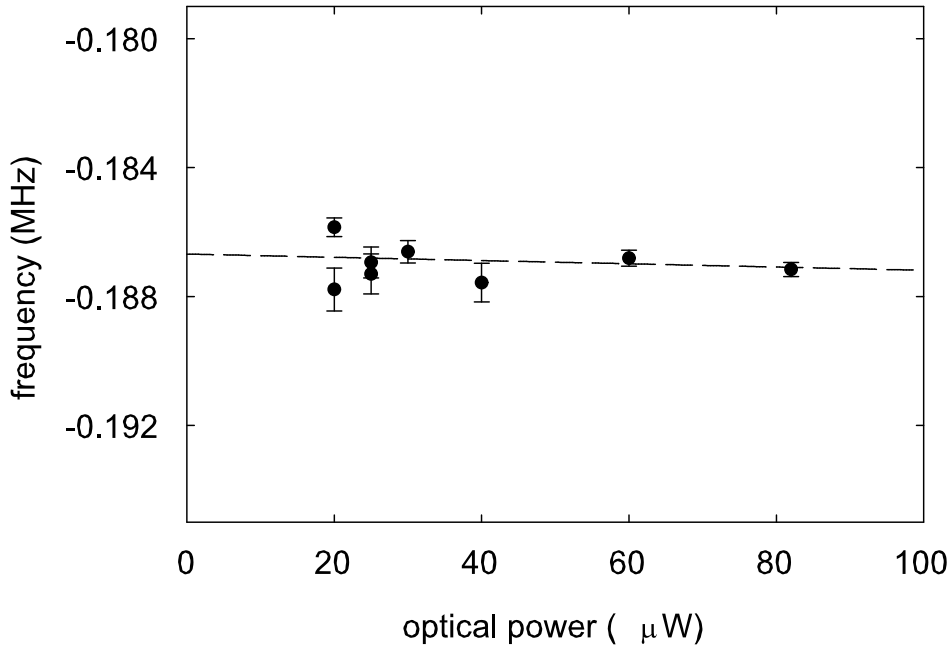


Figure 6.9: Linear dependence of  $d_0$ , the measure of the light-pressure-induced shifts, on optical power.

The light-pressure-induced shift correction error arises from some uncertainty in decoupling the possible optical power dependence of the light-pressure effect from the light shift of the  $2^3\text{S}_1 - 2^3\text{P}_2(m_J, m'_J = 0)$  peak relative to that of the  $2^3\text{S}_1 - 2^3\text{P}_2(m_J, m'_J = \pm 1)$  peaks. Two arguments show that this coupling and the associated error are very small. First, the light-pressure-induced shifts are expected to be independent of the optical power to first order from Chapter 4. Second, the optical power dependence of  $d_0$  was measured and found to be consistent with zero, as illustrated in Fig. 6.9. The measured dependence of  $d_0$  on optical power at the typical pressure of 18 mTorr is  $d_0 = -186.7(4) \text{ kHz} - 0.00503(599) \text{ kHz}/\mu\text{W}$ . Although the slope of this linear fit is consistent with zero, the standard deviation of all 18 mTorr  $d_0$  measurements at the optical powers of 20 – 80  $\mu\text{W}$  and discharge powers of 10

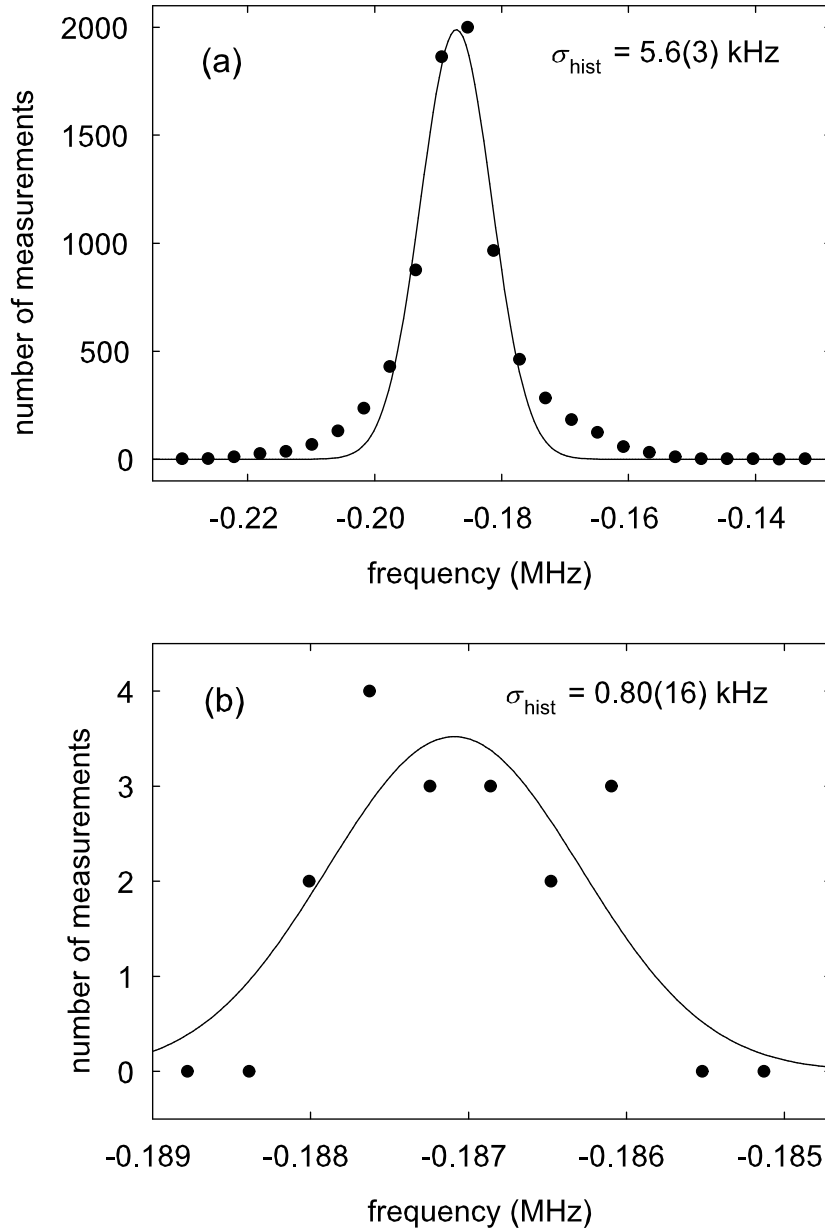


Figure 6.10: (a) The histogram of all  $d_0$  measurements at the same pressure setting of 18 mTorr throughout the data run. It is much broader in the wings than would be expected from a statistical distribution. The width of the fitted Gaussian is 5.6(3) kHz, while the calculated standard deviation of all the measurements is 9.1 kHz. (b) The histogram of all the daily  $d_0$  measurements at 18 mTorr, each measurement containing at least 300 values. The histogram is 0.80(16) kHz wide, much broader than the typical 0.34 kHz statistical error on  $d_0$ .

– 25 W,  $\sigma_d = 0.65$  kHz, was taken as the uncertainty on the  $d_0$  measurements at all pressure points, rather than the small statistical errors. The histogram of all the 18 mTorr  $d_0$  measurements taken throughout the data run is shown in Fig. 6.10 (a). It is much broader in the wings than would be expected from a statistical distribution. The width of the fitted Gaussian is 5.6(3) kHz, which underestimates the actual rms spread in measured values of 9.1 kHz. The histogram of all the daily  $d_0$  measurements at 18 mTorr, with at least 300 values in each measurement, is shown in Fig. 6.10 (b). The width of the Gaussian fitted to the histogram is 0.80(16) kHz, in agreement with  $\sigma_d = 0.65$  kHz, and much larger than the expected width, which equals the typical  $d_0$  statistical error of 0.34 kHz. Because of the large  $d_0$  scatter, the uncertainty  $\sigma_d$  was used in the light-pressure corrections in Fig. 6.7 when it exceeded the statistical errors, which was not the case for the low pressure points. The light-pressure-induced shift corrections contribute 0.54 kHz and 0.65 kHz uncertainties in the pressure extrapolation of the  $f_{01}$  and  $f_{02}$  intervals.

## 6.5 Optical Power Shifts

Optical beams perturb the atomic Hamiltonian and result in ac Stark shifts of energy levels, also known as light shifts. For two laser beams with small saturation parameters  $s$ , the light shift of the interval between two Zeeman sublevels  $|g, m\rangle$  and  $|e, n\rangle$  is [67, 68]

$$\delta\omega_{\text{LS}} = 2sC_m^n \left[ \frac{\omega_0 - \omega}{1 + [2(\omega_0 - \omega)/\Gamma]^2} + \frac{\omega_0 + \omega}{1 + [2(\omega_0 + \omega)/\Gamma]^2} \right], \quad (6.39)$$

where  $C_m^n$  is the coupling coefficient between  $|g, m\rangle$  and  $|e, n\rangle$ .

The first term of the light shift in eq. (6.39) is odd in laser detuning  $\omega - \omega_0$ , and does not contribute to a shift of a saturation spectroscopy line. The second term, called the Bloch-Siegert shift, is on the order of 0.01 Hz and is negligible.

Light shifts also arise from non-resonant atomic levels that are coupled to the ground or excited state of the probed transition by the laser field. Neglecting the Bloch-Siegert shifts, the contribution of non-resonant levels to the light shift is [67]

$$\delta\omega_{\text{LS}}^{\text{nonres}} = \frac{s\Gamma^2}{4} \left[ \sum_{j \neq m,n} \frac{C_m^j}{\omega_{jm} - \omega} - \sum_{k \neq m,n} \frac{C_k^n}{\omega_{kn} - \omega} \right]. \quad (6.40)$$

The value of  $\delta\omega_{\text{LS}}^{\text{nonres}}$  is on the order of a kilohertz for the  $2^3\text{S} - 2^3\text{P}$  helium transitions. Moreover, additional contribution to the light shift may result from eq. (6.39) if points on the line profile are not distributed perfectly symmetrically about the line center. Therefore, light shifts contribute to the error budget, and are measured and accounted for in the final results.

The dependences of the fine structure intervals on optical power of the pump or probe beam are plotted in Fig. 6.11. The pump and probe powers were kept equal throughout the experiment. The optical power used in the measurements of pressure dependence and light-pressure-induced shifts is  $80 \mu\text{W}$ , and the light shift corrections found from linear slopes in Fig. 6.11 and applied to the fine structure values are  $-0.82(11)$  kHz,  $1.17(16)$  kHz, and  $0.76(20)$  kHz for  $f_{12}$ ,  $f_{01}$ , and  $f_{02}$ , respectively.

## 6.6 Discharge Power Shifts

The dependences of fine structure intervals on rf discharge power were found to be very weak, and are plotted in Fig. 6.12. The discharge power used in the

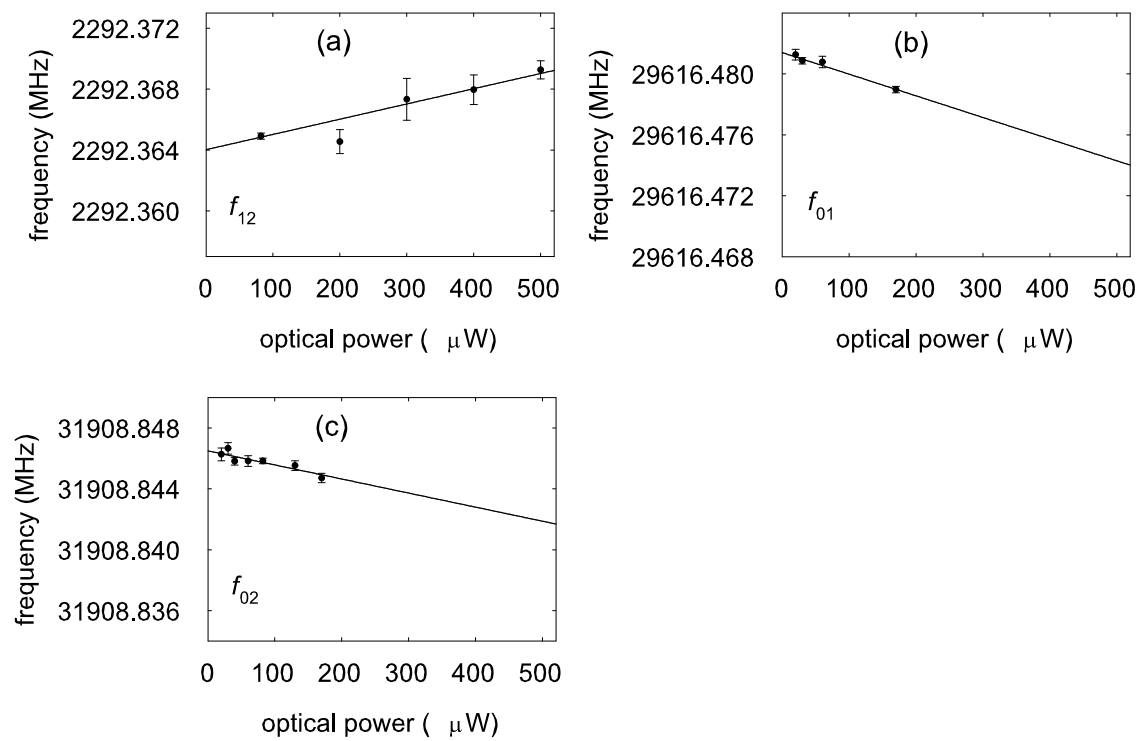


Figure 6.11: Light shifts of the fine structure intervals. (a) The  $2^3\text{P}_1 - 2^3\text{P}_2$  interval. (b) The  $2^3\text{P}_0 - 2^3\text{P}_1$  interval. (c) The  $2^3\text{P}_0 - 2^3\text{P}_2$  interval.

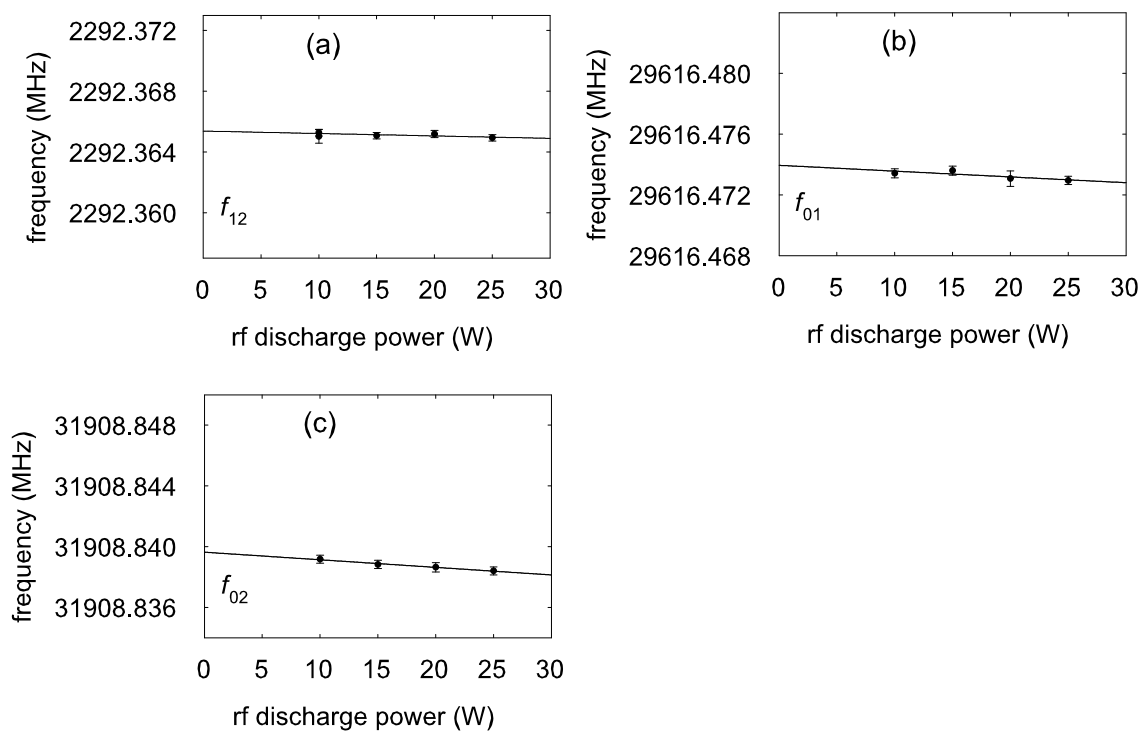


Figure 6.12: Dependences of the fine structure intervals on rf discharge power. (a) The  $2^3P_1 - 2^3P_2$  interval. (b) The  $2^3P_0 - 2^3P_1$  interval. (c) The  $2^3P_0 - 2^3P_2$  interval.

measurements of pressure dependence and light-pressure-induced shifts is 10 W, and the discharge power corrections found from linear slopes in Fig. 6.12 and applied to the fine structure values are 0.16(18) kHz, 0.38(26) kHz, and 0.50(23) kHz for  $f_{12}$ ,  $f_{01}$ , and  $f_{02}$ , respectively.

## 6.7 Magnetic Field Corrections

The magnetic field in the discharge cell was measured using the Zeeman splitting of  $2^3S_1 - 2^3P_1$  transition peaks, as described in Sec. 5.1.3. The value of the field is 52.6077(25) G, where the error corresponds to the standard deviation of all Zeeman splitting measurements throughout the period of data collection. It indicates the degree of temporal field variation during the experiment.

Using the magnetic shift coefficients from Sec. 5.1.1, the magnetic field corrections applied to the fine structure intervals are  $-1188.74(11)$  kHz,  $471.75(4)$  kHz, and  $-716.98(7)$  kHz for  $f_{12}$ ,  $f_{01}$ , and  $f_{02}$ , respectively. In addition, as mentioned in Sec. 5.2, the error associated with magnetic field inhomogeneity in the illuminated region of the cell does not exceed 0.10 kHz.

## 6.8 Consideration of Other Systematic Effects

### 6.8.1 Wavefront Curvature of Optical Beams

Saturation spectroscopy signals may be broadened and frequency shifted if they interact with curved wavefronts of Gaussian optical beams [69]. Since this effect is related to beam geometry, it is not expected to contribute to frequency shifts of fine

structure intervals. Nevertheless, care is taken to minimize effects of laser wavefronts on spectroscopy. The beam diameter is expanded to 2 cm, and the optics arrangement on the pump beam side of the helium cell matches that on the probe beam side. Fixed 8 mm diameter apertures at both ends of the cell confine the spectroscopy signal to atoms near the central part of the beams where wavefronts are flattest, and the intensity profile is relatively uniform. The rule of thumb [47] is to make the wavefront radius of curvature  $R$  large enough to satisfy

$$R \gg \frac{w^2}{\lambda} \sim 10^3 \text{ cm}, \quad (6.41)$$

where  $w = 4$  mm is the radius of the beam portion contributing to the spectroscopy signal. If  $w_0 = 1$  cm is the beam radius at the waist and  $x$  is the distance along the beam measured from the waist [46],

$$R(x) = x \left[ 1 + \left( \frac{\pi w_0^2}{\lambda x} \right)^2 \right] \sim 10^6 \text{ cm} \quad (6.42)$$

as far as  $x = 2$  m away from the beam waist. Matching the powers of pump and probe also helps eliminate frequency shifts [69]. Finally, ground state helium atoms serve as buffer gas in this experiment. Buffer gas greatly reduces shifts related to wavefront curvature, since collisions randomize atomic motion and atoms sample less curvature. Even at a low pressure of 10 mTorr, the mean free path in the cell is only  $l = \bar{v}\tau \approx 0.8$  mm.

### 6.8.2 Frequency Offset between Pump and Probe Beams

Because of the frequency offset between pump and probe beams  $\delta_0 = 2$  MHz, atoms contributing to the saturation signal move with a non-zero average velocity.

The holes burned by the pump and probe in the atomic velocity distribution overlap on the side of the broad Gaussian, potentially shifting the measured center of the resonance. Taking into account finite Doppler width as well as the frequency offset  $\delta_0$ , the saturation spectroscopy line shape in eq. (6.6) is modified as [61]

$$S(\omega) = S_0 \frac{1}{1 + \frac{(\omega - \omega_0)^2}{(\gamma/2)^2}} \exp\left(-\frac{(\omega - \omega_0 + \delta_0/2)^2}{(kv_D)^2}\right). \quad (6.43)$$

For experimental values of  $\gamma$  and  $kv_D$ , the deviation of eq. (6.43) from a Lorentzian is only 0.01 kHz. Moreover, this shift cancels when fine structure intervals are computed, and does not affect the results at the level of precision achieved here.

### 6.8.3 Coupling of Systematic Effects

Most systematic measurements of the fine structure intervals include more than one source of frequency shifts. One example is the pressure dependence of the intervals which includes linear pressure shifts and light-pressure-induced shifts discussed in Chapter 4. These two effects are decoupled as described in Sec. 6.4. Velocity changing collision pedestals also exhibit a pressure dependence, depicted in Fig. 6.4. The error due to vcc in the intervals that contain  $2^3S_1 - 2^3P_2$  lines with poorly resolved vcc pedestals is discussed in Sec. 6.2.3. The interdependence on pressure is minimized by taking data at low pressures where the relative height of the vcc pedestals does not exceed 0.055.

Among the other experimental parameters contributing to the error budget, - helium pressure, optical power, rf discharge power, and magnetic field, - only helium pressure and optical power, and discharge and optical powers, are potentially interdependent pairs.

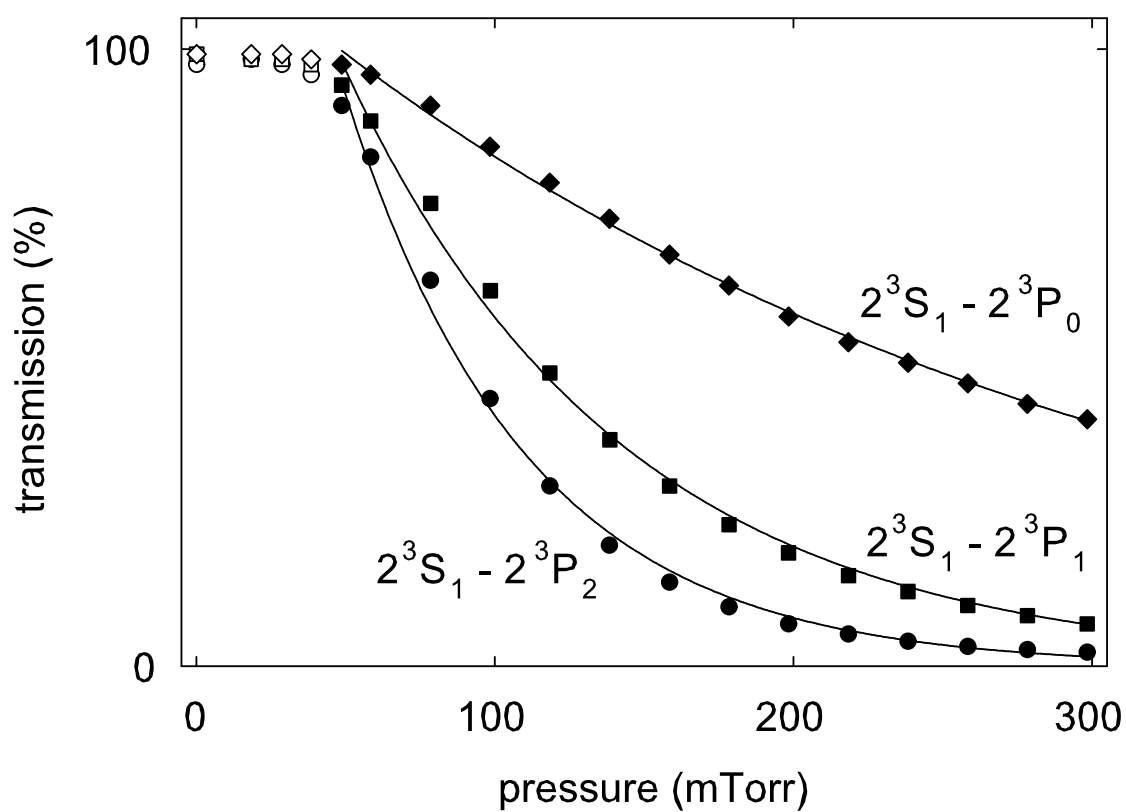


Figure 6.13: Variation of optical power transmitted through the cell with helium pressure.

The coupling of pressure and optical power was measured and plotted in Fig. 6.13. At helium pressures above 50 mTorr, the discharge cell obeys the linear absorption law, and transmitted single-beam power decays exponentially, with  $1/e$  attenuation occurring at 320 mTorr, 140 mTorr, and 110 mTorr for  $2^3S_1 - 2^3P_0$ ,  $2^3S_1 - 2^3P_1$ , and  $2^3S_1 - 2^3P_2$ , respectively. Below 50 mTorr, the production of metastables with the rf discharge is less effective, and the transmitted power is constant with pressure. Since all experimental data was collected at pressures under 60 mTorr, no corrections for optical thickness of the helium cell were needed.

Although at pressures above 60 mTorr the discharge power and optical power are weakly coupled and the transmission of optical power through the cell decreases with increasing discharge power, no significant attenuation of transmitted light is observed in the pressure range used in the experiment.

## 6.9 Experimental Statistics

To obtain a value from a series of  $f_{JJ'} = 2^3P_J - 2^3P_{J'}$  fine structure interval measurements, a weighted mean

$$\mu_w = \frac{\sum f_i / \sigma_i^2}{\sum 1 / \sigma_i^2} \quad (6.44)$$

is calculated, where  $f_i$  is the  $i$ -th measured  $f_{JJ'}$  value and  $\sigma_i$  is its error. The scatter of the  $f_i$  values determines the statistical error of the mean for a series of  $N$  measurements of  $f_{JJ'}$ ,

$$\sigma_\mu = \sqrt{\frac{\sum (f_i - \mu_w)^2}{N(N-1)}}. \quad (6.45)$$

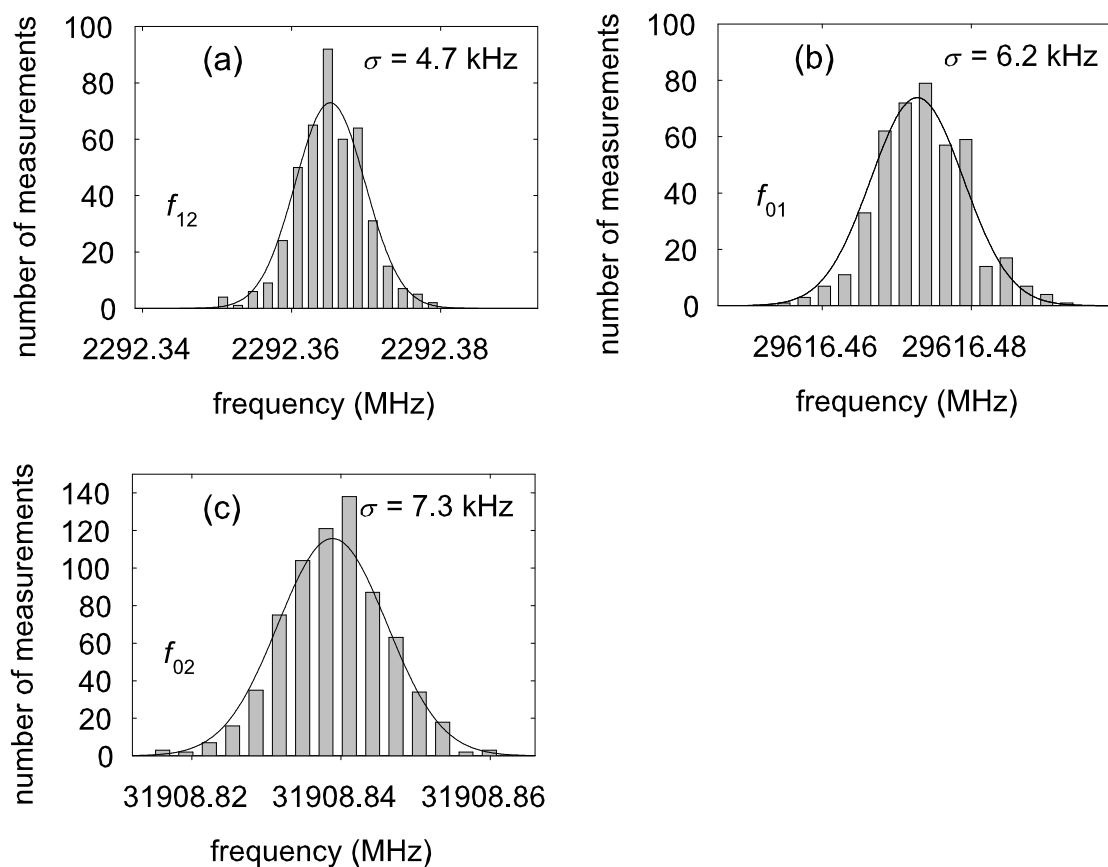


Figure 6.14: Typical fine structure interval measurement histograms for approximately 30 hours of data collection at 18 mTorr pressure. (a) The  $2^3P_1 - 2^3P_2$  interval. (b) The  $2^3P_0 - 2^3P_1$  interval. (c) The  $2^3P_0 - 2^3P_2$  interval.

Typical fine structure interval statistical distributions for approximately 30 hours of data collection at 18 mTorr pressure are shown in Figs. 6.14 (a), (b), and (c) for  $f_{12}$ ,  $f_{01}$ , and  $f_{02}$ , respectively. The statistical errors on individual data points are typically 0.2 – 0.5 kHz. Particularly at helium pressures under 15 mTorr or optical powers under 30  $\mu\text{W}$ , reducing these errors by a factor of 2 could require additional weeks of data collection per point, at the present signal to noise ratio and stability of the clock laser. The combined statistical errors for the fine structure intervals from all measurements in the data set are less than 0.1 kHz.

## 6.10 Results

The final fine structure interval values along with applied systematic corrections and errors are summarized in the table below.

(in units of kHz)	$2^3\text{P}_1 - 2^3\text{P}_2$	$2^3\text{P}_0 - 2^3\text{P}_1$	$2^3\text{P}_0 - 2^3\text{P}_2$
Zero-pressure intercept with			
light-pressure correction	2 292 364.77(37)	29 616 478.24(72)	31 908 842.36(83)
Light intensity shift	-0.82(11)	+1.17(16)	+0.76(20)
Magnetic field measurement	-1 188.74(11)	+471.75(04)	-716.98(07)
Magnetic field inhomogeneity	+0.00(10)	+0.00(10)	+0.00(10)
Velocity changing collisions	+0.00(40)	+0.00(20)	+0.00(40)
Discharge power shift	+0.16(18)	+0.38(26)	+0.50(23)
Final result	2 291 175.4(6)	29 616 951.5(8)	31 908 126.6(1.0)

The measurement results demonstrate internal consistency of the experiment, since  $f_{12} + f_{01} = 31\,908\,126.9(1.0)$  kHz, which agrees with  $f_{02} = 31\,908\,126.6(1.0)$  kHz. All three fine structure interval results improve on their previous measurements. In addition, the  $f_{12}$  value is the most precise helium fine structure measurement to date.

The results are graphically compared to those from three other research groups in Fig. 6.15. The specifics of the other groups' experiments are discussed in Chapter 2. The  $f_{12}$  Harvard measurement is in excellent agreement with the other experimental results, and the  $f_{01}$  result agrees with the LENS and York University results, but not with the University of North Texas measurement. The  $f_{02}$  result is not in agreement with the Texas group measurement. It is worth noting that the disagreeing Texas  $f_{01}$  result in Fig. 6.15 (b) is based on their  $f_{02}$  measurement.

Fig. 6.16 summarizes the most recent theoretical and experimental  $f_{12}$  and  $f_{01}$  fine structure interval values. The smaller interval  $f_{12}$  is typically used as a check of helium fine structure calculations. Currently, there is a 13(5) kHz disagreement between the Pachucki and Sapirstein value [3] and the Harvard measurement, and a 21(1) kHz disagreement between the Drake value [4] and the Harvard measurement. Until there is close agreement between theory and experiment, a reliable value of  $\alpha$  cannot be derived from the  $f_{01}$  interval measurements.

Currently, the two theoretical values do not contain all of the same higher-order corrections arising from the electron-electron interactions, although both groups agree that terms of that type must be present in the final result [21, 25]. As a first step, Pachucki and Sapirstein must check Drake's calculations of the electron-electron contributions, which then should be independently confirmed. This cross-check has al-

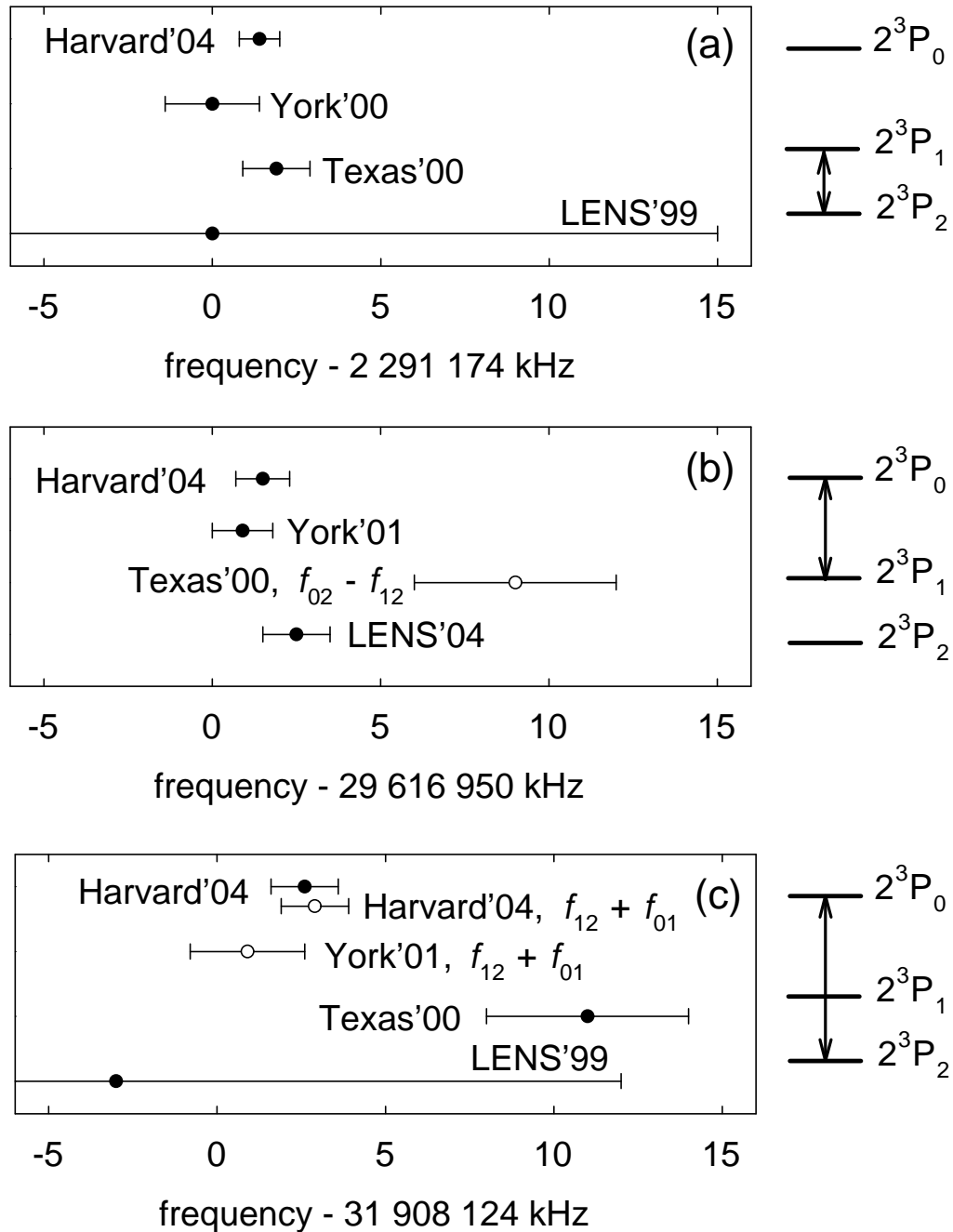


Figure 6.15: The comparison of the most recent helium fine structure interval measurements by four research groups. (a) The  $2^3P_1 - 2^3P_2$  interval. (b) The  $2^3P_0 - 2^3P_1$  interval. (c) The  $2^3P_0 - 2^3P_2$  interval. The interval values shown with open circles are not direct measurements, but consistency checks using measurements of two other intervals.

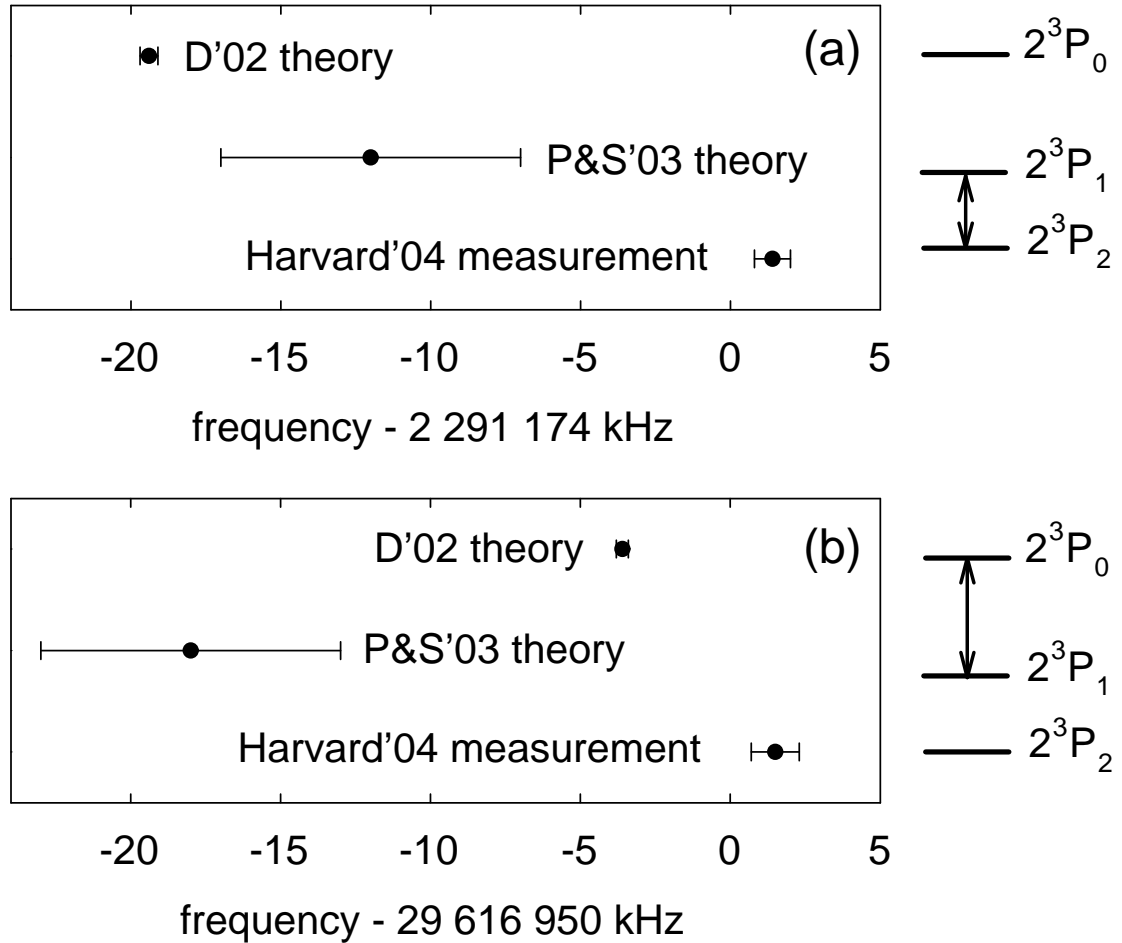


Figure 6.16: The comparison of the Harvard helium fine structure interval measurements and theoretical values by Pachucki and Sapirstein (PS) [3] and Drake (D) [4]. The fine structure constant from the electron magnetic moment experiment [6] was used in the theoretical interval expansions. (a) The  $2^3P_1 - 2^3P_2$  interval. (b) The  $2^3P_0 - 2^3P_1$  interval.

ready been carried out for most electron-nuclear contributions except for the Bethe logarithmic terms not yet verified by Drake. The next step is to complete the calculations of any remaining terms of order  $\alpha^5$ , which would enable the theorists to assign a more meaningful error to their results. If the complete and confirmed calculation to this order brings theoretical and experimental values into agreement, and if the  $\mathcal{O}(\alpha^6)$  contributions are shown to be small, the measurement of the  $f_{01}$  interval can be used to derive a value of  $\alpha$ .

At this time, it is not likely that the experimental values are highly inaccurate, since they have been confirmed by very different techniques, including one reported in this thesis. This leads to the conclusion that the discrepancy between theory and experiments arises from an incomplete understanding of the theory. Ongoing theoretical efforts [3, 4] show promise that the source of the disagreement may be found in the near future, leading to a 14 part in  $10^9$  determination of  $\alpha$  based on helium fine structure measurements.

# Chapter 7

## Conclusion

### 7.1 Significance of the Results

A precise measurement of helium  $2^3P$  fine structure was performed using saturation spectroscopy in a discharge cell. All other helium fine structure experiments [36, 37, 40] relied on metastable helium beams. Although the use of the discharge cell necessitated studying additional systematic effects such as pressure shifts, discharge power shifts, and collisional cross-relaxation of atomic velocities, the accuracy achieved in this experiment shows that gas cells are useful alternatives to atomic beams in precision measurements. The advantages of using the cell are a high signal to noise ratio and the possibility of investigating light-pressure-induced shifts as a function of helium pressure. Light-pressure-induced frequency shifts are one of the largest systematic effects in this measurement, and the use of the discharge cell facilitates their study and makes it possible to experimentally determine and apply corrections to compensate for them.

The measured fine structure values are 2 291 175.4(6) kHz for the  $2^3P_1 - 2^3P_2$  interval, 29 616 951.5(8) kHz for the  $2^3P_0 - 2^3P_1$  interval, and 31 908 126.6(1.0) kHz for the  $2^3P_0 - 2^3P_2$  interval. The values of the  $f_{12}$  and  $f_{01}$  intervals are the most precise helium fine structure measurements to date, and the  $f_{02}$  interval value exceeds the precision of the best prior direct measurement of this interval by a factor of 3. The  $f_{01}$  measurement helps resolve an existing disagreement between the other experiments. The results are compared to recent helium results obtained by other research groups in Fig. 6.15.

## 7.2 Future Improvements

In the course of this experiment it became clear that greater magnetic fields are needed for a higher precision. Currently, a field of about 50 G resolves the Zeeman sublevels of the helium atoms. This field is sufficient to cleanly resolve the lines of the  $2^3S_1 - 2^3P_0$  and  $2^3S_1 - 2^3P_1$  optical transitions, but the Lorentzian peaks of the  $2^3S_1 - 2^3P_2$  transition overlap in the wings, since this line has pronounced crossover resonances at low pressures. This overlap causes several problems. One problem is that the crossover resonance peaks in close proximity to the saturation peaks result in a relatively poor quality of magnetic field measurements using the  $2^3S_1 - 2^3P_2$  line splitting. If this were not the case, the field measurements using the  $2^3S_1 - 2^3P_1$  line splitting could be confirmed to a high precision. The second problem with the small splitting of the  $2^3S_1 - 2^3P_2$  line is the large degree of overlap of broad pedestals that arise from velocity changing collisions. Hence, the line cannot be fitted to a full line shape that includes both the narrow saturation peaks and the broad cross-relaxation

pedestals. Instead, the error due to the signal backgrounds has to be estimated from the studies of the  $2^3S_1 - 2^3P_0$  and  $2^3S_1 - 2^3P_1$  transitions.

The magnetic field can be increased with the existing magnetic coil setup by using a more powerful current supply. However, increasing the field by a factor of 2 or more would require redesigning the coils for two reasons. First, they would need to be water-cooled, as they cannot easily handle an excess of 4 A without significant overheating. Second, the magnetic field homogeneity requirement becomes much more stringent as magnetic fields increase. With the present configuration, the magnetic field inhomogeneity leads to a minor systematic error. However, increasing the field even twofold would result in a more appreciable error, on the order of 0.5 kHz. Thus, the dimensions of the coils might need to be increased to accommodate a larger magnetic field. An important advantage of having a set of coils that can accept high currents is the ability to perform fine structure measurements at several magnetic field values, which is a valuable consistency check.

Other upgrades that would benefit the experiment are improved laser amplitude noise rejection, and a better optical frequency reference. Residual laser amplitude noise is one of the leading sources of noise on the low pressure signals, and excellent noise regulation can open up a possibility of working at pressures of 5 mTorr or lower. The fiber amplifiers used to boost diode laser power are greater sources of noise than diode lasers themselves, and other power enhancement options should be pursued if they are available. It is possible to remove the amplifiers from the setup, but this could make the study of light shifts more difficult.

The advantage of improving the stability of the optical frequency reference, which

currently is based on frequency modulation spectroscopy of helium in a discharge cell, is a reduced scatter of the measured fine structure interval values. The effects of clock drift are minimized by measuring the optical transition frequencies in close temporal proximity of each other, but the scatter still reaches several kilohertz. A smaller degree of scatter would cut down the length of time required to attain the same level of statistical uncertainty. An iodine clock presently under construction has the potential of reducing the scatter to below a kilohertz.

Besides improvements to the fine structure measurements suggested above, future experiments can include the study of  $^3\text{He} - ^4\text{He}$  isotope shifts, and measurements of helium  $2^3\text{S} - 2^3\text{P}$  optical transition frequencies. A femtosecond frequency comb is currently being constructed to achieve a kilohertz or better level of accuracy on the optical frequencies.

### 7.3 Summary

The results presented in this thesis exceed the precision of other helium fine structure measurements, while demonstrating the use of discharge cells in precision measurements. In addition, this is the only experiment to directly measure all three helium  $2^3\text{P}$  fine structure intervals to a 1 kHz level. The  $2^3\text{P}_1 - 2^3\text{P}_2$  interval value agrees with other experiments and disagrees with theoretical predictions of two-electron QED. On the theoretical front, progress is being made to resolve the disagreement. Once the cause for the difference is discovered, the experimental value of the  $2^3\text{P}_0 - 2^3\text{P}_1$  interval can be used to obtain a new value of the fine structure constant to 14 parts in  $10^9$ .

# Bibliography

- [1] A. Sommerfeld, *Ann. Phys. Lpz.* **51**, 1 (1916).
- [2] Toichiro Kinoshita, *Rep. Prog. Phys.* **59**, 1459 (1996).
- [3] Krzysztof Pachucki and Jonathan Sapirstein, *J. Phys. B* **36**, 803 (2003).
- [4] G. W. F. Drake, *Can. J. Phys.* **80**, 1195 (2002).
- [5] Peter J. Mohr and Barry N. Taylor, *Rev. Mod. Phys.* **72**, 351 (2000).
- [6] R. S. Van Dyck Jr., P. B. Schwinberg, and H. G. Dehmelt, *Phys. Rev. Lett.* **59**, 26 (1987).
- [7] T. Kinoshita and M. Nio, *Phys. Rev. Lett.* **90**, 021803 (2003).
- [8] K. von Klitzing, G. Dorda, and M. Pepper, *Phys. Rev. Lett.* **45**, 494 (1980).
- [9] B. D. Josephson, *Phys. Lett.* **1**, 251 (1962).
- [10] J.-S. Tsai, A. K. Jain, and J. E. Lukens, *Phys. Rev. Lett.* **51**, 316 (1983).
- [11] W. D. Phillips, W. E. Cooke, and D. Kleppner, *Metrologia* **13**, 179 (1977).
- [12] E. R. Williams, G. R. Jones Jr., S. Ye, R. Liu, H. Sasaki, P. T. Olsen, W. D. Phillips, and H. P. Layer, *IEEE Trans. Instrum. Meas.* **38**, 233 (1989).
- [13] Eckhard Krüger, Wolfgang Nistler, and Winfried Weirauch, *IEEE Trans. Instrum. Meas.* **46**, 101 (1997).
- [14] D. S. Weiss, B. C. Young, and S. Chu, *Phys. Rev. Lett.* **70**, 2706 (1993).
- [15] S. Stenholm, *Rev. Mod. Phys.* **58**, 699 (1986).
- [16] A. Peters, K. Y. Chung, B. Young, J. Hensley, and S. Chu, *Phil. Trans. R. Soc. Lond. A* **355**, 2223 (1997).
- [17] Michael P. Bradley, James V. Porto, Simon Rainville, James K. Thompson, and David E. Pritchard, *Phys. Rev. Lett.* **83**, 4510 (1999).

- 
- [18] Andreas Wicht, Joel M. Hensley, Edina Sarajlic, and Steven Chu, *Phys. Scr.* **102**, 82 (2002).
- [19] Chu group, private communication.
- [20] W. Liu *et al.*, *Phys. Rev. Lett.* **82**, 711 (1999).
- [21] G. W. F. Drake, private communication.
- [22] G. Breit, *Phys. Rev.* **34**, 553 (1929).
- [23] H. A. Bethe and E. E. Salpeter, *Quantum Mechanics of One- and Two-Electron Atoms, 2nd edition* (Plenum, New York, 1977).
- [24] Krzysztof Pachucki and Jonathan Sapirstein, *J. Phys. B* **33**, 5297 (2000).
- [25] K. Pachucki, private communication.
- [26] Michael L. Lewis and Paul H. Serafino, *Phys. Rev.* **134**, A1181 (1978).
- [27] Zong-Chao Yan and G. W. F. Drake, *Phys. Rev. Lett.* **74**, 4791 (1995).
- [28] Tao Zhang and G. W. F. Drake, *Phys. Rev. A* **54**, 4882 (1996).
- [29] Krzysztof Pachucki and Jonathan Sapirstein, *J. Phys. B* **35**, 1783 (2002).
- [30] Charles Schwartz, *Phys. Rev.* **134**, A1181 (1964).
- [31] James Daley, Marvin Douglas, Lars Hambro, and Norman M. Kroll, *Phys. Rev. Lett.* **29**, 12 (1972).
- [32] F. M. J. Pichanick, R. D. Swift, C. E. Johnson, and V. W. Hughes, *Phys. Rev.* **169**, 55 (1968).
- [33] A. Kponou, V. W. Hughes, C. E. Johnson, S. A. Lewis, and F. M. J. Pichanick, *Phys. Rev. A* **24**, 264 (1981).
- [34] W. Frieze, E. A. Hinds, V. W. Hughes, and F. M. J. Pichanick, *Phys. Rev. A* **24**, 279 (1981).
- [35] D. Shiner, R. Dixson, and P. Zhao, *Phys. Rev. Lett.* **72**, 1802 (1994).
- [36] J. Castilleja, D. Livingston, A. Sanders, and D. Shiner, *Phys. Rev. Lett.* **84**, 4321 (2000).
- [37] Pablo Cancio, Maurizio Artoni, Giovanni Giusfredi, Francesco Minardi, Francesco S. Pavone, and Massimo Inguscio, *Atomic Physics* **16**, 42 (1999).

- 
- [38] P. Cancio Pastor, G. Giusfredi, P. De Natale, G. Hagel, C. de Mauro, and M. Inguscio, Phys. Rev. Lett. **92**, 023001 (2004).
- [39] C. H. Storry, M. C. George, and E. A. Hessels, Phys. Rev. Lett. **84**, 3274 (2000).
- [40] M. C. George, L. D. Lombardi, and E. A. Hessels, Phys. Rev. Lett. **87**, 173002 (2001).
- [41] T. W. Hänsch and H. Walter, Rev. Mod. Phys. **71**, S242 (1999).
- [42] Gary C. Bjorklund, Opt. Lett. **5**, 15 (1980).
- [43] Thanks to O. Poulsen and C. Larsen of OFS, Denmark, for providing the 10 km optical fiber.
- [44] R. Y. Chiao, C. H. Townes, and B. P. Stoicheff, Phys. Rev. Lett. **12**, 592 (1964).
- [45] R. Paschotta, D. C. Hanna, P. De Natale, G. Modugno, M. Inguscio, and P. Laporta, Opt. Commun. **136**, 243 (1997).
- [46] Christopher C. Davis, *Lasers and Electro-Optics* (Cambridge University Press, Cambridge, 1996).
- [47] Wolfgang Demtröder, *Laser Spectroscopy, 3rd edition* (Springer, Berlin, 2003).
- [48] Jr. W. R. Bennet, Phys. Rev. **126**, 580 (1962).
- [49] M. G. Prentiss and S. Ezekiel, Phys. Rev. Lett. **56**, 46 (1986).
- [50] Rudolf Grimm, Ph.D. thesis, Swiss Federal Institute of Technology, 1989.
- [51] R. Grimm and J. Mlynek, Appl. Phys. B **49**, 179 (1989).
- [52] Rudolf Grimm and Jürgen Mlynek, Phys. Rev. Lett. **63**, 232 (1989).
- [53] F. Minardi, M. Artoni, P. Cancio, M. Inguscio, G. Giusfredi, and I. Carusotto, Phys. Rev. A **60**, 4164 (1999).
- [54] M. Artoni, I. Carusotto, and F. Minardi, Phys. Rev. A **62**, 023402 (2000).
- [55] V. G. Minogin and V. S. Letokhov, *Laser Light Pressure on Atoms* (Gordon and Breach, London, 1987).
- [56] V. S. Letokhov and V. P. Chebotayev, *Nonlinear Laser Spectroscopy, Springer Ser. Opt. Sci. 4* (Springer, London, 1977).
- [57] D. Vrinceanu, S. Kotochigova, and H. R. Sadeghpour, Phys. Rev. A **69**, 022714 (2004).

- 
- [58] Zong-Chao Yan and G. W. F. Drake, *Phys. Rev. A* **50**, R1980 (1994).
- [59] S. A. Lewis, F. M. J. Pichanick, and V. W. Hughes, *Phys. Rev. A* **2**, 86 (1970).
- [60] M. L. Lewis and V. W. Hughes, *Phys. Rev. A* **8**, 2845 (1973).
- [61] P. W. Smith and T. Hänsch, *Phys. Rev. Lett.* **26**, 740 (1971).
- [62] Julian Keilson and James E. Storer, *Q. Appl. Math.* **10**, 243 (1952).
- [63] P. R. Berman, P. F. Liao, and J. E. Bjorkholm, *Phys. Rev. A* **20**, 2389 (1979).
- [64] C. Brechignac, R. Vetter, and P. R. Berman, *Phys. Rev. A* **17**, 1609 (1978).
- [65] M. Pinard, C. G. Aminoff, and F. Laloë, *Phys. Rev. A* **19**, 2366 (1979).
- [66] Michel Baranger, *Phys. Rev.* **111**, 481 (1958).
- [67] A. T. Nguyen, D. Budker, S. K. Lamoreaux, and J. R. Torgerson, *Phys. Rev. A* **69**, 022105 (2004).
- [68] Harold J. Metcalf and Peter van der Straten, *Laser Cooling and Trapping* (Springer, New York, 1999).
- [69] J. L. Hall and C. J. Bordé, *Appl. Phys. Lett.* **29**, 788 (1976).